



TECHNISCHE
UNIVERSITÄT
WIEN

DISSERTATION

Widely Distributed Massive MIMO Communication Systems for High Mobility Users

*carried out for the purpose of obtaining the degree of
Doctor technicae (Dr. techn.)*

*submitted at Technische Universität Wien
Faculty of Electrical Engineering and Information Technology
by*

Dipl.-Ing. David LÖSCHENBRAND

Mat.Nr.: 00926714

under the supervision of

Privatdoz. Dipl.-Ing. Dr. techn. Thomas ZEMEN
AIT Austrian Institute of Technology GmbH

reviewed by

Prof. Fredrik TUFVESSON, Ph.D., Lund University, Sweden
Prof. Dr. techn. Florian KALTENBERGER, Eurecom, France

Vienna, May 2023

Affidavit

I declare in lieu of oath, that I wrote this thesis and performed the associated research myself, using only literature cited in this volume. If text passages from sources are used literally, they are marked as such.

I confirm that this work is original and has not been submitted elsewhere for any examination, nor is it currently under consideration for a thesis elsewhere.

I acknowledge that the submitted work will be checked electronically-technically using suitable and state-of-the-art means (plagiarism detection software). On the one hand, this ensures that the submitted work was prepared according to the high-quality standards within the applicable rules to ensure good scientific practice "Code of Conduct" at the TU Wien. On the other hand, a comparison with other student theses avoids violations of my personal copyright.

Signed:

Date:

Abstract

Massive multiple input multiple output (MIMO) systems utilize tens to hundreds of base station (BS) antennas to exploit diversity in space, and serve several users simultaneously in the same time-frequency resource, thus achieving unprecedented levels of spectral efficiency, energy efficiency, and reliability. For this reason, they became the method of choice in the current roll-out of 5G deployments. However, a stringent requirement for massive MIMO systems is accurate and timely channel state information (CSI) from all users to all BS antennas. Currently, the only viable and scalable solution is the application of a time division duplex (TDD) scheme and relying on channel reciprocity. In high mobility scenarios, this approach inherently causes service degradation, as outdated CSI introduces inter-user interference and a reduced signal to noise ratio (SNR).

In this thesis, we investigate, both analytically and numerically, the adverse effects of users with high mobility on the reliability in a massive MIMO system, propose mitigation strategies, and evaluate their effectiveness. We consider (i) prediction to increase the quality of outdated CSI estimates; (ii) orthogonal precoding (OP) to further exploit spatial diversity; and (iii) distributed BS antenna geometries.

More specifically, we derive the instantaneous and asymptotic signal to interference and noise ratio (SINR) of a TDD massive MIMO system for a time-correlated fading process utilizing multi-step minimum mean square error (MMSE) CSI prediction and quantify the improvement over the utilization of aged CSI. We additionally prove and show by numerical simulation that the capability of massive MIMO systems to reduce small-scale fading, i.e., the variance of the SINR, is independent of the CSI age. Further, we show the beneficial impact of OP in combination with CSI prediction on the reliability of a massive MIMO system by numerical link-level bit error rate (BER) simulation.

To substantiate the analytical and numerical findings, we develop a software-defined radio (SDR) based channel sounding framework. It has the capability to capture time-variant wireless channel impulse responses from two users to 32 BS antennas in highly dynamic scenarios in a fully parallel and time-synchronized manner. Moreover, the sounding framework is designed to support flexible BS antenna placements with an aperture of up to 90 m to characterize widely distributed (i.e., cell-free) setups. We conduct two vehicular measurement campaigns with highly mobile users in urban scenarios with BS antenna apertures ranging from 1 m to 50 m. The empiric evidence suggests that a widely distributed massive MIMO system, with BS antennas distributed over a wide aperture, mitigates the effects of aged CSI and reduces random fluctuations in signal strength, thus increasing reliability and energy efficiency.

Kurzfassung

Mobilfunksysteme mit großen Mehrfachantennen (massive MIMO) nutzen Dutzende bis Hunderte Antennenelemente an der Basisstation, um die Charakteristika der räumlichen Funkwellenausbreitung bestmöglich zu erfassen und sie wirksam einzusetzen. So gelingt es, mehrere Nutzer zeitgleich auf derselben Frequenz zu versorgen, wodurch noch nie dagewesene spektrale Effizienz, Energieeffizienz und Zuverlässigkeit erreicht wird. Aus diesem Grund dient massive MIMO als Basistechnologie in der Entwicklung und Einführung von 5G-fähigen Mobilfunksystemen. Allerdings erfordert massive MIMO eine exakte und rechtzeitige Schätzung des Zustands der Funkkanäle zwischen allen Nutzern und allen Basisstationsantennen. Derzeit ist der einzige praktikable und skalierbare Ansatz die Anwendung eines Zeitduplexverfahrens unter Annahme reziproker Funkkanäle. In Szenarien mit hoher Mobilität führt dieser Ansatz zwangsläufig zu einer Verschlechterung der Übertragungsqualität im Mobilfunknetz, da die veraltete Information über den Funkkanalzustand zu Interferenz zwischen Nutzern und zu einem geringeren Signal-Rausch-Verhältnis führt.

In dieser Arbeit untersuchen wir analytisch und numerisch die nachteiligen Auswirkungen von hoher Mobilität auf die Zuverlässigkeit eines massive MIMO-Systems, entwickeln Methoden zur Erhöhung der Zuverlässigkeit und bewerten ihre Wirksamkeit. Wir betrachten (i) Prädiktionsverfahren, um die Qualität der Schätzung der Funkkanalinformation zu verbessern; ii) orthogonale Vorcodierung (orthogonal precoding), um die räumliche Mehrfachausbreitung im Funkkanal bestmöglich zu nutzen; und iii) verteilte Antennengeometrien an der Basisstation. Unter Annahme eines zeitkorrelierten Schwundprozesses und eines mehrstufigen Prädiktionsverfahrens wird das momentane und asymptotische Verhältnis zwischen Signalleistung und Interferenz- und Rauschleistung (SINR) in einem massive MIMO-System abgeleitet. Die Verbesserung gegenüber der Verwendung von veralteter Funkkanalinformation wird dargestellt und quantifiziert. Durch einen Beweis und numerische Simulation wird gezeigt, dass die Verringerung der Varianz des SINR unabhängig vom Alter der Funkkanalinformation ist. Außerdem werden die positiven Auswirkungen von orthogonaler Vorcodierung in Kombination mit den entwickelten Prädiktionsverfahren auf die Zuverlässigkeit eines massive MIMO-Systems gezeigt.

Um die theoretischen und simulierten Ergebnisse zu untermauern, wird ein Funkkanalmesssystem basierend auf programmierbaren Sende- und Empfangskomponenten entwickelt. Es ermöglicht die parallele und zeitsynchronisierte Erfassung zeitveränderlicher drahtloser Funkkanalimpulsantworten von zwei Nutzern und 32 Basisstationsantennen in hochdynamischen Szenarien. Darüber hinaus ist das Funkkanalmesssystem so konzipiert, dass es flexible Anordnungen der Basisstationsantennen mit einer Apertur von bis zu 90 m ermöglicht. Zwei Messkampagnen mit Nutzern in Fahrzeugen in städtischen Szenarien mit einer Aperturgröße der Basisstation von 1 m bis 50 m wurden durchgeführt. Die Messdaten legen nahe, dass ein Aufbau mit weit verteilten Basisstationsantennen sinnvoll ist. Er reduziert die Auswirkungen von veralteter Funkkanalinformation, und zufällige Schwankungen der Signalstärke, was wiederum Zuverlässigkeit und Energieeffizienz erhöht.

Acknowledgements

Firstly, I would like to express my sincere gratitude to my supervisor Thomas Zemen, who provided guidance and motivation, extensive knowledge and critical questions, understanding and support, excitement and vision. Thank you for believing in my research, even when I didn't.

Many thanks to Fredrik Tufvesson from Lund University, and Florian Kaltenberger from Eurecom, who generously provided knowledge and expertise in fruitful discussions and while reviewing this thesis.

I am especially thankful for my colleagues and friends from AIT, Markus Hofer, Stefan Zelenbaba, Anja Dakić, Laura Bernadó, Benjamin Rainer, and Hamed Radpour, whose participation in countless discussions (on and off-topic), measurement campaigns, and shared lunch breaks is highly appreciated. I could not have wished for better office mates.

This endeavor would not have been possible without the unconditional support of my family, that always stands by me and has been encouraging me for as long as I can remember.

Finally, I would like to express my deepest gratitude to Debora, whose strength, patience, perspective, encouragement, support, and kindness contributed more to this thesis than she will ever know. And to my children, who may be the reason why it took longer than expected but are definitely the reason why I finished. This thesis is dedicated to them.

Contents

Affidavit	iii
Abstract	v
Kurzfassung	vii
Acknowledgements	ix
1 Introduction	1
1.1 Motivation and Objectives	1
1.2 Methodology, Contribution, and Outline	2
2 Massive MIMO for Mobile Users	5
2.1 Contents of this Chapter	5
2.2 Multiple Mobile Users Case	6
2.2.1 Signal Model	6
2.2.2 Channel Estimation	9
2.2.3 Multi-Step Channel Prediction	9
2.3 Spectral Efficiency and Channel Hardening for Multiple Users	11
2.3.1 Instantaneous and Asymptotic SINR	11
2.3.2 Ergodic and Asymptotic Spectral Efficiency	12
2.3.3 Channel Hardening	13
2.3.4 Numeric Results	14
2.4 Single Mobile User Case	18
2.4.1 Orthogonal Precoding Signal Model	18
2.4.2 Note on Interplay of Channel Aging and Channel Hardening	19
2.4.3 Channel Prediction Methods	21
2.4.4 Prediction Quality Assessment	23
2.4.5 Reliability Assessment	25
2.5 Main Findings and Conclusion	26
2.6 Related Literature	29
3 Data Acquisition and Processing	31
3.1 Contents of this Chapter	31
3.2 Massive MIMO Channel Sounding Framework	31
3.2.1 Channel Sounder Architecture	31
3.2.2 Transmit and Receive Antennas	33
3.2.3 Massive MIMO Calibration Unit	38
3.2.4 Synchronization	40
3.3 Channel Acquisition and Analysis	41
3.3.1 Channel Sounding Signal Model	41
3.3.2 Ray Tracing Implementation	42
3.3.3 Stochastic Characterization of the Wireless Propagation Channel	44

3.3.4	Stochastic Characterization of the Fading Process	47
3.3.5	Massive MIMO Signal Model	47
3.4	Related Literature	50
4	Measurement Campaigns and Results	53
4.1	Contents of this Chapter	53
4.2	DIST Measurement Campaign	53
4.2.1	Measurement Scenario	54
4.2.2	Single Antenna Results	54
4.2.3	Stochastic Evaluation	58
4.2.4	Key Findings	61
4.2.5	Massive MIMO Results	62
4.2.6	Key Findings	66
4.3	WIDE Measurement Campaign	67
4.3.1	Measurement Scenario	68
4.3.2	Single Antenna Results	70
4.3.3	Average Received Power	72
4.3.4	Delay- and Doppler spreads	74
4.3.5	Collinearity of the LSF in space	80
4.3.6	Key Findings	82
4.3.7	Massive MIMO Processing and Results	84
4.3.8	Key Findings	87
5	Concluding Remarks	89
5.1	Conclusion and Discussion	89
5.2	Outlook	90
	Bibliography	105

Chapter 1

Introduction

1.1 Motivation and Objectives

Since the inception of the first radio telegraphy transmission systems around 125 years ago by Marconi, wireless communication has become ubiquitous and indispensable in a globally connected world. In the early days, radio communication systems were complex, bulky, and only suitable for stationary applications like radio and television broadcasting. Advances both in transistor technology and information theory led to the deployment of cellular mobile networks, with the global system for mobile communications (GSM) being the first standard adopted by the masses. This marks a paradigm shift in telecommunications, as for the first time in human history, it is the people that are directly connected through devices they carry with them, instead of fixed installments we must frequent to communicate. Inherent to this transition is mobility of the user while communicating, which poses a technological challenge not encountered previously.

Currently, the fifth generation (5G) of cellular mobile networks is deployed around the world. It promises to not only connect people, but also machines (vehicles, trains, infrastructure, robots etc.), at a large scale. Accordingly, requirements on the network differ substantially from previous generations of mobile networks. Machine-type communication typically demands high reliability and low latency while still assuming high mobility of all participants.

The fundamental upper limit for the information rate that can be transmitted over a communication channel with bandwidth B and arbitrary low error rate, i.e., the *capacity* C of the communication channel, was found by Shannon in 1949 to be [1]

$$C = B \log_2 \left(1 + \frac{P}{\sigma^2} \right). \quad (1.1)$$

The transmit signal power is denoted by P and the noise power by σ^2 . The significance of this result cannot be overstated, as it shows that in the bandwidth-limited regime $P/\sigma^2 \gg 1$, increasing the transmit power linearly increases the capacity only logarithmically. To put this into perspective, doubling the signal to noise ratio (SNR) from $P/\sigma^2 = 10$ to $P/\sigma^2 = 20$ only increases the capacity by a factor of 1.27.

In an effort to keep up with the rising demands on communication systems in terms of data rate, reliability, and latency, simply utilizing more transmit power does not scale. Additionally, environmental concerns prohibit this approach. One historically proven strategy therefore is allocating more bandwidth to the communication channel, as there is a linear impact on capacity. However, electromagnetic spectrum is a limited resource and allocating more bandwidth may not be possible or practical, as it might be already in use.

Increasing transmit power or bandwidth solely focuses on the physical properties of a communication channel. On the contrary, advances in information theory on multiple input multiple output (MIMO) systems in the 1990s [2] led to the conclusion that multiple transmit and receive antennas and corresponding processing leads to a capacity expression that linearly depends on the number of transmit and receive antennas [3, Ch. 20],

$$C^{(\text{MIMO})} = \min \left(A^{(\text{RX})}, A^{(\text{TX})} \right) B \log_2 \left(1 + \frac{P}{\sigma^2} \right). \quad (1.2)$$

Here, $A^{(\text{RX})}$ and $A^{(\text{TX})}$ are the numbers of receive and transmit antennas, respectively, and uncorrelated MIMO channels are assumed. A viable path forward was found, but at the cost of computational complexity to perform complex MIMO transmit and receive algorithms.

In current 5G deployments, a key technological enabler is massive MIMO, a successor of conventional MIMO, introduced by Marzetta in 2010 [4]. The underlying idea of massive MIMO is to utilize a large number A of antennas (usually more than 64) at the base station (BS) of a cellular network, while a single antenna is sufficient at each of the K user terminals. There are several advantages to this approach, all of them mathematically rooted in the law of large numbers:

- The capacity of the communication system grows unbounded and logarithmically with the number of BS antennas [5].
- Linear processing algorithms are sufficient to approach capacity for $A \gg K$, i.e., if the number of BS antennas is far greater than the number of served users [4].
- The effects of uncorrelated receiver noise and fast fading are eliminated completely, and transmissions to terminals within one cell do not interfere [4].

An essential requirement for massive MIMO communication systems is timely and accurate channel state information (CSI) for processing the signals from the large number of BS antennas. In high mobility scenarios, timely CSI is difficult to obtain, but crucial to guarantee reliability. There is a strong trend in sectors like automotive, industry, railway, or urban air mobility, to harvest the capabilities of 5G, but communication solutions must provide high reliability in these time-varying scenarios.

Therefore, this thesis addresses the following **objectives**:

- O1** Assess the impact of CSI prediction on the reliability of widely distributed massive MIMO communications systems in high mobility scenarios.
- O2** Utilize time-frequency diversity through orthogonal precoding (OP) and spatial diversity through widely distributed BS antennas to increase the reliability of massive MIMO systems.
- O3** Devise suitable measurement campaigns, gather empirical data to analyze the statistical properties of widely distributed massive MIMO systems, and confirm the assumptions and results in **O1** and **O2**.

1.2 Methodology, Contribution, and Outline

We choose four methods to achieve the objectives of this thesis, both on a theoretic and an empiric level:

- M1** Numerical simulation, and analysis of obtained results, to gain insight into measures that enable reliable communication in high mobility scenarios. Possible approaches include OP and CSI prediction (**O1**, **O2**).
- M2** Analytic derivations and analysis to deepen our understanding of CSI prediction capabilities and its impact on reliability (**O1**).
- M3** Design and implementation of a fully parallel massive MIMO channel sounding architecture suitable for high mobility scenarios, as well as conceptualization and realization of corresponding measurement campaigns (**O3**).
- M4** Numerical analysis of the empirical data gathered with **M3** to evaluate the impact of outdated CSI as well as the impact of different spatial BS antenna configurations (**O1**, **O2**, **O3**).

With the methodology provided above, we achieve several contributions that, as a whole, demonstrate the capabilities of massive MIMO to enable and support highly reliable communication in time-varying scenarios.

- We derive the instantaneous and asymptotic signal to interference and noise ratio (SINR) and the spectral efficiency (SE) of a time division duplex (TDD) massive MIMO system for a time-correlated fading process utilizing multi-step minimum mean square error (MMSE) Wiener prediction. This result generalizes the work of [6] for single-step AR(1) process prediction (**O1**; [7]).
- We prove and show by numerical simulation that the capability of massive MIMO to reduce the variance of the received signal power is independent of the CSI age, i.e., channel hardening is independent of channel aging. The CSI age mainly affects the SINR and thereby the SE (**O1**; [7]).
- We show that with the utilization of OP, the bit error rate (BER) performance of polynomial (Wiener) prediction approaches that of perfectly known CSI to within 2 dB (1 dB) for a velocity of 160 km/h at 3.5 GHz (**O1**; [8]).
- We investigate the dependence of the BER performance on the number of BS antennas and the prediction/precoding horizon (**O2**; [8]).
- We conduct the world-first fully parallel and coherent widely distributed array channel sounding measurements in a high mobility scenario with 32 BS antennas and two users (**O3**; [9]).
- We perform a comparative analysis of wireless propagation conditions for BS aperture sizes from 2 m to 46.5 m in terms of delay spread, Doppler spread, received power, and collinearity of the local scattering function (LSF) (**O3**; [9]–[11]).
- We evaluate channel hardening and effects of channel aging on the SINR in a widely distributed massive MIMO system based on the obtained measurement data (**O1**, **O2**, **O3**; [9]).

The contributions described in this thesis are presented to a large extent in the following papers:

[10] D. Löschenbrand, M. Hofer, L. Bernadó, G. Humer, B. Schrenk, S. Zelenbaba, and T. Zemen, “Distributed massive MIMO channel measurements in urban vehicular scenario”, in *13th European Conference on*

Antennas and Propagation (EuCAP), Krakow, Poland, 2019.

[11] D. Löschenbrand, M. Hofer, B. Rainer, and T. Zemen, "Empirical and simulated performance evaluation of distributed massive MIMO", in *Asilomar Conference on Signals, Systems, and Computers (ASILOMAR)*, 2019.

[8] D. Löschenbrand, M. Hofer, and T. Zemen, "Orthogonal precoding with channel prediction for high mobility massive MIMO", in *2020 IEEE 31st Annual International Symposium on Personal, Indoor and Mobile Radio Communications (PIMRC)*, 2020. DOI: 10.1109/PIMRC48278.2020.9217208.

[9] D. Löschenbrand, M. Hofer, L. Bernadó; S. Zelenbaba, and T. Zemen, "Towards cell-free massive MIMO: A measurement-based analysis", *IEEE Access*, 2022. DOI: 10.1109/ACCESS.2022.3200365.

[7] D. Löschenbrand, M. Hofer, and T. Zemen, "Spectral efficiency of time-variant massive MIMO using Wiener prediction", *IEEE Communications Letters*, 2023. DOI: 10.1109/LCOMM.2023.3242457

Chapter 2

Massive MIMO for Mobile Users

2.1 Contents of this Chapter

In this chapter, the paradigm of massive MIMO communication is introduced as an enabler for increased spectral and energy efficiency as well as high reliability of wireless links. The distinctive characteristic of a massive MIMO communication scheme is the large number of deployed BS antennas, each with a dedicated radio frequency (RF) chains that far outnumber the active user equipments (UEs) connected to it.

This approach, first put forward in [4], offers several key advantages: linear processing is almost capacity-achieving, small-scale fading is eliminated, and users can be served on the same time-frequency resource without interfering with each other. These favorable characteristics arise due to constructive superposition of all multipath contributions at the intended UE position, and random superposition everywhere else. However, timely and accurate CSI is essential for the required beamforming processing in a massive MIMO system, but hard to acquire in time-varying scenarios with user mobility.

In Section 2.2, the uplink of a massive MIMO system with several users is considered. CSI prediction as a promising means of enabling operation in time-varying scenarios is analyzed analytically and by numerical simulation. In Section 2.3, a reliability assessment is given in terms of SINR and channel hardening (**O1**). The contents of these sections are published in

[7] D. Löschenbrand, M. Hofer, and T. Zemen, "Spectral efficiency of time-variant massive MIMO using Wiener prediction", *IEEE Communications Letters*, 2023. DOI: 10.1109/LCOMM.2023.3242457.

In Section 2.4, the downlink of a massive MIMO system with a single user is considered. After introducing the signal model, methods to allow for operation in time-varying scenarios are introduced. A reliability assessment of the considered system is provided for different degrees of user mobility and varying number of BS antennas by means of a numerical link-level simulation (**O1**, **O2**). The contents of this section are published in

[8] D. Löschenbrand, M. Hofer, and T. Zemen, "Orthogonal precoding with channel prediction for high mobility massive MIMO", in *2020 IEEE 31st Annual International Symposium on Personal, Indoor and Mobile Radio Communications (PIMRC)*, 2020. DOI: 10.1109/PIMRC48278.2020.9217208.

Findings and conclusions are summarized in Section 2.5, and Section 2.6 provides related literature.

2.2 Multiple Mobile Users Case

Massive MIMO systems are an important enabling technology in current 5G deployments, providing improved SE and reliability compared to conventional MIMO. However, they still struggle to unlock their potential in high mobility scenarios, e.g., in automotive and industrial use cases.

The fundamental cause for this is the systems dependency on high quality and timely CSI for the communication channel from all users to all BS antenna elements for accurate beam-forming [4]. Currently, the only viable and scalable solution is the application of a TDD method and relying on channel reciprocity. In this case, CSI estimation with pilot symbols and their utilization for beam-forming must happen within the coherence time $T^{(\text{coh})}$ of the wireless channel. The coherence time is defined as the time duration that is required for the wireless channel to change significantly. A more stringent definition will be provided later.

In high mobility scenarios, that is in scenarios where the time delay between CSI estimation and its use for beam-forming is larger than the coherence time of the wireless channel, this approach inherently causes service degradation due to outdated CSI, also termed *channel aging* [9]. Channel aging causes an increase of the BER due to a reduction of the SINR. Mitigation strategies include (i) decreasing the time between uplink CSI acquisition and downlink beam-forming, (ii) OP to exploit time and frequency diversity, and (iii) CSI prediction, all of which will be addressed in the following.

In this section, we introduce a multi-user massive MIMO system employing channel prediction to analyze the uplink SE and quantify its degradation due to user mobility. Further, we investigate the variance of the received signal power around its mean for different prediction horizon lengths, i.e., how channel prediction influences channel hardening. This facilitates the reliability analysis of a massive MIMO system in terms of received signal power fluctuation. In this section, we discuss the uplink only. However, all results on SE apply for the downlink too, through the uplink-downlink duality [12, Theorem 4.8].

2.2.1 Signal Model

We consider an uplink massive MIMO system, where K users with single-antenna terminals $k \in \{1, \dots, K\}$ send pilots and data to a BS deploying A antenna elements $a \in \{1, \dots, A\}$, without neighboring cells. The notation we introduce for this system is largely based on [6], with the exception that only one cell is considered, as our focus mainly lies on the aspect of time variance of the bandlimited fading process and its impact on the SINR and SE. We assume an orthogonal frequency-division multiplexing (OFDM) system where the individual subcarriers are orthogonal and are therefore treated individually. The dependency on frequency is thus omitted in the considerations below to facilitate notation. The dependency on time is indicated by the index m .

The effects of the wireless channel on the scalar transmitted information symbol s_{km} are modeled by a complex scalar channel coefficient h_{kam} . The channel coefficients of one user k to all A BS antennas are collected in a channel vector

$$\mathbf{h}_{km} = [h_{k1m} \ h_{k2m} \ \dots \ h_{kAm}]^T \in \mathbb{C}^{A \times 1}. \quad (2.1)$$

The channel matrix

$$\mathbf{H}_m = [\mathbf{h}_{1m} \ \mathbf{h}_{2m} \ \dots \ \mathbf{h}_{Km}] \in \mathbb{C}^{A \times K} \quad (2.2)$$

contains the individual channel vectors of all users. Similarly, the beam-forming matrix

$$\mathbf{W}_m = [\mathbf{w}_{1m} \ \mathbf{w}_{2m} \ \dots \ \mathbf{w}_{Km}] \in \mathbb{C}^{A \times K} \quad (2.3)$$

contains the individual beam-forming vectors $\mathbf{w}_m \in \mathbb{C}^{A \times 1}$ for user k , all A BS antenna elements, and time index m .

The vector collecting the received symbols from all K users at time index m is

$$\hat{\mathbf{s}}_m = \mathbf{W}_m^H \mathbf{y}_m = \mathbf{W}_m^H \mathbf{H}_m \mathbf{s}_m + \mathbf{W}_m^H \mathbf{n}_m, \quad (2.4)$$

with P the average transmit power of each user, $\mathbf{s}_m \in \mathbb{C}^{K \times 1}$ the vector collecting the transmitted information symbols of all users, and $\mathbf{W}_m^H \mathbf{n}_m \sim \mathcal{CN}(\mathbf{0}, \frac{\sigma_n^2}{P} \mathbf{I}_K)$ denoting filtered complex Gaussian noise. Figure 2.1 shows a schematic of the receive combining signal model (2.4).

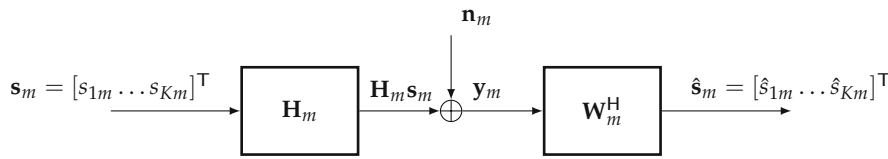


FIGURE 2.1: Receive combining matrix signal model for the massive MIMO uplink.

The spatial correlation matrix of the channel vector for user k is

$$\mathbf{R}_k = \mathbb{E} \left\{ \mathbf{h}_{km} \mathbf{h}_{km}^H \right\}. \quad (2.5)$$

Further, we assume local wide-sense stationarity of the fading process and a joint spatial and temporal covariance matrix

$$\mathbb{E} \left\{ \mathbf{h}_{km-\ell} \mathbf{h}_{km-\ell'}^H \right\} = \mathbf{r}_{\mathbf{h},|\ell'-\ell|} \mathbf{R}_k, \quad (2.6)$$

with $\mathbf{r}_{\mathbf{h},\ell}$ being the temporal correlation coefficient of the channel vector with time delay ℓ .

Note that the scalar approach in (2.6) intrinsically assumes, that the temporal correlation is the same for all antenna pairs (a, a') , which is valid if all BS antenna elements are collocated.

The temporal correlation coefficient $\mathbf{r}_{\mathbf{h},\ell}$ is useful to formally define the coherence time $T^{(\text{coh})}$ of the wireless channel [3, Sec. 6.5.4] as

$$T^{(\text{coh})} = T^{(\text{symb})} \ell' \quad (2.7)$$

where $T^{(\text{symb})}$ is the symbol duration. The threshold symbol index ℓ' is chosen such that

$$\mathbf{r}_{\mathbf{h},\ell} \geq 0.5, \quad \ell \leq \ell', \quad (2.8)$$

$$\mathbf{r}_{\mathbf{h},\ell} < 0.5, \quad \ell = \ell' + 1 \quad (2.9)$$

holds. In other words, the coherence time is defined as the time duration in which the temporal correlation coefficient $\mathbf{r}_{\mathbf{h},\ell}$ drops below 0.5. Figure 2.2 depicts the connection between coherence time and temporal correlation.

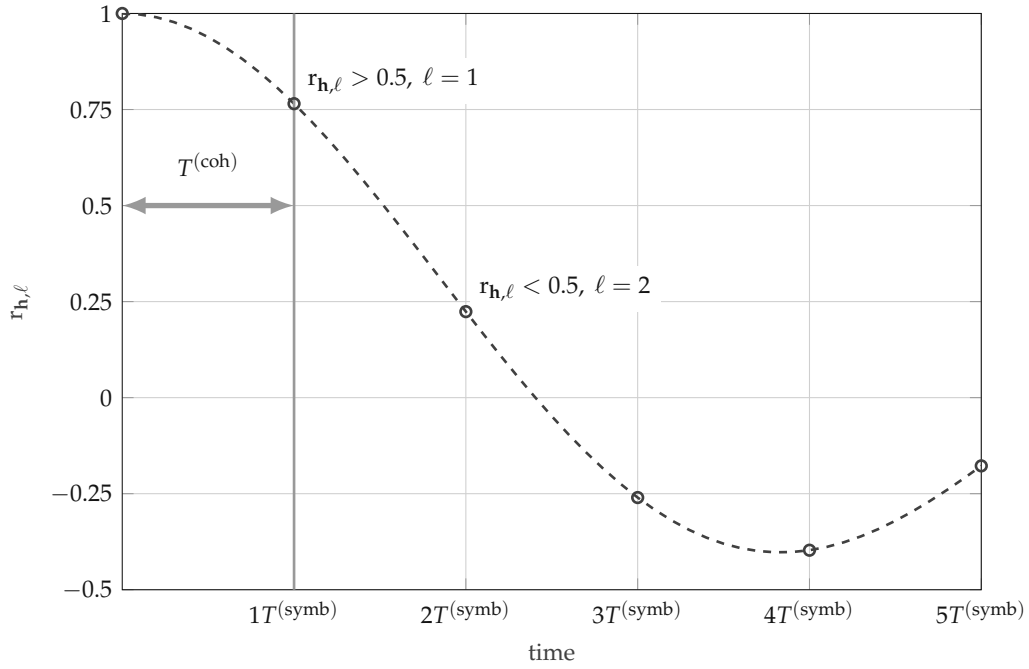


FIGURE 2.2: Exemplary temporal correlation coefficient $r_{h,\ell}$ and coherence time $T^{(\text{coh})}$.

The received symbol estimate from one single user k at the BS is

$$\begin{aligned}\hat{s}_{km} &= \mathbf{w}_{km}^H \mathbf{y}_m = \mathbf{w}_{km}^H \mathbf{H}_m \mathbf{s}_m + \mathbf{w}_{km}^H \mathbf{n}_m \\ &= \mathbf{w}_{km}^H \mathbf{h}_{km} s_{km} + \mathbf{w}_{km}^H \mathbf{n}_m + \sum_{k' \neq k} \mathbf{w}_{km}^H \mathbf{h}_{k'm} s_{k'm},\end{aligned}\quad (2.10)$$

where the first term in the second line is the scaled signal, the second term is filtered and scaled Gaussian noise $\mathbf{w}_{km}^H \mathbf{n}_m \sim \mathcal{CN}(0, \frac{\sigma_n^2}{P})$, and the third term is interference from other users $k' \neq k$. Figure 2.3 shows the equivalent receive combining signal model.

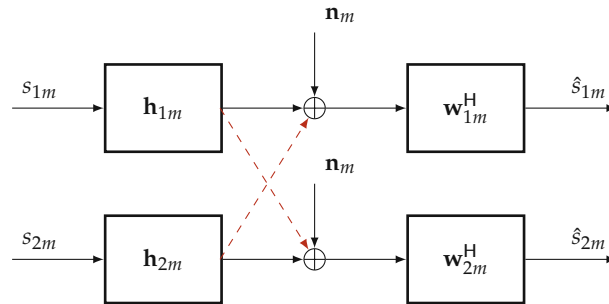


FIGURE 2.3: Equivalent receive combining matrix signal model for two users, where the red arrows indicate interference from other users.

2.2.2 Channel Estimation

For channel estimation, a single-cell approach similar to [6, Eq. (9)] is used to obtain noisy observations of the channel vector

$$\mathbf{y}_{km} = \mathbf{h}_{km} + \mathbf{n}_m. \quad (2.11)$$

They are filtered by the MMSE estimator [6] to obtain the channel vector estimate

$$\hat{\mathbf{h}}_{km} = \mathbf{R}_k \left(\frac{\sigma_n^2}{P} \mathbf{I}_A + \mathbf{R}_k \right)^{-1} \mathbf{y}_{km}, \quad (2.12)$$

distributed as $\hat{\mathbf{h}}_{km} \sim \mathcal{CN}(\mathbf{0}, \mathbf{\Theta}_{k10})$, where

$$\mathbf{\Theta}_{k10} = \mathbf{R}_k \left(\frac{\sigma_n^2}{P} \mathbf{I}_A + \mathbf{R}_k \right)^{-1} \mathbf{R}_k \quad (2.13)$$

denotes a special case of the covariance matrix $\mathbf{\Theta}_{kN\ell}$ with the number of pilots $N = 1$ and the prediction horizon $\ell = 0$.

2.2.3 Multi-Step Channel Prediction

Given the following matrices to ease notation

$$\boldsymbol{\delta}_{N\ell} = [\mathbf{r}_{\mathbf{h},\ell} \ \mathbf{r}_{\mathbf{h},\ell+1} \ \dots \ \mathbf{r}_{\mathbf{h},\ell+N-1}], \quad (2.14)$$

$$\boldsymbol{\Delta}_{N\ell} = \begin{bmatrix} \mathbf{r}_{\mathbf{h},\ell} & \mathbf{r}_{\mathbf{h},\ell+1} & \dots & \mathbf{r}_{\mathbf{h},\ell+N-1} \\ \mathbf{r}_{\mathbf{h},\ell+1} & \mathbf{r}_{\mathbf{h},\ell} & \dots & \mathbf{r}_{\mathbf{h},\ell+N-2} \\ \vdots & \vdots & \ddots & \vdots \\ \mathbf{r}_{\mathbf{h},\ell+N-1} & \mathbf{r}_{\mathbf{h},\ell+N-1} & \dots & \mathbf{r}_{\mathbf{h},\ell} \end{bmatrix}, \quad (2.15)$$

$$\mathbf{T}_{kN\ell} = \left[\boldsymbol{\Delta}_{N\ell} \otimes \mathbf{R}_k + \frac{\sigma_n^2}{P} \mathbf{I}_{AN} \right]^{-1}, \quad (2.16)$$

$$\mathbf{\Theta}_{kN\ell} = (\boldsymbol{\delta}_{N\ell} \otimes \mathbf{R}_k) \mathbf{T}_{kN0} (\boldsymbol{\delta}_{N\ell} \otimes \mathbf{R}_k)^H, \quad (2.17)$$

we find the linear Wiener multi-step predictor by extending the framework provided in [6] and the joint spatial and temporal correlation defined in (2.6).

Theorem 2.2.1 (Wiener multi-step predictor). *Given N consecutive pilot symbols, the optimal linear Wiener predictor $\mathbf{V}_{k\ell}$ with prediction horizon ℓ is*

$$\mathbf{V}_{k\ell} = (\boldsymbol{\delta}_{N\ell} \otimes \mathbf{R}_k) \mathbf{T}_{kN0}, \quad (2.18)$$

and the predicted channel vector $\tilde{\mathbf{h}}_{km+1}$ is

$$\tilde{\mathbf{h}}_{km+1} = \mathbf{V}_{k\ell+1} \tilde{\mathbf{y}}_{km-\ell}, \quad (2.19)$$

with

$$\tilde{\mathbf{y}}_{km-\ell} = \begin{bmatrix} \mathbf{y}_{km-\ell} \\ \mathbf{y}_{km-\ell-1} \\ \vdots \\ \mathbf{y}_{km-\ell-N+1} \end{bmatrix} \in \mathbb{C}^{AN \times 1}. \quad (2.20)$$

stacking N received pilot symbols delayed by ℓ .

Proof. We follow the approach in [6] but extend it to a general temporal fading model and multi-step prediction. We assume that N consecutive pilot symbols are used for prediction.

Suppose that the pilot symbols are outdated, e.g., only pilot symbols $\tilde{\mathbf{y}}_{km-\ell}$ with CSI acquisition delay $\ell > 0$ are available to predict \mathbf{h}_{km+1} . The optimal predictor [6] extended to multi-step prediction is then found by solving

$$\mathbb{E} \left\{ (\mathbf{h}_{km+1} - \mathbf{V}_{k\ell+1} \tilde{\mathbf{y}}_{km-\ell}) \tilde{\mathbf{y}}_{km-\ell}^H \right\} = \mathbf{0} \quad (2.21)$$

or, after reformulating,

$$\mathbf{V}_{k\ell+1} = \mathbb{E} \left\{ \mathbf{h}_{km+1} \tilde{\mathbf{y}}_{km-\ell}^H \right\} \mathbb{E} \left\{ \tilde{\mathbf{y}}_{km-\ell} \tilde{\mathbf{y}}_{km-\ell}^H \right\}^{-1}. \quad (2.22)$$

By using the channel estimation signal model in (2.11), the joint spatial and temporal correlation (2.6), and assuming that uncorrelated noise terms cancel for $\ell > 0$, we find the covariance matrix of two received pilot symbols with CSI acquisition delay ℓ to be

$$\mathbb{E} \left\{ \mathbf{y}_{km} \mathbf{y}_{km-\ell}^H \right\} = \begin{cases} \mathbf{r}_{\mathbf{h},0} \mathbf{R}_k + \frac{\sigma_n^2}{P}, & \ell = 0; \\ \mathbf{r}_{\mathbf{h},\ell} \mathbf{R}_k, & \text{otherwise.} \end{cases} \quad (2.23)$$

The covariance matrix of the stacked pilot symbols is then calculated with (2.20) and (2.23) as

$$\begin{aligned} \mathbb{E} \left\{ \tilde{\mathbf{y}}_{km-\ell} \tilde{\mathbf{y}}_{km-\ell}^H \right\} &= \mathbb{E} \left\{ \tilde{\mathbf{y}}_{km} \tilde{\mathbf{y}}_{km}^H \right\} \\ &= \Delta_{N0} \otimes \mathbf{R}_k + \frac{\sigma_n^2}{P} \mathbf{I}_{AN} \\ &= \mathbf{T}_{kN0}^{-1}. \end{aligned} \quad (2.24)$$

The first line of (2.24) holds since wide-sense stationarity is assumed, i.e., the statistics are independent of an arbitrary time shift ℓ for the considered frame duration and prediction horizon [13].

With (2.11), (2.6) and (2.20), the cross-correlation between the true channel and the stacked pilot symbols is

$$\begin{aligned} \mathbb{E} \left\{ \mathbf{h}_{km+1} \tilde{\mathbf{y}}_{km-\ell}^H \right\} &= [\mathbf{r}_{\mathbf{h},\ell+1} \mathbf{R}_k, \dots, \mathbf{r}_{\mathbf{h},\ell+N} \mathbf{R}_k] \\ &= \delta_{N,\ell+1} \otimes \mathbf{R}_k. \end{aligned} \quad (2.25)$$

Substituting (2.24) and (2.25) into (2.22) gives (2.19).

The predicted channel vector is thus

$$\tilde{\mathbf{h}}_{km+1} = \mathbf{V}_{k\ell+1} \tilde{\mathbf{y}}_{km-\ell}, \quad (2.26)$$

and its distribution $\tilde{\mathbf{h}}_{km+1} \sim \mathcal{CN}(\mathbf{0}, \Theta_{kN\ell+1})$ depends on the prediction horizon ℓ [6]. \square

The mean squared error (MSE) of the predicted channel vector \mathbf{h}_{km+1} , given a prediction horizon of ℓ , is calculated as

$$\begin{aligned}
\epsilon_{kN\ell}(\tilde{\mathbf{h}}_{km+1}, \mathbf{h}_{km+1}) &= \mathbb{E} \left\{ \|\mathbf{h}_{km+1} - \mathbf{V}_{k\ell+1} \tilde{\mathbf{y}}_{km-\ell}\|_{\mathbb{F}}^2 \right\} \\
&= \text{tr} \left\{ \mathbb{E} \left\{ (\mathbf{h}_{km+1} - \mathbf{V}_{k\ell+1} \tilde{\mathbf{y}}_{km-\ell}) \mathbf{h}_{km+1}^H \right\} \right\} \\
&= \text{tr} \left\{ \mathbb{E} \left\{ \mathbf{h}_{km} \mathbf{h}_{km}^H \right\} - \mathbf{V}_{k\ell+1} \mathbb{E} \left\{ \tilde{\mathbf{y}}_{km-\ell} \mathbf{h}_{km+1}^H \right\} \right\} \\
&= \text{tr} \{ \mathbf{R}_k - \mathbf{\Theta}_{kN\ell+1} \}. \tag{2.27}
\end{aligned}$$

Note that in the case of $N = 1$, i.e., only one pilot symbol is used, (2.14) and (2.15) each reduce to the scalar temporal correlation coefficient and the predicted channel becomes $\tilde{\mathbf{h}}_{km+1} = \mathbf{V}_{k\ell+1} \tilde{\mathbf{y}}_{km-\ell} = \mathbf{r}_{\mathbf{h},\ell} \hat{\mathbf{h}}_{km-\ell+1}$. Simply put, with only one pilot at hand, the evolution of the channel cannot be tracked, and the best prediction is the weighted aged channel estimate.

2.3 Spectral Efficiency and Channel Hardening for Multiple Users

By introducing the predicted channel $\tilde{\mathbf{h}}_{km+1}$ in (2.28), we obtain the estimated received symbol from one single user k at the BS after receive combining as

$$\begin{aligned}
\hat{s}_{km+1} &= \mathbf{w}_{km+1}^H \tilde{\mathbf{h}}_{km+1} s_{km+1} + \mathbf{w}_{km}^H \mathbf{n}_{m+1} \\
&\quad + \mathbf{w}_{km+1}^H (\mathbf{h}_{km+1} - \tilde{\mathbf{h}}_{km+1}) s_{km+1} \\
&\quad + \sum_{k' \neq k} \mathbf{w}_{km+1}^H \mathbf{h}_{k'm+1} s_{k'm+1}. \tag{2.28}
\end{aligned}$$

The first term is the intended signal multiplied with the effective channel gain

$$\gamma_{km+1} = \mathbf{w}_{km+1}^H \tilde{\mathbf{h}}_{km+1}, \tag{2.29}$$

the second term is additive noise, the third term is the channel prediction error considered as noise, and the fourth term is interference from other users $k' \neq k$.

The choice of the beam-forming vectors in \mathbf{W}_m greatly affects the capability of a massive MIMO system to suppress the interference from other users. In this work, we analyze maximum ratio combining (MRC) and regularized zero-forcing (RZF) as common choices of beam-forming vectors [4], [14]:

$$\mathbf{W}_m = [\mathbf{w}_{1m} \ \mathbf{w}_{2m} \ \dots \ \mathbf{w}_{K_m}] = \begin{cases} \tilde{\mathbf{H}}_m, & \text{MRC;} \\ \tilde{\mathbf{H}}_m (\tilde{\mathbf{H}}_m^H \tilde{\mathbf{H}}_m)^{-1}, & \text{ZF;} \\ \tilde{\mathbf{H}}_m \left(\tilde{\mathbf{H}}_m^H \tilde{\mathbf{H}}_m + \frac{\sigma_n^2}{P} \mathbf{I}_K \right)^{-1}, & \text{RZF;} \end{cases} \tag{2.30}$$

where the columns of the predicted channel matrix $\tilde{\mathbf{H}}_m$ are composed of the predicted channel vectors similar to (2.2).

2.3.1 Instantaneous and Asymptotic SINR

Considering the signal model (2.28) and assuming channel prediction with prediction horizon ℓ at the BS, the instantaneous signal power is given as the squared absolute

value of the effective channel gain γ_{km+1} and yields

$$S_{kl} = |\gamma_{km+1}|^2 = \left| \mathbf{w}_{km+1}^H \tilde{\mathbf{h}}_{km+1} \right|^2. \quad (2.31)$$

The instantaneous interference and noise power is defined as the sum of all interference/noise contributions in (2.28)

$$I_{kl} = \frac{\sigma_n^2}{\sqrt{P}} \mathbf{w}_{km+1}^H \tilde{\mathbf{h}}_{km+1} + \left| \mathbf{w}_{km+1}^H (\mathbf{h}_{km+1} - \tilde{\mathbf{h}}_{km+1}) \right|^2 + \sum_{k' \neq k} \left| \mathbf{w}_{km+1}^H \mathbf{h}_{k'm+1} \right|^2. \quad (2.32)$$

The instantaneous SINR is defined as the ratio of instantaneous signal to interference and noise power

$$\eta_{kl} = \frac{S_{kl}}{I_{kl}} = \frac{\left| \mathbf{w}_{km+1}^H \tilde{\mathbf{h}}_{km+1} \right|^2}{\frac{\sigma_n^2}{\sqrt{P}} \mathbf{w}_{km+1}^H \tilde{\mathbf{h}}_{km+1} + \left| \mathbf{w}_{km+1}^H (\mathbf{h}_{km+1} - \tilde{\mathbf{h}}_{km+1}) \right|^2 + \sum_{k' \neq k} \left| \mathbf{w}_{km+1}^H \mathbf{h}_{k'm+1} \right|^2}. \quad (2.33)$$

Theorem 2.3.1. *The asymptotic deterministic SINR $\bar{\eta}_{kl} = \lim_{A \rightarrow \infty} \eta_{kl}$ with MRC is calculated as*

$$\bar{\eta}_{kl} = \frac{\bar{S}_{kl}}{\bar{I}_{kl}} = \frac{\left| \text{tr}\{\mathbf{\Theta}_{kN\ell+1}\} \right|^2}{\frac{\sigma_n^2}{\sqrt{P}} \text{tr}\{\mathbf{\Theta}_{kN\ell+1}\} + \text{tr}\{\mathbf{\Theta}_{kN\ell+1} (\mathbf{R}_k - \mathbf{\Theta}_{kN\ell+1})\} + \sum_{k' \neq k} \text{tr}\{\mathbf{\Theta}_{kN\ell+1} \mathbf{R}_{k'}\}}. \quad (2.34)$$

Proof. Since MRC is assumed, the beam-forming vector is computed as $\mathbf{w}_{km+1} = \tilde{\mathbf{h}}_{km+1}$. For $A \rightarrow \infty$, the instantaneous signal power (2.31) converges towards its asymptotic deterministic equivalent [6]

$$\bar{S}_{kl} = \lim_{A \rightarrow \infty} \frac{1}{A^2} S_{kl} = \left| \text{tr}\{\mathbf{\Theta}_{kN\ell+1}\} \right|^2, \quad (2.35)$$

with the covariance matrix $\mathbf{\Theta}_{kN\ell+1}$ defined in (2.17). Similarly, the instantaneous interference and noise power (2.32) converges toward its asymptotic deterministic equivalent [6]

$$\begin{aligned} \bar{I}_{kl} &= \lim_{A \rightarrow \infty} \frac{1}{A^2} I_{kl} \\ &= \frac{\sigma_n^2}{\sqrt{P}} \text{tr}\{\mathbf{\Theta}_{kN\ell+1}\} + \text{tr}\{\mathbf{\Theta}_{kN\ell+1} (\mathbf{R}_k - \mathbf{\Theta}_{kN\ell+1})\} + \sum_{k' \neq k} \text{tr}\{\mathbf{\Theta}_{kN\ell+1} \mathbf{R}_{k'}\} \end{aligned} \quad (2.36)$$

as the number of BS antenna elements grows. The asymptotic deterministic SINR is therefore found as the ratio $\bar{S}_{kl}/\bar{I}_{kl}$ as specified in (2.34). \square

2.3.2 Ergodic and Asymptotic Spectral Efficiency

Similar to [6], we define the uplink ergodic achievable SE of user k with prediction horizon ℓ as

$$\text{SE}_{kl} = \mathbb{E} \left\{ \log_2 (1 + \eta_{kl}) \right\}, \quad (2.37)$$

where the expectation is over channel realizations. In the asymptotic case with the number of BS antenna elements $A \rightarrow \infty$, the SINR is deterministic and the uplink

asymptotic achievable SE of user k with prediction horizon ℓ is [6]

$$\overline{\text{SE}}_{k\ell} = \log_2(1 + \bar{\eta}_{k\ell}). \quad (2.38)$$

Both (2.37) and (2.38) do not take into account the number of uplink pilot symbols N that are necessary for prediction, as well as the number of necessary guard symbols N_G . A fair comparison that takes into account uplink overhead is thus provided by the uplink achievable block SE of user k with block length M , number of pilots N , and number of guard symbols N_G [4], [12]

$$\text{SE}_{kMN} = \frac{1}{M + N + N_G} \sum_{\ell=1}^M \text{SE}_{k\ell}. \quad (2.39)$$

2.3.3 Channel Hardening

Channel hardening refers to the phenomenon of the effective channel gain $\gamma_{km+1} = \mathbf{w}_{km+1}^H \tilde{\mathbf{h}}_{km+1}$ in (2.29) fluctuating only marginally around its mean [15],

$$\frac{\gamma_{km+1}}{\mathbb{E}\{\gamma_{km+1}\}} \rightarrow 1, \text{ as } A \rightarrow \infty. \quad (2.40)$$

To assess if channel hardening is occurring, we investigate the ratio of the effective gain variance to its squared mean

$$\beta_{k\ell} = \frac{\text{Var}\{\gamma_{km+1}\}}{\mathbb{E}\{\gamma_{km+1}\}^2}, \quad (2.41)$$

similar to [15]–[17]. Low values of $\beta_{k\ell}$ indicate a low probability of the channel gain γ_{km+1} deviating significantly from its mean.

Theorem 2.3.2 (Channel hardening). *Let $N = 1$ and $\mathbf{w}_{km+1} = \mathbf{r}_{\mathbf{h},\ell} \hat{\mathbf{h}}_{km-\ell+1}$ (i.e., MRC is applied), then the channel hardening metric $\beta_{k\ell}$ in (2.41) is independent of the prediction horizon ℓ .*

Proof. We acknowledge that, for $N = 1$, the predicted channel vector $\tilde{\mathbf{h}}_{km+1}$ is the outdated channel estimate decreased by its temporal correlation coefficient, i.e., $\tilde{\mathbf{h}}_{km+1} = r_{\mathbf{h},\ell} \hat{\mathbf{h}}_{km-\ell+1}$. Further, by applying MRC, the beam-forming vector becomes $\mathbf{w}_{km+1} = r_{\mathbf{h},\ell} \hat{\mathbf{h}}_{km-\ell+1}$. We then calculate

$$\begin{aligned} \mathbb{E}\{\gamma_{km+1}\} &= \mathbb{E}\left\{\mathbf{w}_{km+1}^H \tilde{\mathbf{h}}_{km+1}\right\} \\ &= r_{\mathbf{h},\ell}^2 \mathbb{E}\left\{\hat{\mathbf{h}}_{km-\ell+1}^H \hat{\mathbf{h}}_{km-\ell+1}\right\} \\ &= r_{\mathbf{h},\ell}^2 \text{tr}\{\mathbf{\Theta}_{k10}\}, \end{aligned} \quad (2.42)$$

where the third line follows from (2.12), and

$$\begin{aligned} \text{Var}\{\gamma_{km+1}\} &= \mathbb{E}\left\{\left(\mathbf{w}_{km+1}^H \tilde{\mathbf{h}}_{km+1}\right)^2 - \mathbb{E}\left\{\mathbf{w}_{km+1}^H \tilde{\mathbf{h}}_{km+1}\right\}^2\right\} \\ &= r_{\mathbf{h},\ell}^4 \mathbb{E}\left\{\left(\hat{\mathbf{h}}_{km-\ell+1}^H \hat{\mathbf{h}}_{km-\ell+1}\right)^2 - \text{tr}\{\mathbf{\Theta}_{k10}\}^2\right\} \\ &= r_{\mathbf{h},\ell}^4 \mathbb{E}\left\{\left(\hat{\mathbf{h}}_{km}^H \hat{\mathbf{h}}_{km}\right)^2 - \text{tr}\{\mathbf{\Theta}_{k10}\}^2\right\}. \end{aligned} \quad (2.43)$$

We plug (2.42) and (2.43) into (2.41) to get

$$\beta_{k\ell} = \frac{\mathbb{E} \left\{ \left(\hat{\mathbf{h}}_{km}^H \hat{\mathbf{h}}_{km} \right)^2 - \text{tr}\{\mathbf{\Theta}_{k10}\}^2 \right\}}{\text{tr}\{\mathbf{\Theta}_{k10}\}^2}, \quad (2.44)$$

which is independent of the prediction horizon ℓ . \square

While $\beta_{k\ell}$ is time-dependent in general when employing RZF, we show empirically in the next section that its variation is negligible compared to the impact of the number of BS antenna elements on channel hardening.

2.3.4 Numeric Results

We use a Monte-Carlo simulation to verify the uplink ergodic and asymptotic SE and channel hardening results under the influence of aged CSI and multi-step Wiener prediction. The expectation and variance in (2.37) and (2.41) are numerically estimated as the mean over random channel realizations. The random variable realizations are drawn according to the distributions specified in Section 2.2. The number of runs for the simulation is 20000.

Channel vector realizations with proper statistics in (2.28) are calculated using the approach outlined in [18], [19] with 400 paths and one tap. We consider Clarke's model $\mathbf{r}_{h,\ell} = J_0(2\pi f_D T_s \ell)$ for the temporal correlation coefficient, where J_0 denotes the Bessel function of the first kind and $f_D T_s$ denotes the maximum Doppler shift f_D normalized by the symbol duration T_s . This is more suitable for modeling a band limited fading processes, compared to the unbounded Doppler spectrum of the AR(1) model used in [6]. It also provides a direct relation between correlation in time and maximum Doppler shift. In the simulations, we set the normalized Doppler shift to $f_D T_s = 0.04$, which corresponds to a velocity of 172 km/h at a carrier frequency of 3.5 GHz (wavelength $\lambda = 8.6$ cm) and a symbol duration $T_s = 71.4 \mu\text{s}$. The number of BS antenna elements is $A = 64$ unless stated otherwise.

We note an excellent match between the SE in (2.37), simulated with $A = 64$ BS antenna elements, and the asymptotic SE in (2.38) for MRC beam-forming, shown in Fig. 2.4. Channel prediction with a higher number of pilots $N > 1$ increases the SE considerably and prevents sudden drops (caused by the temporal correlation function $\mathbf{r}_{h,\ell}$ approaching zero). For a prediction horizon $\ell = 7$ (equivalent to a movement of the user by 0.28λ since CSI acquisition), utilizing four instead of one pilot symbol doubles the achievable SE from 2.2 bit/s/Hz to 4.3 bit/s/Hz.

Figure 2.5 shows significant achievable SE improvements in the most relevant region $\ell \leq 10$ when choosing RZF over MRC. For a prediction horizon $\ell = 7$, utilizing four instead of one pilot symbol increases the achievable SE from 2.5 bit/s/Hz to 5.2 bit/s/Hz. We also note that for $\ell \geq 5$, the SE with an SNR of 6 dB and $N = 4$ is superior to the SE with an SNR of 12 dB and $N = 1$, highlighting the importance of channel prediction.

Figure 2.6 shows a boxplot of the distribution of $\beta_{k\ell}$ over the prediction horizon ℓ for different numbers of BS antenna array elements $A \in [8, 128]$. The whiskers of the boxes, indicating the interval from minimum to maximum of $\beta_{k\ell}$ over ℓ , remain close to its median value (red), irrespective of the number of BS antennas A . We verify that channel hardening is indeed largely independent of the prediction horizon ℓ and is mostly determined by the number of BS antenna array elements.

Figure 2.7 shows the SE for different SNR values P/σ_n^2 with $N = 4$ pilot symbols utilized and $A = 64$ BS antennas. For small values $\ell \in \{1, 2\}$ of the prediction

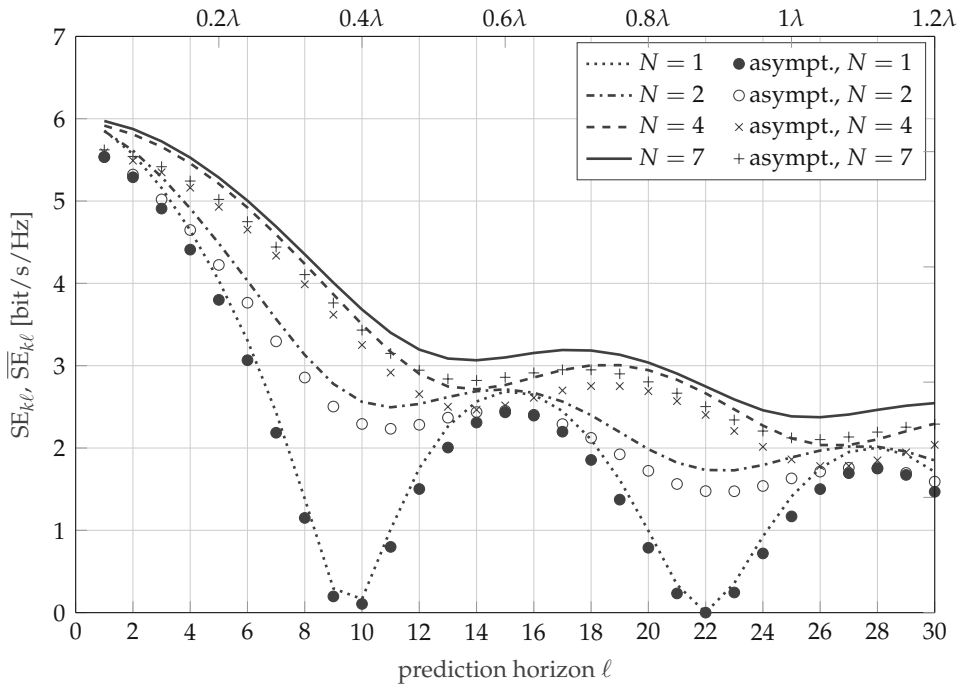


FIGURE 2.4: Ergodic and asymptotic achievable $SE_{k\ell}$ over prediction horizon ℓ for a normalized Doppler $f_D T_s = 0.04$, an SNR $\frac{P}{\sigma_n^2} = 12$ dB, and MRC beam-forming. The distance in terms of the wavelength λ corresponding to a given prediction horizon is given as second x -axis.

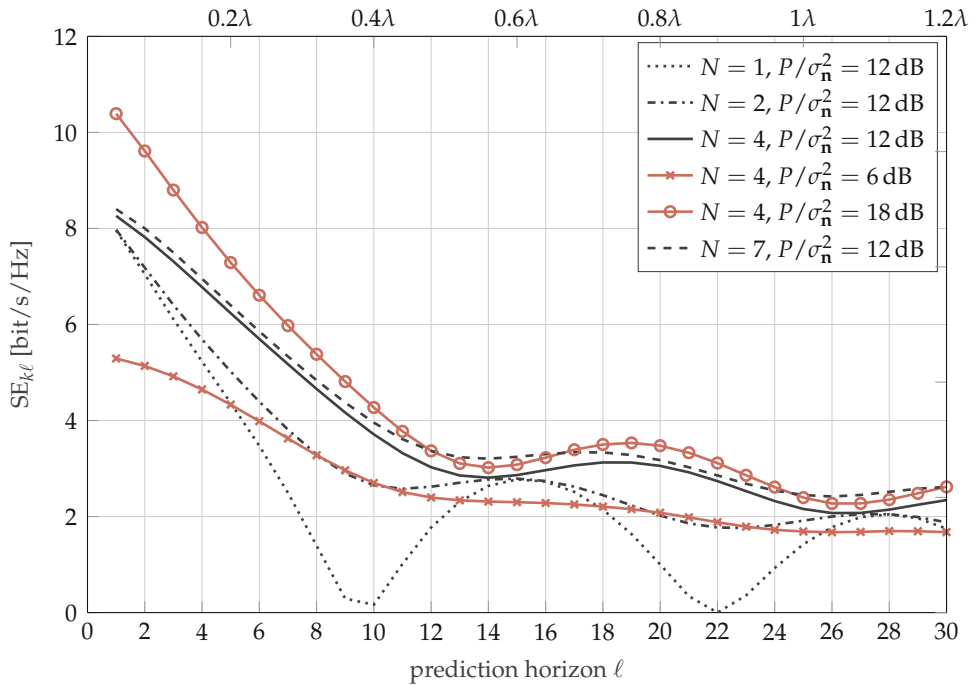


FIGURE 2.5: $SE_{k\ell}$ over prediction horizon ℓ for a normalized Doppler $f_D T_s = 0.04$ and RZF beam-forming. The distance in terms of the wavelength λ corresponding to a given prediction horizon is given as second x -axis.

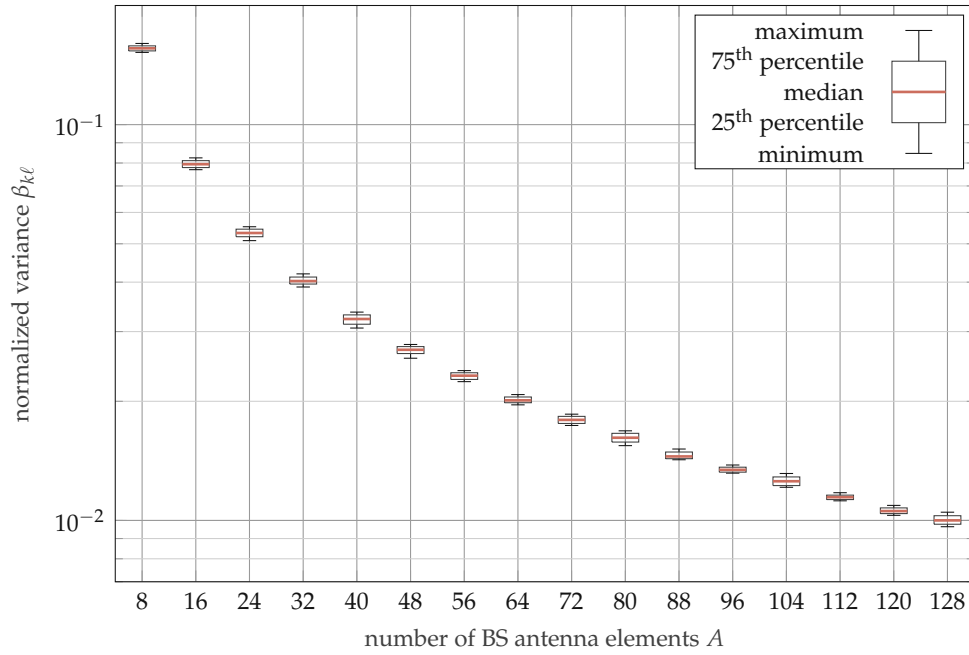


FIGURE 2.6: Boxplot of the channel hardening coefficient $\beta_{k\ell}$ (normalized variance of effective channel gain) distribution over prediction horizon $\ell \in \{0, \dots, 30\}$ for different number of BS antennas, $A \in [8, 128]$. The normalized Doppler $f_D T_s = 0.04$, the SNR $\frac{P}{\sigma_n^2} = 12$ dB, the number of pilots $N = 4$, and the beam-forming method is RZF. The small variance of $\beta_{k\ell}$ demonstrates that the channel hardening in massive MIMO is basically independent of the CSI age.

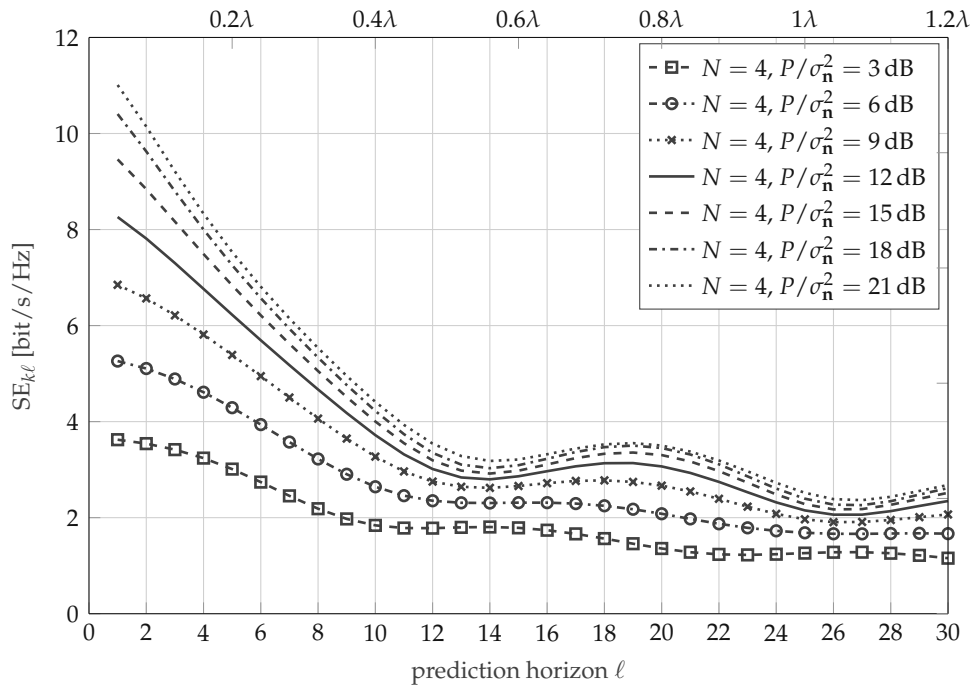


FIGURE 2.7: $SE_{k\ell}$ over prediction horizon ℓ for a normalized Doppler $f_D T_s = 0.04$ and RZF beam-forming. The number of BS antennas $A = 64$. The distance in terms of the wavelength λ corresponding to a given prediction horizon is given as second x -axis.

horizon, we clearly observe the logarithmic dependency of the SE on the SINR $\eta_{k\ell}$. However, for larger values $\ell > 10$, prediction quality has deteriorated so much that investing more power does not significantly increase the SE.

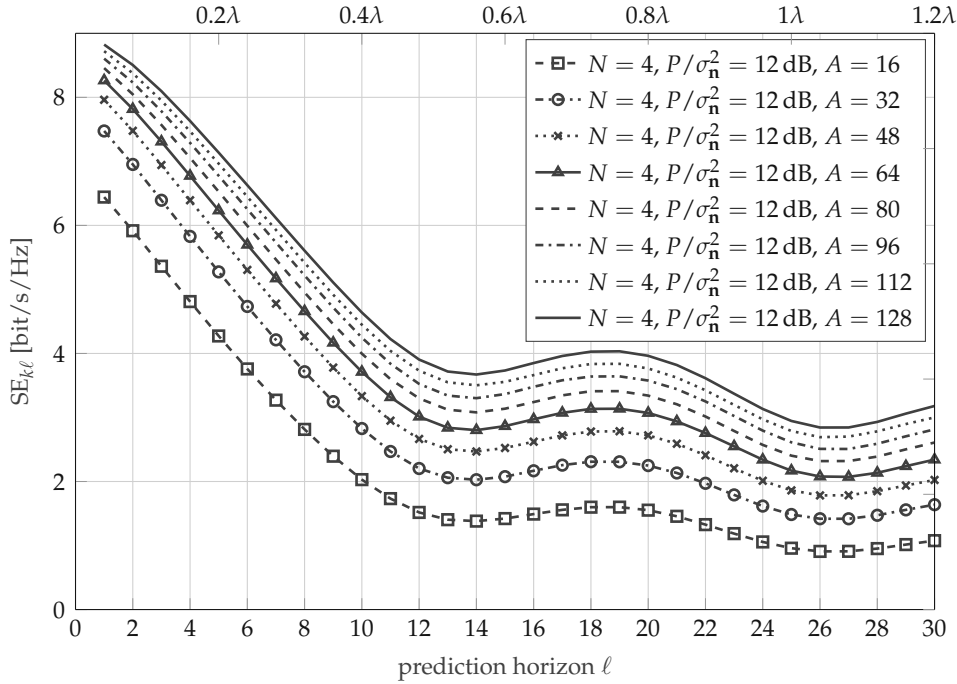


FIGURE 2.8: $SE_{k\ell}$ over prediction horizon ℓ for a normalized Doppler $f_D T_s = 0.04$ and RZF beam-forming. The distance in terms of the wavelength λ corresponding to a given prediction horizon is given as second x-axis.

Figure 2.8 shows the SE for different numbers of BS antenna elements $A \in [16, 128]$ with an SNR $P/\sigma_n^2 = 12$ dB and $N = 4$ pilot symbols. The logarithmic dependency of the SE on the number of BS antennas A is immediately visible, as expected when considering (2.37). The decrease in SE for growing prediction horizon ℓ is similar for different numbers of BS antennas at approximately 5 bit/s/Hz for 0.5λ distance traveled.

Figure 2.9 shows the achievable block SE_{kMN} in (2.39) that takes into account the block length M , the number of pilots N , and number of guard symbols N_G . We see that the mean SE over a block of length M is highest for very short blocks $M = 5$ and only $N = 1$ pilot symbol, which intuitively makes sense. In a rapidly changing wireless channel, it would be beneficial to receive CSI information as frequently as possible. This highlights a crucial limitation of CSI prediction methods: the reduction of the mean SE over a certain period of time due to pilot overhead. However, the timing of uplink and downlink schedule depends on many factors and can therefore not be chosen arbitrarily to accommodate users with high mobility. CSI prediction is therefore seen as a viable method to ensure high SE even with larger block length. This can be seen in Fig. 2.9, where utilizing CSI prediction with $N = 3$ pilot symbols and a block length $M = 10$ yields a block SE of 3.78 bit/s/Hz, while the optimal configuration with $M = 5$ and $N = 1$ yields 3.83 bit/s/Hz. Moreover, utilizing three or four pilot symbols gives similar SE over a wide range of block lengths, with only slowly declining values towards higher block lengths.

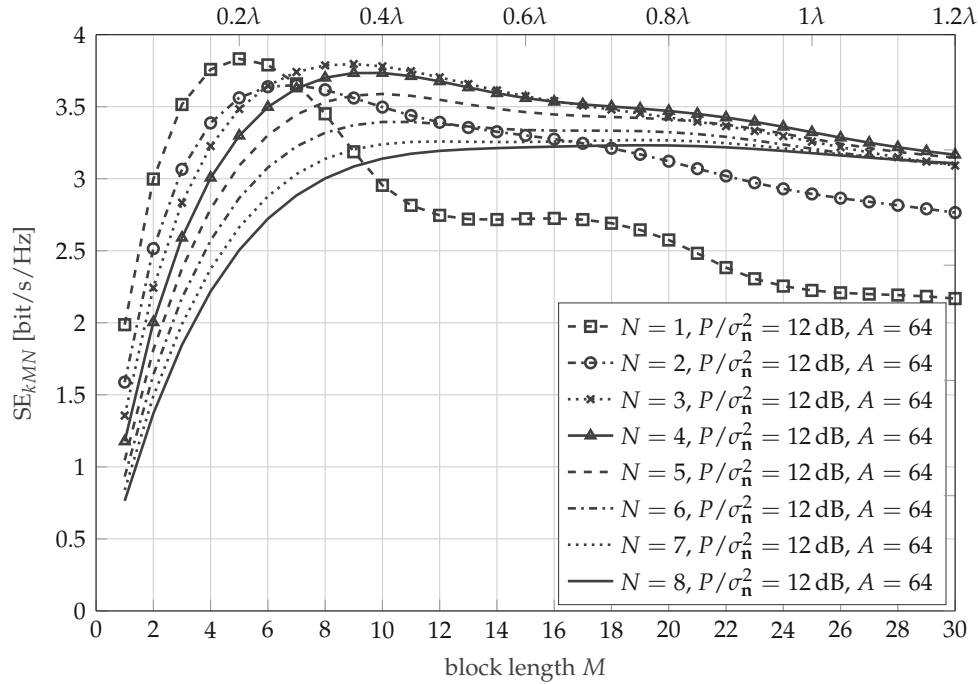


FIGURE 2.9: SE_{kMN} for block length M , a normalized Doppler $f_D T_s = 0.04$, and RZF beam-forming. The distance in terms of the wavelength λ corresponding to a given block length is given as second x -axis.

2.4 Single Mobile User Case

As we saw in the previous section, massive MIMO systems struggle to unlock their potential in high mobility scenarios, where CSI acquisition and beam-forming does not occur within the coherence time of the wireless channel. In this case, i.e., if channel aging occurs, the BER increases due to a reduction of the SINR. Mitigation strategies include decreasing the time between uplink CSI acquisition and downlink beam-forming and CSI prediction. Additionally, a method known as OP is considered as candidate to enable reliable massive MIMO applications with high mobility. OP spreads transmitted information in time and frequency to take advantage of diversity in those domains (rather than in space as massive MIMO does) and thereby increases resilience towards fading of individual components in the time-frequency grid. In what follows, OP and its interplay with CSI prediction is investigated.

2.4.1 Orthogonal Precoding Signal Model

We consider a massive MIMO downlink system similar to the previous section, where a BS with a large number of antennas A transmits to single-antenna UEs in a time-varying scenario. We focus on one UE for ease of notation, but the given signal model can readily be extended to several users by means of the multi-user signal model introduced in the previous section.

The underlying multiplexing scheme is assumed to be TDD, the modulation is OFDM and the transmission takes place in a blocked manner, thus M time samples and Q frequency samples are grouped in one block. To obtain the vectorized transmit symbols $\mathbf{s} \in \mathbb{C}^{QM \times 1}$, the vectorized information symbols $\mathbf{b} \in \mathbb{C}^{QM \times 1}$ are spread over a time-frequency block of size $M \times Q$, as described in [17], via the orthogonal

spreading matrix $\mathbf{C} \in \mathbb{C}^{QM \times QM}$, as

$$\mathbf{s} = \mathbf{C}\mathbf{b}. \quad (2.45)$$

This approach is in the following referred to as OP.

Suitable spreading matrices are derived from orthogonal basis sets such as the discrete symplectic Fourier transform (DSFT) [20], Walsh-Hadamard or discrete prolate spheroidal (DPS) sequences [21]. The rationale for spreading the information symbols over time and frequency is to leverage diversity of the doubly-selective propagation channel to mitigate fading and the effects of channel aging [17]. In [17], it has been shown that all constant modulus spreading sequences achieve the same performance. For easier comparison with previous work on DSFT, and given its efficient implementation with fast Fourier transforms (FFTs), we use the DSFT sequences for spreading in this work.

The time index is denoted by $m \in \{0, \dots, M-1\}$ and the sub-carrier index is denoted by $q \in \{0, \dots, Q-1\}$. With $\text{vec}(\cdot)$ denoting vectorization, we compactly write the vectorized matrix $\mathbf{t} = \text{vec}(\mathbf{T})$ with elements $(\mathbf{T})_{ij} = t_{ij}$ as $\mathbf{t} = \text{vec}(t_{ij})$.

The vectorized received symbols $\hat{\mathbf{s}} = \text{vec}(s_{qm}) \in \mathbb{C}^{QM \times 1}$ at the UE in a system applying OP are then modeled as

$$\hat{\mathbf{s}} = \mathbf{H}^H \mathbf{W} \mathbf{s} + \mathbf{n}, \quad (2.46)$$

with the massive MIMO channel matrix

$$\mathbf{H} = \begin{bmatrix} \text{diag}(\mathbf{h}_1) \\ \vdots \\ \text{diag}(\mathbf{h}_A) \end{bmatrix} \in \mathbb{C}^{QMA \times QM} \quad (2.47)$$

and the (downlink) beam-forming matrix

$$\mathbf{W} = \begin{bmatrix} \text{diag}(\mathbf{w}_1) \\ \vdots \\ \text{diag}(\mathbf{w}_A) \end{bmatrix} \in \mathbb{C}^{QMA \times QM}. \quad (2.48)$$

The individual channel vectors $\mathbf{h}_a = \text{vec}(h_{aqm}) \in \mathbb{C}^{QM \times 1}$ contain QM time-frequency channel coefficients from BS antenna a to the UE. They are diagonalized and stacked to form the channel matrix \mathbf{H} . Likewise, the individual beam-forming vectors $\mathbf{w}_a \in \mathbb{C}^{QM \times 1}$ are diagonalized and stacked to form the beam-forming matrix \mathbf{W} . Additive noise is denoted by $\mathbf{n} \sim \mathcal{CN}(\mathbf{0}, \sigma_n^2 \mathbf{I}_{QM})$, with σ_n^2 denoting the noise variance. We normalize the channel matrix $\mathbb{E} \{ \|\mathbf{H}\|_2^2 \} = QM$ such that the array gain is not taken into account. The downlink SNR is then given by $1/\sigma_n^2$.

2.4.2 Note on Interplay of Channel Aging and Channel Hardening

We showed in Section 2.2 that channel hardening is largely independent of channel aging, and that these two effects can be investigated separately. In practice, this means that channel hardening always occurs in favorable propagation conditions, regardless of the CSI age and beam-forming quality. The effective channel gain γ_m will become quasi-deterministic if the number of BS antennas is large. The important takeaway is that its mean, however, is heavily impacted by channel aging. Moreover, channel hardening can mitigate issues introduced by channel aging, as a quasi-deterministic

2.4.3 Channel Prediction Methods

The general framework in which we investigate channel prediction algorithms is based on the 5G new radio (NR) self-contained TDD slot structure. It allows to carry $N \in \{1, 2, 4\}$ consecutive SRS symbols within the last six symbols of one slot in the uplink. With this measure, timely CSI is acquired at the BS before downlink beam-forming. Figure 2.10 shows the slot structure with eight downlink data symbols, two guard symbols and four uplink SRS symbols at the end of the slot [23]. Assuming a subcarrier spacing of 15 kHz, the slot duration equals the sub-frame duration at $T^{(\text{slot})} = 1$ ms and the symbol duration is assumed to be $T^{(\text{symb})} = T^{(\text{slot})}/14 = 71.43 \mu\text{s}$.

The goal of the channel prediction schemes is to predict the CSI for the downlink symbols given the four uplink SRS symbols from the preceding slot. We consider prediction on a per sub-carrier basis and therefore drop the subcarrier index q . The channel vectors $\mathbf{h}_a = [h_{a1} \dots h_{aM}]^T \in \mathbb{C}^{M \times 1}$ from BS antenna a to the UE reduce to time series vectors with the block length M . Further, the SRS channel coefficients \hat{h}_{am} are estimated in the uplink from known SRS channel coefficients $(\mathbf{s})_m = s_m^{(\text{SRS})}$ by

$$\hat{h}_{am} = \frac{h_{am}s_m^{(\text{SRS})} + n_{am}}{s_m^{(\text{SRS})}} = h_{am} + \hat{n}_{am}. \quad (2.49)$$

The additive white Gaussian noise process $\hat{n}_{am} \sim \mathcal{CN}(0, \sigma_{\hat{n}}^2)$ is assumed stationary over one slot duration and independent of a . Time indices $m \in \{-3, \dots, 0\}$ indicate SRS channel coefficients from the preceding slot.

Given the above notation, we seek a prediction $\tilde{\mathbf{h}}_a = [\tilde{h}_{a1} \dots \tilde{h}_{aM}]^T$ of the actual channel vector \mathbf{h}_a , given the SRS channel coefficient estimates \hat{h}_{am} of the preceding slot. The metric to quantify the prediction quality is the relative MSE

$$\epsilon_M(\tilde{\mathbf{h}}_a, \mathbf{h}_a) = \frac{(\tilde{\mathbf{h}}_a - \mathbf{h}_a)^H (\tilde{\mathbf{h}}_a - \mathbf{h}_a)}{\mathbf{h}_a^H \mathbf{h}_a}, \quad (2.50)$$

which is dependent on the considered block length M .

To obtain the predicted channel vectors $\tilde{\mathbf{h}}_a$, we investigate four prediction methods which are detailed in the following. For other prediction methods developed in recent years, including Kalman-filter and machine learning (ML) approaches, the reader is referred to, e.g., [24]–[26].

Constant Prediction This method assumes a slowly varying channel with a coherence time $T^{(\text{coh})}$ much larger than the slot duration $T^{(\text{slot})}$, i.e., the CSI does not change significantly during one slot [3]. In this case, the last estimated channel coefficient \hat{h}_{a0} is considered a suitable prediction for the following channel coefficients, i.e.,

$$\tilde{h}_{am} = \hat{h}_{a0}. \quad (2.51)$$

In other words, no prediction is done, but the last known noisy uplink CSI is applied for downlink beam-forming. Only one uplink SRS channel coefficient is required with this method, so the overhead is minimized.

Linear Prediction This method applies a linear extrapolation using the last channel coefficients. The linear prediction is calculated by solving the linear set of equation

$\hat{h}_{am} = b_0 m + b_1$, $m \in \{-1, 0\}$ for b_0, b_1 and subsequent calculation of

$$\tilde{h}_{am} = b_0 m + b_1 = \hat{h}_{a0} + m \left(\hat{h}_{a0} - \hat{h}_{a,-1} \right) \quad (2.52)$$

for $m \geq 0$.

Polynomial Prediction A polynomial of third degree is fitted to the SRS channel coefficients and extrapolated to obtain the channel coefficients for $m > 0$. The polynomial prediction is calculated as

$$\tilde{h}_{am} = \sum_{k=-3}^0 \hat{h}_{ak} \Lambda_k(m) \quad (2.53)$$

with the Lagrange basis functions defined as

$$\Lambda_k(m) = \prod_{\substack{k'=-3, \\ k' \neq k}}^0 \frac{m - k'}{k - k'}. \quad (2.54)$$

The Lagrange polynomials can be precalculated and in our case read as

$$\Lambda_0(m) = \frac{1}{6}(m+1)(m+2)(m+3), \quad (2.55)$$

$$\Lambda_{-1}(m) = -\frac{1}{2}m(m+2)(m+3), \quad (2.56)$$

$$\Lambda_{-2}(m) = \frac{1}{2}m(m+1)(m+3), \quad (2.57)$$

$$\Lambda_{-3}(m) = -\frac{1}{6}m(m+1)(m+2). \quad (2.58)$$

Four SRS channel coefficients are required for the polynomial prediction of third degree.

Wiener Prediction Assuming that the fading process of the channel coefficients is described by Clarke's model, the autocorrelation of the channel coefficients in time, independent of the BS antenna a , is given by

$$\mathbf{r}_{h,m} = J_0 \left(2\pi f_D T^{(\text{symp})} |m| \right) \quad (2.59)$$

with $J_0(\cdot)$ being the zeroth-order Bessel function of the first kind and f_D the maximum Doppler shift.

Given that the uplink SRS channel coefficients are corrupted by noise according to (2.49), the Wiener predictor is written as [27]

$$\tilde{h}_{am} = \mathbf{r}_{h,m}^H \mathbf{R}_{\hat{h}}^{-1} \hat{\mathbf{h}}_a \quad (2.60)$$

with

$$\mathbf{R}_{\hat{h}} = \mathbf{R}_h + \sigma_n^2 \mathbf{I}_4, \quad (2.61)$$

$$(\mathbf{R}_h)_{m,m'} = r_{h,m-m'}, \quad (2.62)$$

$$\mathbf{r}_{h,m} = [r_{h,m} \ \dots \ r_{h,m-3}]^T, \quad (2.63)$$

$$\hat{\mathbf{h}}_a = [\hat{h}_{a0} \ \dots \ \hat{h}_{a,-3}]^T, \quad (2.64)$$

and known noise variance σ_n^2 .

First, we investigate the prediction algorithms outlined in Section 2.4.3 in terms of prediction quality, i.e., the relative MSE from (2.50), depending on the block length M in time, for a given maximum Doppler frequency f_D . The case of perfect CSI is also included for reference when appropriate. We analyze both synthetic data and data from vehicular measurements. In a second approach, we investigate the combination of OP and channel prediction in a link-level simulation using parameters similar to the 5G standard.

2.4.4 Prediction Quality Assessment

Simulations are done for a speed of 70 km/h at a carrier frequency of 3.5 GHz, resulting in a maximum Doppler frequency of 227 Hz. A correlated Rayleigh fading channel realization without additional noise according to [18] is assumed which exhibits a Clarke's Doppler power spectral density. The number of paths is 40 and no correlation across antennas is considered. The number of channel realizations of length M over which the relative MSE is calculated and averaged is 65000.

Figure 2.11 shows the relative MSE $\epsilon_M(\hat{\mathbf{h}}_a, \mathbf{h}_a)$ over the block length M . The Wiener predictor is superior to the other approaches as the autocorrelation process and the maximum Doppler shift f_D in (2.59) are known perfectly. The polynomial prediction performs reasonably well without any assumptions on the underlying channel statistics. The lines in Figure 2.11 marked with plus signs and circles show the relative MSE for the Wiener predictor with a correlation matrix obtained by decreasing or increasing the design Doppler frequency f_D in (2.59) by 25%. In this case, the prediction quality deteriorates and approaches the quality of the polynomial predictor.

Simulation models only reproduce the real world to a certain degree. Therefore, we use empirical data from vehicular measurements to analyze prediction quality in more realistic conditions. Given the high SNR of the measurements, we consider the gathered empirical data as perfect (i.e., noiseless) representation of the channel. The empirical channel coefficients \mathbf{h}_a were obtained in a line of sight (LOS) scenario with an UE mounted on a car with a velocity of approximately 60 km/h at a center frequency of 3.5 GHz. Details on the setup used to gather the empirical data are found in [10]. The repetition rate of the measurement was 1 ms and a DPS interpolation method with oversampling factor 14 as described in [19] is used to obtain channel realizations with a repetition time of $T^{(\text{symb})} = 71.43 \mu\text{s}$.

Figure 2.12 shows the relative MSE $\epsilon_M(\hat{\mathbf{h}}_a, \mathbf{h}_a)$ for the investigated prediction methods over block length M . Constant and linear prediction show similar prediction quality as with simulated data. The maximum Doppler frequency f_D for the Wiener predictor is derived from the position information obtained during the measurement and the autocorrelation process is not known perfectly. Therefore, the Wiener predictor shows degraded quality and approaches the performance of the polynomial approach.

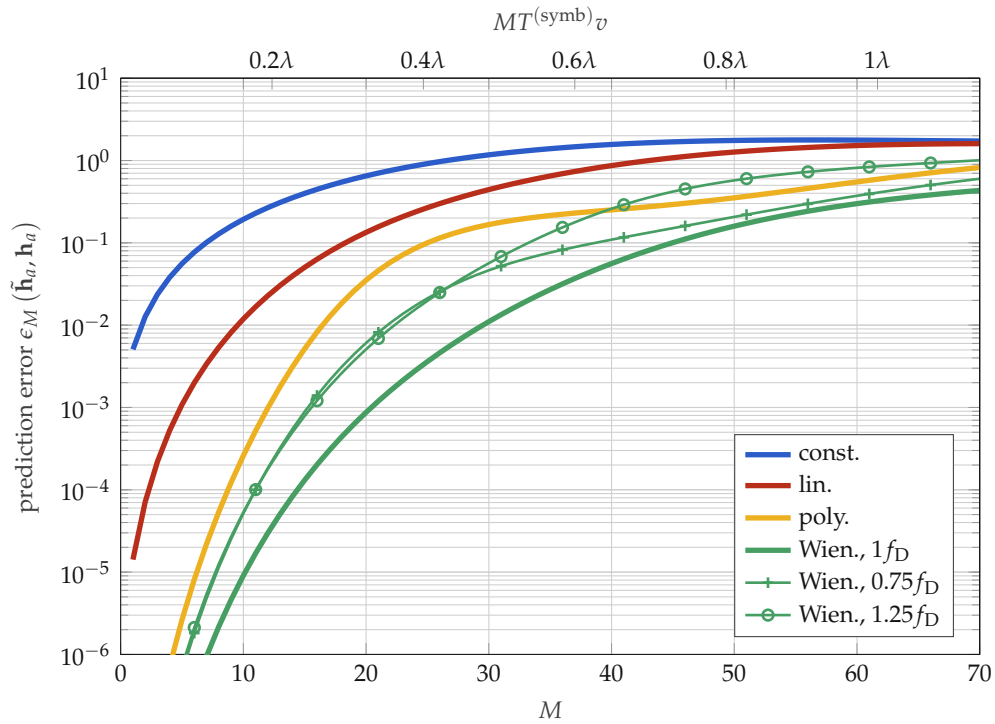


FIGURE 2.11: Relative MSE for block length M , a velocity of 70 km/h, and a carrier frequency of 3.5 GHz in a simulated Rayleigh channel. The Wiener predictor with perfect knowledge of the channel statistics exhibits the best prediction quality. For a mismatching maximum Doppler frequency f_D it approaches the quality of the polynomial prediction.

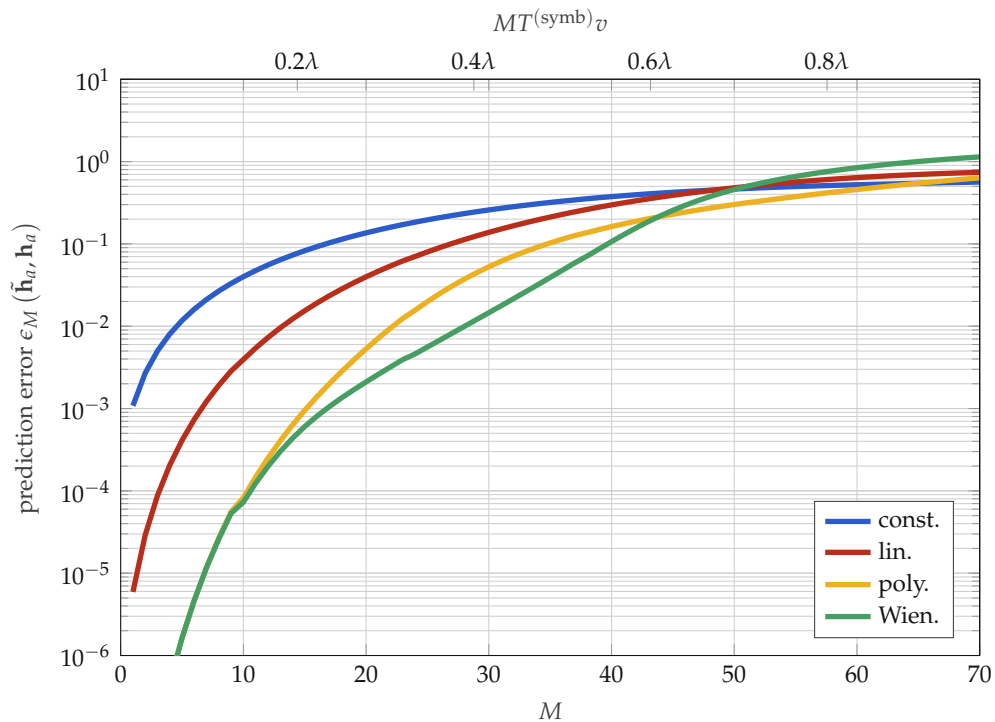


FIGURE 2.12: Relative MSE over the block length M in time for a velocity of 60 km/h at 3.5 GHz for empirical channel data from vehicular measurements.

2.4.5 Reliability Assessment

To assess the joint performance and trade-offs for massive MIMO beam-forming in space, OP in time-frequency and CSI prediction using the 5G slot structure, extensive link-level simulations are performed. Like before, a correlated Rayleigh fading channel model according to [18] is assumed with a Clarke's Doppler power spectral density. The number of paths is 40 and no correlation across antennas is considered. The maximum Doppler frequency $f_D = 520$ Hz unless noted otherwise, according to a velocity of 160 km/h at 3.5 GHz.

The physical layer is an OFDM system and we simulate $Q = 512$ subcarriers with a spacing of 15 kHz. Of all simulated subcarriers, 120 adjacent ones are considered for precoding, corresponding to 10 resource blocks with 12 subcarriers each. As before, the slot duration $T^{(\text{slot})} = 1$ ms and the symbol duration $T^{(\text{symbol})} = 71.43 \mu\text{s}$. Prediction and precoding are calculated for a block length of $M = 22$ in time. This block length is chosen such that, given 4 SRS symbols are transmitted in the uplink, one whole slot with 14 downlink symbols and one slot with 8 downlink symbols is predicted and simulated. The remaining 6 symbols of the second slot are reserved for guard and SRS symbols of the subsequent downlink phase and are therefore not considered (see also Fig. 2.10).

Perfect uplink channel information is considered, i.e., $\sigma_{\hat{h}}^2 = 0$ in (2.49). The downlink symbols consider an SNR as specified in the plots. An iterative receiver applying a BCJR decoder and soft-symbol feedback as described in [17] is used. The BS is considered to have $A = 64$ antennas and 500 frames are simulated per block length M .

Figure 2.13 shows a bar plot of the simulated BER for all considered prediction methods for four different velocities, three SNR values and no precoding over time and frequency employed, i.e., $\mathbf{s} = \mathbf{b}$ in (2.45). It is clearly observed that the BER increases for increasing velocities if constant CSI is assumed, and that the BER is only dependent on the SNR if CSI is perfectly known. Linear prediction offers decreased BER for low velocities, but performance quickly deteriorates for higher speeds. If the channel statistics are perfectly known, as is assumed here, Wiener prediction of the CSI significantly increases performance and is largely independent of the velocity as long as the prediction horizon is not larger than approximately 0.6λ .

Figure 2.14 plots the simulated BERs for the considered prediction methods, and compares no precoding to OP using DSFT. The assumed velocity is 160 km/h and channel statistics are known for the Wiener predictor. Precoding in combination with CSI prediction significantly increases performance. The penalty for imperfect channel prediction is roughly 1 dB for the Wiener filter with perfect channel statistic knowledge and roughly 2 dB for the polynomial predictor without any knowledge of the channel. In real-world scenarios, the performance of the Wiener prediction method will be closer to the polynomial one, as the channel statistics are hardly known perfectly and change over time.

It is seen from the dashed lines in Figure 2.14 that the deployment of polynomial prediction achieves BER performance gains over constant and linear prediction of > 4 dB (Wiener prediction: > 5 dB).

Figure 2.15 shows the dependence of the BER on the block length M for $A = 64$ BS antennas, a fixed velocity of 160 km/h and an SNR of $E_b/N_0 = 6$ dB using DSFT OP. We can observe that, for Wiener and polynomial prediction, the lowest BER is not achieved with the smallest prediction horizon $M = 8$ as would be expected without precoding, but with the increased block size $M = 14$. This effect arises due to the increased time-frequency diversity that is harvested by the OP method and

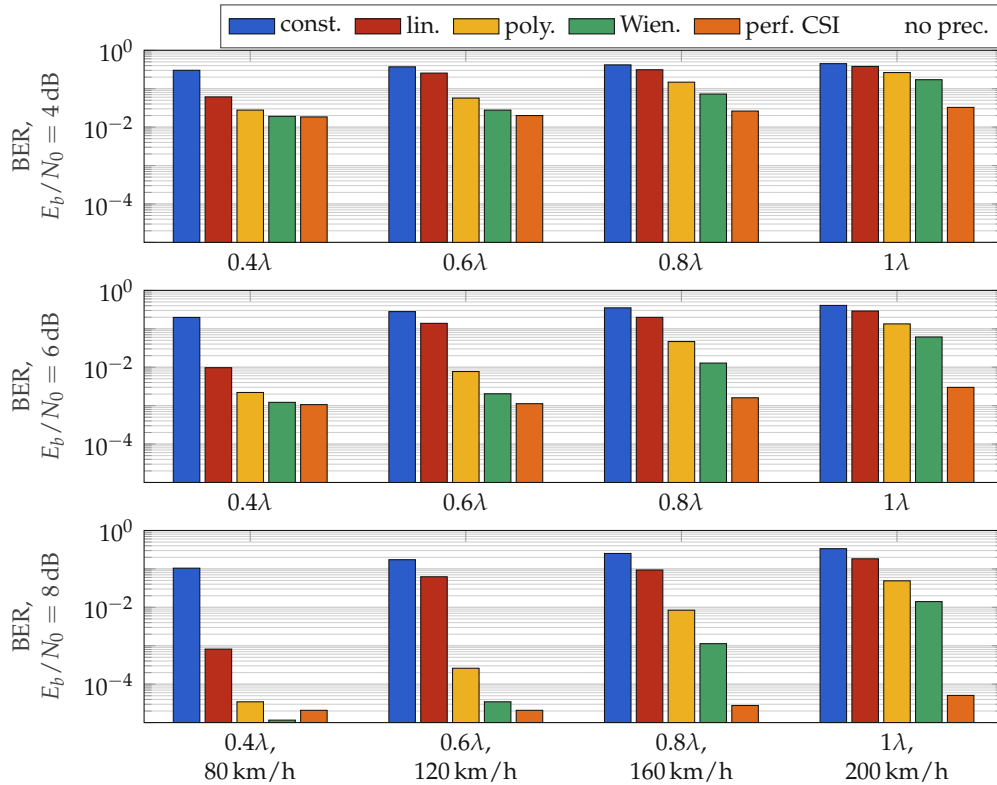


FIGURE 2.13: Bar plot of the simulated BER for a massive MIMO system employing CSI prediction without precoding, given various velocity and SNR combinations. The number of BS antennas is $A = 64$.

that successfully compensates for increased prediction errors towards the end of the slot. We conclude that for a given velocity and the corresponding spatial prediction horizon there exists an optimal block length M that entails the smallest prediction error and the largest diversity gain.

Figure 2.16 shows the dependence of the BER on the number of BS antennas A and the block length M in time for a fixed velocity of 160 km/h and an SNR of $E_b/N_0 = 6$ dB using OP. We can observe that the BER is mostly independent on A for $A > 16$ in our single user scenario. Moreover, the best performance is not achieved with the smallest prediction horizon $M = 8$ as would be expected without precoding, but with the increased block size $M = 16$. This effect arises due to the increased time-frequency diversity that is harvested by the OP method and that successfully compensates for increased prediction errors towards the end of the slot. We conclude that for a given velocity and the corresponding spatial prediction horizon there exists an optimal block length M that entails small prediction errors and large diversity gains.

2.5 Main Findings and Conclusion

We address the SE of time-variant massive MIMO using Wiener prediction. We derive asymptotic expressions of the achievable SE in an uplink massive MIMO system for an arbitrary prediction horizon $\ell \geq 1$, assuming a general temporal covariance matrix. Our results are also directly applicable to the downlink, due to uplink-downlink duality. Utilizing four instead of one pilot symbol is shown to

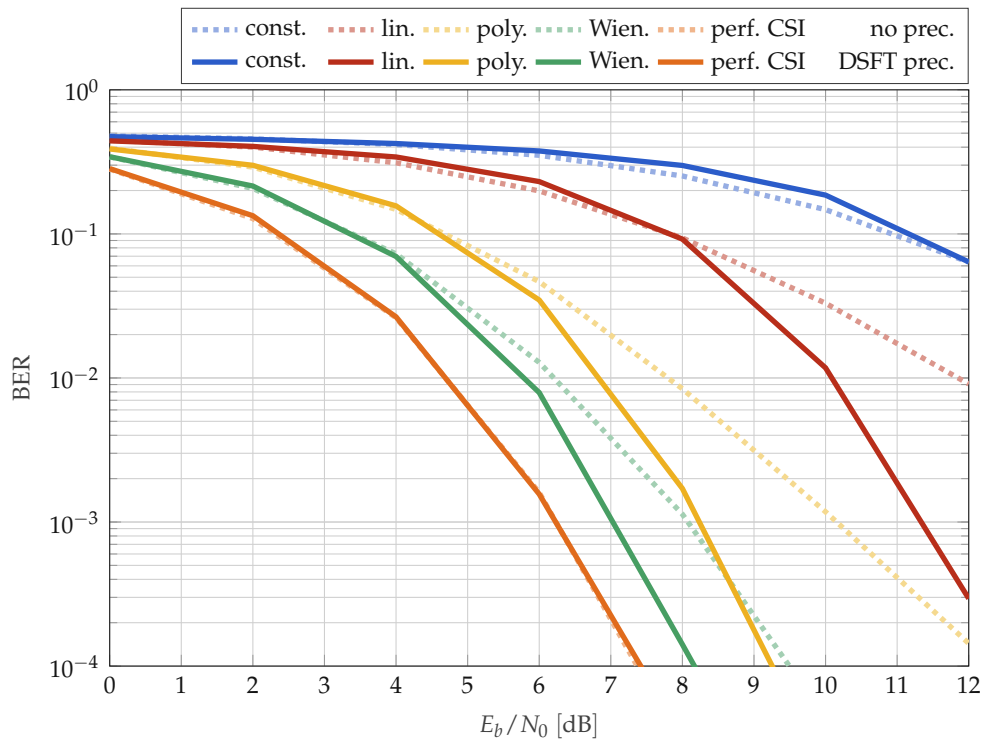


FIGURE 2.14: Simulated BER for a massive MIMO system employing the considered prediction methods without precoding and with DSFT precoding. The prediction horizon is 0.8λ at a velocity of 160 km/h and a frequency of 3.5 GHz, and the number of BS antennas $A = 64$. A significant performance gain is achieved through OP.

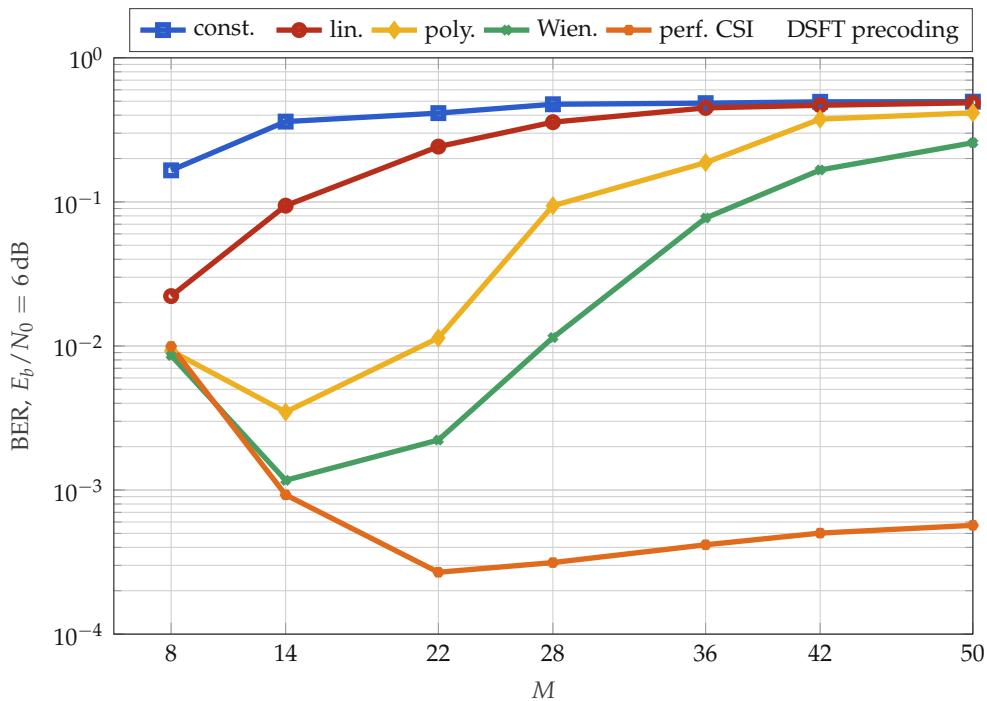


FIGURE 2.15: Simulated BER over block length M in time for $A = 64$ BS antennas, a velocity of 160 km/h and $E_b/N_0 = 6$ dB.

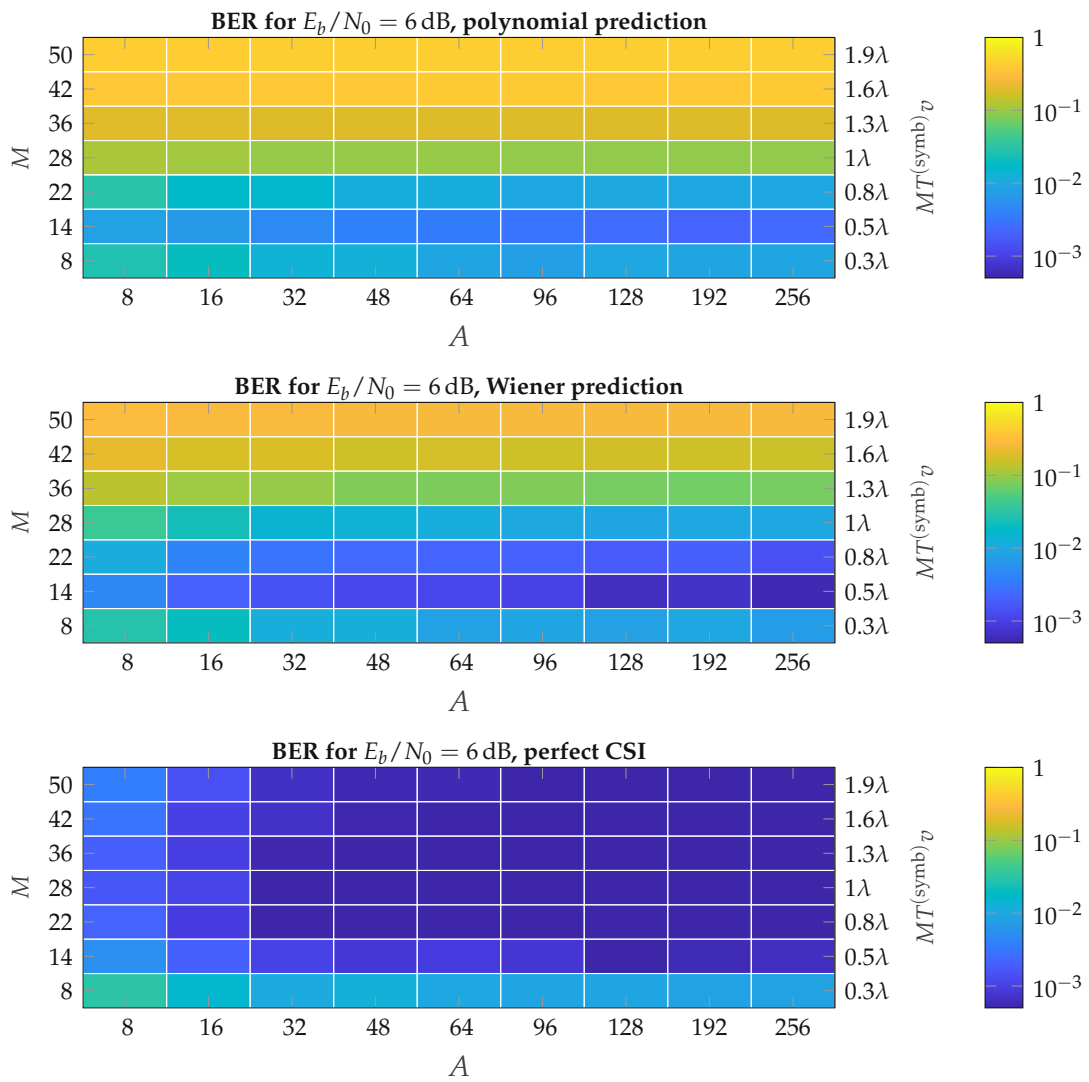


FIGURE 2.16: Simulated BER over block length M and number of BS antennas A for a velocity of 160 km/h.

double the SE, both for MRC and RZF. Utilizing more than four pilots shows no clear advantages.

Further, channel hardening, i.e., the capability of a massive MIMO system to eliminate small-scale fading and create quasi-deterministic effective channel gains, is shown to be (largely) independent of channel aging. These results allow to assess effects of channel aging due to mobility, and channel prediction as mitigation strategy, for arbitrary time delays.

We investigate the combination of OP and various CSI prediction methods in a massive MIMO single user downlink system. We show that the prediction quality of simple polynomial prediction is similar to the Wiener filter with empirical data from a vehicular measurement campaign. Link-level simulations show polynomial and Wiener CSI prediction significantly improves (> 5 dB) BER performance of our system in time-varying scenarios compared to constant or linear prediction. Additional utilization of OP further decreases the BER and enables approaching the performance of the system with perfect channel knowledge to within 2 dB (1 dB) for polynomial (Wiener) prediction for a velocity of 160 km/h. We show there is a trade-off between increased time-frequency diversity utilization and decreased predicted CSI quality for increasing block length in time.

2.6 Related Literature

There is vast literature on channel prediction for MIMO systems applying various methods. In [28], a Markov-model based approach with a Kalman-filter tracking the channel statistics is proposed. The authors in [24], [29] directly apply a Kalman-predictor. The work in [30] describes recurrent neural networks as well as special training methods for channel prediction and [31] investigates deep-learning prediction approaches. The authors in [6] investigate mitigation of channel aging via optimal Wiener channel prediction. However, none of the above explicitly investigates prediction quality given the constraints posed by the self-contained slot structure of the 5G standard [22].

Another strategy to mitigate fading is spreading information in time and frequency as initially introduced in [20], a method we refer to as OP. In [17] the authors investigate the reduction of fading (channel hardening) in a massive MIMO system by applying OP with either outdated or perfect channel knowledge and achieved a significant BER reduction in a high mobility scenario.

In [6], the effects of channel aging are thoroughly derived, but the utilized autoregressive temporal correlation model of order one (AR(1)) and the consideration of only one-step prediction limits the applicability of the results to band-limited real-world fading processes. In [14], the authors model achievable sum-rates of MIMO systems in the presence of channel aging and derive prediction strategies. However, again a simplified AR(1) model is utilized for the temporal correlation. A more suitable correlation is found in [32], where a Clarke's model is employed for modeling channel aging. However, no prediction algorithms are introduced or analyzed in [32]. Recent studies on high mobility massive MIMO utilize advanced prediction methods, such as Kalman filtering [24], [25] and ML [25], [26]. While providing state-of-the-art channel prediction quality, the work in [24]–[26] is not easily accessible to analytic and asymptotic considerations, especially concerning the variance of the achieved received signal power around its mean (which becomes negligible in case of channel hardening).

Chapter 3

Data Acquisition and Processing

3.1 Contents of this Chapter

To achieve **O3** of this thesis, that is, to gather empirical data to substantiate and support the theoretic and simulated results from Chapter 2, we devise in this chapter the hardware, software, and processing stack to enable fully parallel and coherent channel sounding in high mobility scenarios with widely distributed BS antennas (**M3**).

Section 3.2 details the hardware structure of the devised channel sounding framework, including the overall architecture, utilized antennas, synchronization methods, and calibration procedures. In Section 3.3, the necessary signal processing steps to analyze the gathered measurement data are devised. The contents of this chapter are published in

[10] D. Löschenbrand, M. Hofer, L. Bernadó, G. Humer, B. Schrenk, S. Zelenbaba, and T. Zemen, "Distributed massive MIMO channel measurements in urban vehicular scenario", in *13th European Conference on Antennas and Propagation (EuCAP)*, Krakow, Poland, 2019.

[11] D. Löschenbrand, M. Hofer, B. Rainer, and T. Zemen, "Empirical and simulated performance evaluation of distributed massive MIMO", in *Asilomar Conference on Signals, Systems, and Computers (ASILOMAR)*, 2019.

[9] D. Löschenbrand, M. Hofer, L. Bernadó; S. Zelenbaba, and T. Zemen, "Towards cell-free massive MIMO: A measurement-based analysis", *IEEE Access*, 2022. DOI: 10.1109/ACCESS.2022.3200365.

Based on this chapter, measurement campaigns are carried out and the respective data is analyzed in Chapter 4.

3.2 Massive MIMO Channel Sounding Framework

We aim at measuring time variant impulse responses of a wireless communication channel, a process commonly referred to as *channel sounding*, in accordance with **O3** of this thesis: to gather empirical data that substantiates the results from Chapter 2. In this section, we present in detail the massive MIMO channel sounding framework, its general architecture and important components utilized to achieve this objective. Special emphasis is put on the measures taken to enable continuous mobile measurements at velocities up to 150 km/h with 115 MHz of bandwidth.

3.2.1 Channel Sounder Architecture

To measure the time variant impulse responses of the wireless communication channel, we use a transmitter (TX) that transmits a known sounding sequence. After

propagating through the surrounding environment, the receiver (RX) receives the sounding sequence convolved with the impulse response of the wireless channel, performs an analog to digital (A/D) conversion and saves the signal to a hard drive. In post processing, the impulse response is obtained. In what follows, we describe the TX and RX hardware components and structure required for the task. The sounding sequence design and the post-processing methods necessary to calculate the impulse response are detailed in Section 3.3.

TX Components and Structure The transmitter node of the presented massive MIMO channel sounder consists of a software-defined radio (SDR) with a frequency range of 10 MHz – 6 GHz (universal software radio peripheral (USRP) 2954R). The USRP feeds two transmit antennas TX 1 and TX 2 with two sounding sequences that are multiplexed in time to avoid interference with each other. External power amplifiers (PAs) are used to increase the transmit power. The USRP is controlled and configured by a host computer which is connected via a PCI extensions for instrumentation (PXI) interface. This data interface allows for the transfer of I/Q samples to and from the USRP with a maximum rate of 800 MB/s. Synchronization and triggering is performed via a Rubidium clock and further detailed in Section 3.2.4. Figure 3.1 shows the block diagram of the TX with two transmit antennas TX 1 and TX 2.

The setup is powered by an uninterruptible power supply (UPS) which allows for more than four hours of measurement time without the need of a power outlet. The TX is placed in a small van and TX antennas as well as global navigation satellite system (GNSS) antennas for position tracking are mounted on the roof of the van. The transmitter node is thus mobile and can be operated at various speeds and in different propagation scenarios.

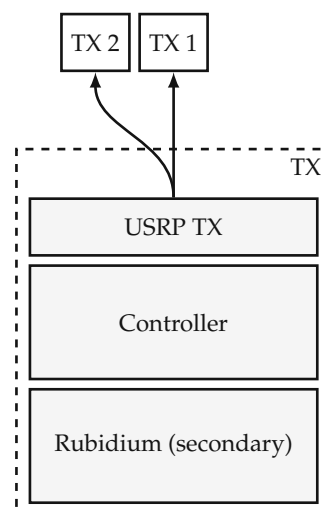


FIGURE 3.1: Block diagram of the massive MIMO channel sounder TX. The transmitter consists of one USRP connected to two antennas (TX 1, TX 2) and supplemented with external PAs. Synchronization is provided by Rubidium clocks at TX and RX, respectively.

RX Components and Structure The RX features 16 SDRs with 32 RF chains in total, which are operated fully parallel at their maximum bandwidth. We group the RF chains into two distributed units (DUs), each of which features 16 RF chains. Both DUs are connected to a host computer in the baseband processing unit (BPU) via 30 m

data and synchronization cables. This allows for a maximum distance between the DUs of up to 60 m. The 16 deployed SDRs are USRPs 2953R models with a frequency range of 1.2 – 6 GHz. Like the TX, the RX uses a Rubidium clock for synchronization and triggering. Additionally, a designated clock distribution network splits and amplifies the reference and trigger signals from the RX Rubidium oscillator at each DU and forwards it to each individual USRP. Data from the USRPs is passed to a data accumulation unit, which in turn forwards the accumulated data over a fiber optic connection to the controller in the BPU. Fig. 3.2 shows a block diagram of the sounder structure.

To achieve even larger apertures, coaxial cables with a length of 15 m are used to connect each DU with 16 RX patch antenna array elements, see Fig. 3.2 at the top. With this method, array apertures of up to 90 m with 32 array elements are possible, all while maintaining fully parallel coherent reception and fast channel sounding capabilities. To compensate for the losses of the long coaxial cables, power amplifiers with a 1 dB compression point of 39 dBm are used at the TX side.

3.2.2 Transmit and Receive Antennas

Throughout this thesis, we consider carrier frequencies of 3.2 GHz and 3.5 GHz, which lie in a frequency band specifically allocated for 5G in most of the world. To take full advantage of the 120 MHz instantaneous bandwidth of the USRP hardware, the TX and RX antennas must provide a similar or higher bandwidth at the considered carrier frequency.

Depending on the requirements of a measurement campaign, various antenna types can be used with the channel sounding framework described in Section 3.2.1. In particular, measurement bandwidth, interference from nearby cell towers, necessary gain, and aperture determine the right choice of TX and RX antennas. In the following, the antennas that were specifically designed and built to enable the measurement campaigns in this thesis will be described in detail.

TX Antennas Vertical monopole antennas over a finite horizontal ground plane are used on both TX 1 and TX 2. They provide an omni-directional radiation pattern in the upper half-sphere and transmit vertically polarized signals. The 10 dB bandwidth is 600 MHz, centered at a carrier frequency of 3.5 GHz. The monopole antennas are fastened to a magnetic mount to be easily deployable on the vans roof, and are connected to the TX with coaxial cables.

Rectangular RX Patch Antenna Array Air-gaped patch antenna arrays are designed to be used on both DU 1 and DU 2. One array element consists of a single quadratic metallic patch with dimensions 3.05×3.05 cm on a standard 1.52 mm FR4 substrate. One RX DU array consists of 16 patch elements (two rows of eight elements on top of each other) mounted on an aluminum plate that serves as ground plane and adds mechanical stability, see Fig. 3.3b. An air-gap of 3 mm is introduced between substrate and ground plane to extend the bandwidth of each patch element, see Fig. 3.3a. Each patch element is connected to two antenna ports for horizontal and vertical polarization. The patch element spacing is 6 cm ($\approx 0.7\lambda$ at 3.5 GHz) in both horizontal and vertical direction. The total size of one RX array is 48 cm by 12 cm.

The array exhibits a 10 dB bandwidth of 450 MHz centered at a frequency of 3.6 GHz. The S_{11} parameter, measured for both an element in the center of the array as well as on the edge, is shown in Fig. 3.4.

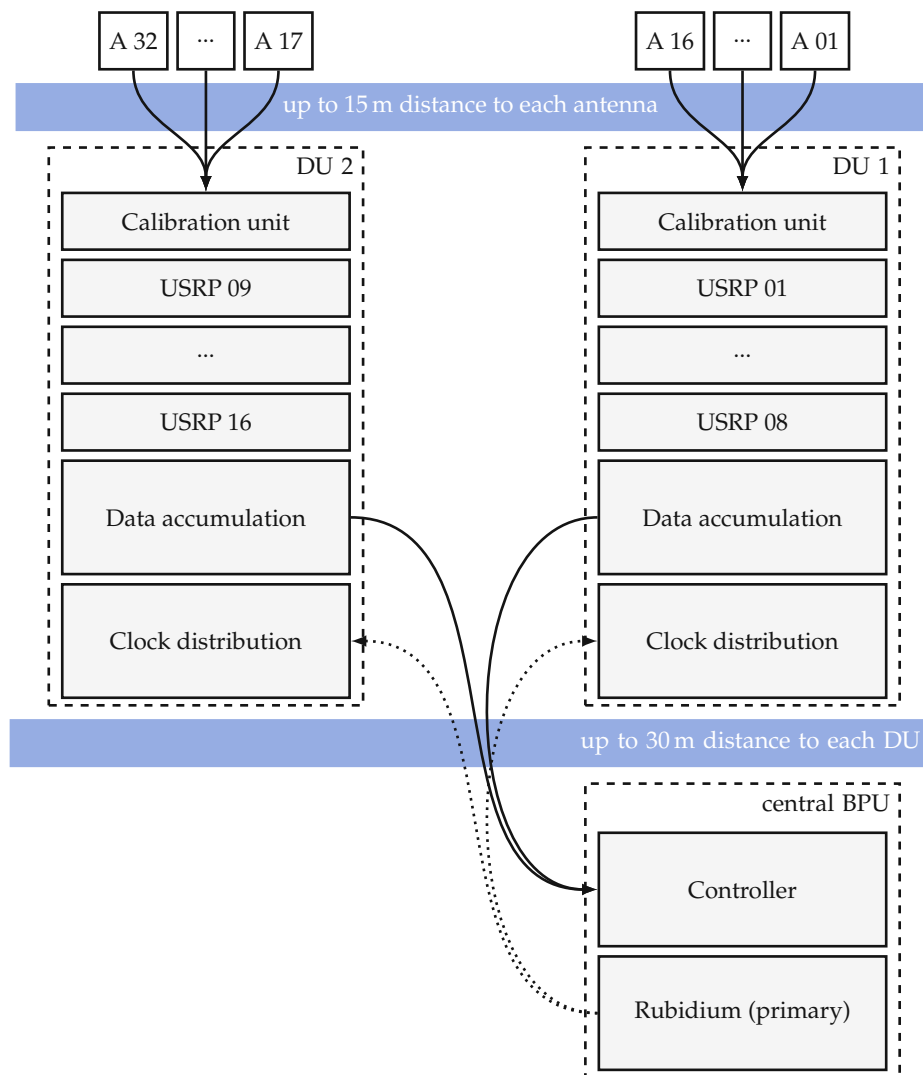
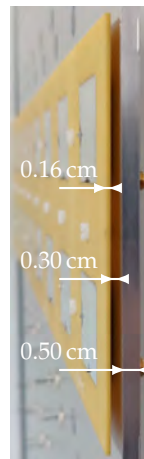
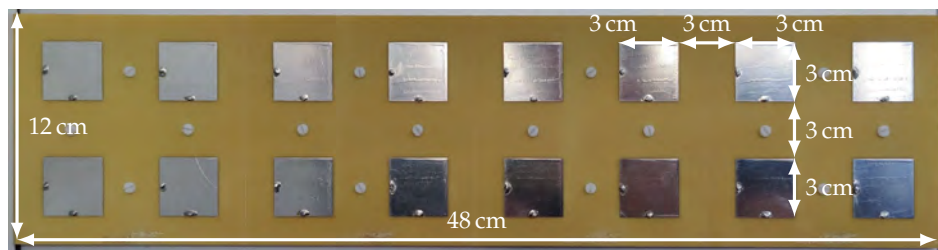


FIGURE 3.2: Block diagram of the massive MIMO channel sounder RX. The RX is divided into a BPU and two DUs which can be placed arbitrarily in space with a maximum distance of 60 m to each other. Each DU is connected to 16 antennas (DU 1: A 01 - A 16, DU 2: A 17 - A 32). The massive MIMO calibration unit is placed between the RX antennas and USRPs in order to facilitate calibration.

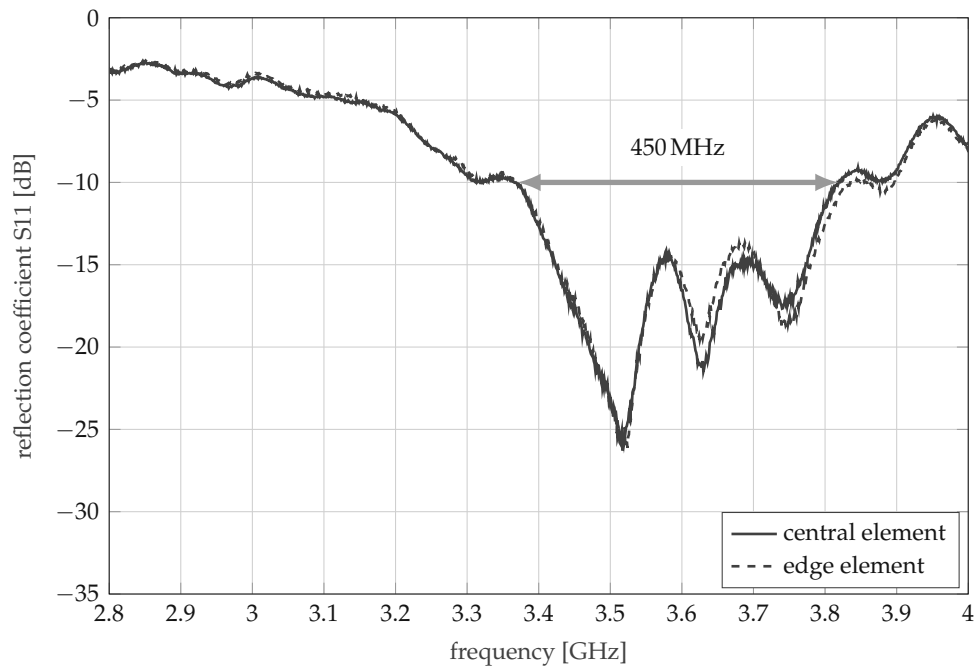


(a) Side view of the RX air-gaped patch antenna array with dimensions.



(b) Front view of the RX air-gaped patch antenna array with dimensions.

FIGURE 3.3: Side view and front view of the rectangular RX air-gaped patch antenna array. Two of these arrays are utilized, one for each DU.

FIGURE 3.4: S_{11} parameter for both an RX antenna element in the center of the array as well as on the edge. The array exhibits a 10 dB bandwidth of 450 MHz centered at a frequency of 3.6 GHz.

Modular Wide Aperture RX Patch Antenna Array In Chapter 2, it is shown that massive MIMO requires nearly orthogonal channel vectors $\mathbf{h}_{km}^H \mathbf{h}_{k'm} \approx 0$ for linear beam-forming techniques like MRC to be close to optimal. This is achieved primarily by deploying a large number of BS antenna elements and capitalizing on the law of large numbers. However, an imperative prerequisite is uncorrelated entries in the channel vector, which can be achieved by harnessing spatial diversity through distribution of BS antenna array elements over a wide aperture in space. This approach gained traction again recently under the terms *wide aperture arrays* and *cell-free massive MIMO* [33].

To enable channel sounding campaigns with RX antennas distributed over a wide aperture, a modular setup of the individual array elements is pursued. Each RX antenna is designed to either being deployed individually or grouped together to form an array. Moreover, each RX antenna offers a 1/4-inch thread that can easily be fastened to photography equipment like tripods or magnetic mounts. We choose a ball head mount for leveling and orientation correction of the RX antenna array element and a magnetic mount, see Fig. 3.5a.

One individual RX antenna consists of a patch element over a finite ground plane. Like in the rectangular RX antenna array described above, an air-gap is introduced between ground plane and patch element to increase its bandwidth. The patch is 3.5 cm by 3.5 cm, centered on a ground plane of dimensions 6 cm by 6 cm. The dielectric which carries the metallic patch element is standard FR4 and 0.5 mm thick, and the air-gap is 3 mm wide, see Figs. 3.5b and 3.5c. Each patch is vertically polarized but can be rotated using the ball head tripod by 90 degree to achieve horizontal polarization.

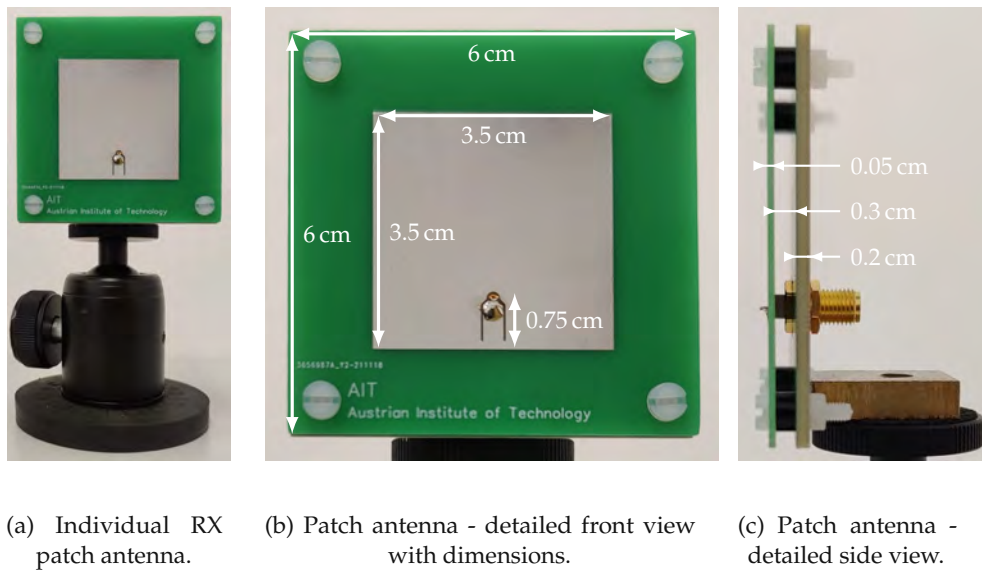


FIGURE 3.5: Modular patch antenna array element on ball head tripod with magnetic mount and dimensions.

With the antenna design described above, we achieve a 10 dB bandwidth of 180 MHz at a center frequency of 3.15 GHz. The S11 parameter, measured both with and without adjacent antennas, is shown in Fig. 3.6.

Modular Wide Aperture RX Antenna Array Configurations Numerous antenna array geometries can be realized with minimal effort utilizing the modular RX antenna array setup as described above. We implement three different horizontal linear arrays

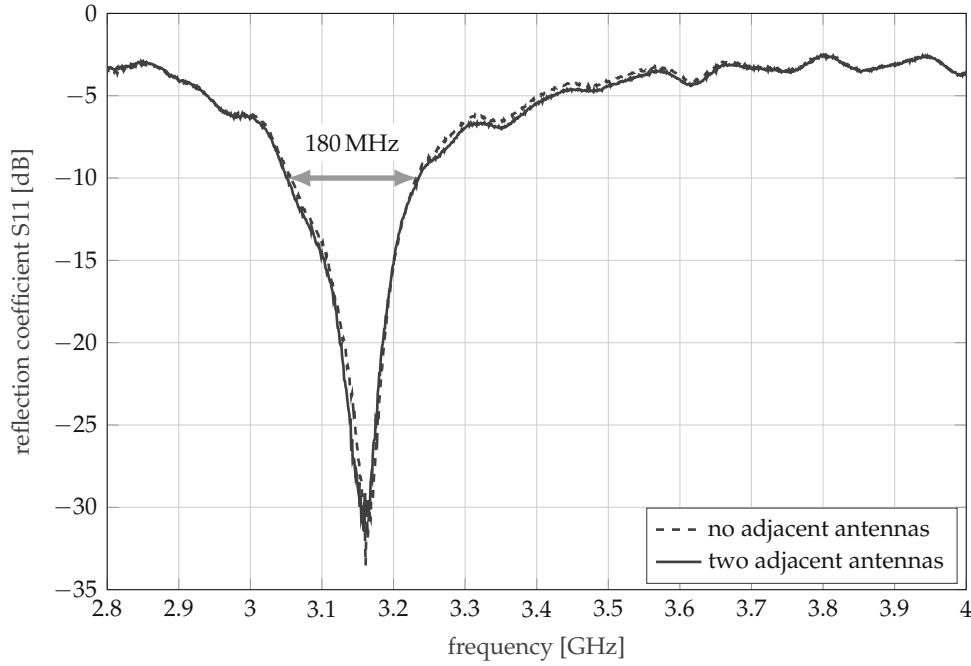


FIGURE 3.6: S_{11} parameter for an individual RX antenna array element, both with and without adjacent antennas. The 10 dB bandwidth is 180 MHz at a center frequency of 3.15 GHz.

with varying aperture size and element spacing. Detailed array dimensions are provided in Fig. 3.7.

RX array configuration 1 (RX conf. 1) resembles a conventional linear massive MIMO array with 32 antenna elements aligned horizontally and spaced 0.64λ with λ being the wavelength at the sounding frequency of $f = 3.2$ GHz. With this array configuration, grating lobes are mostly avoided and the TX operates in the far-field [3, Sec. 4] of the RX array, i.e., the distance d_k between user k and RX array satisfies

$$d_k \geq \frac{2D^2}{\lambda}, \quad (3.1)$$

with D being the size of the linear RX array. Therefore, all 32 RX antennas operate in an almost identical propagation environment and exhibit strong similarities in path-loss, blocking by large objects, visibility of main scatter sources, and relative TX velocity.

RX array configuration 2 (RX conf. 2) resembles a distributed massive MIMO array with two antenna arrays of 16 elements. The two arrays are distributed with a distance of 44.6 m between them. Each of the distributed arrays is again assembled with horizontally aligned and 0.64λ -spaced antenna elements. With this distributed array configuration and a total aperture size of 46.5 m, the TX never operates in the far-field of the RX array according to (3.1). This implies that wavefronts impinging at the RX array are spherical in general and not of equal amplitude. The elements of a distributed 16-element array operate in an almost identical propagation environment. But propagation characteristics like path-loss, shadowing, and Doppler due to the relative TX velocity can differ substantially from one distributed array to the other.

RX array configuration 3 (RX conf. 3) resembles a cell-free massive MIMO setup with 32 antenna elements horizontally aligned but spaced with a distance of 16λ from

one array element to the next. This configuration can be considered as implementation of the radio stripe architecture proposed in [34]. Since receiving elements are uniformly distributed over a large aperture of 46.5 m, they exhibit strong variations of propagation characteristics such as path-loss, shadowing, and Doppler due to the relative TX velocity.

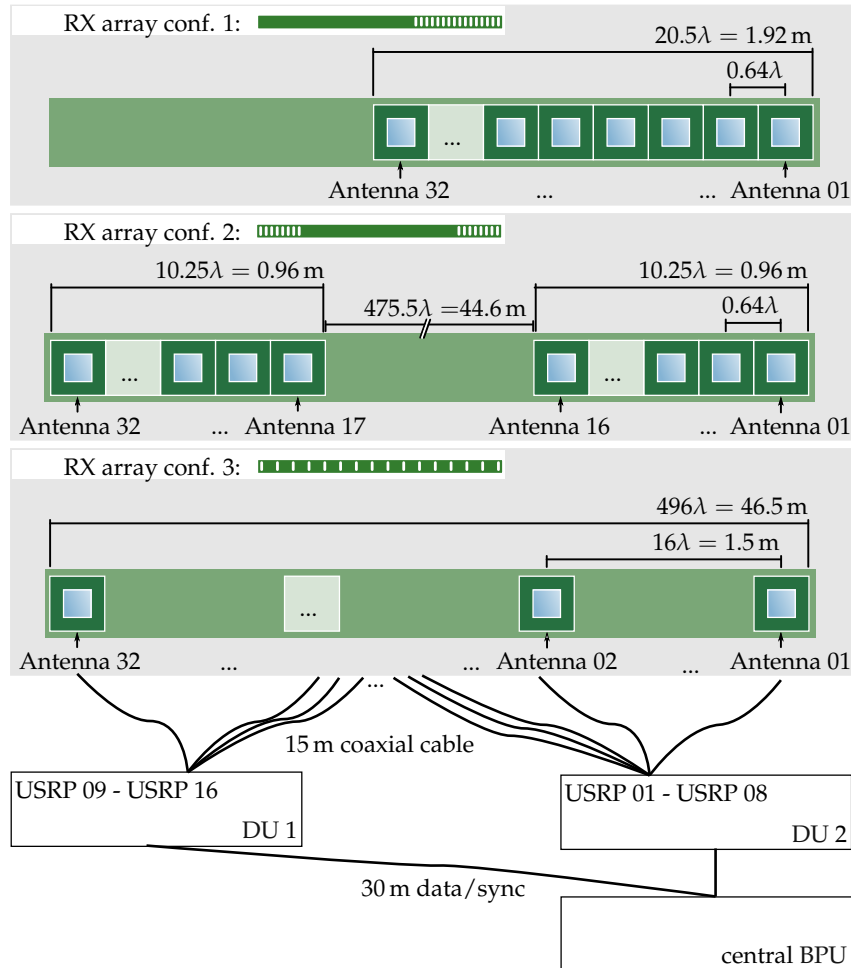
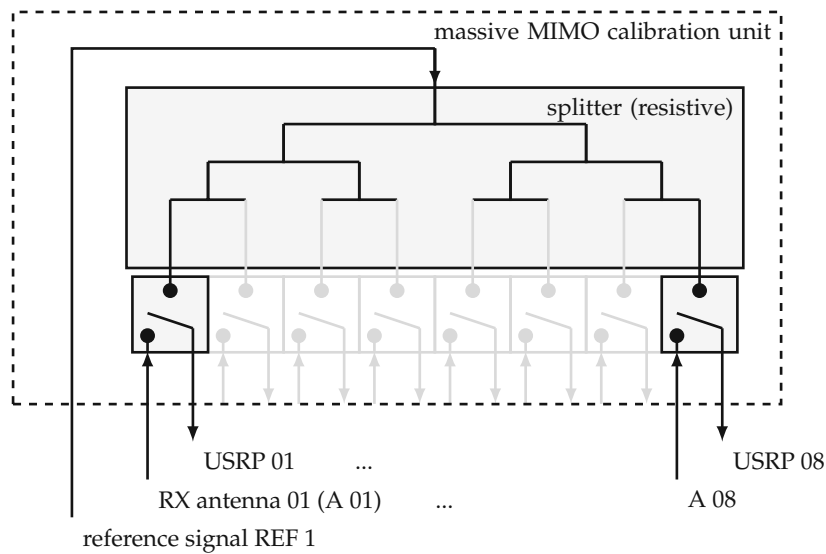


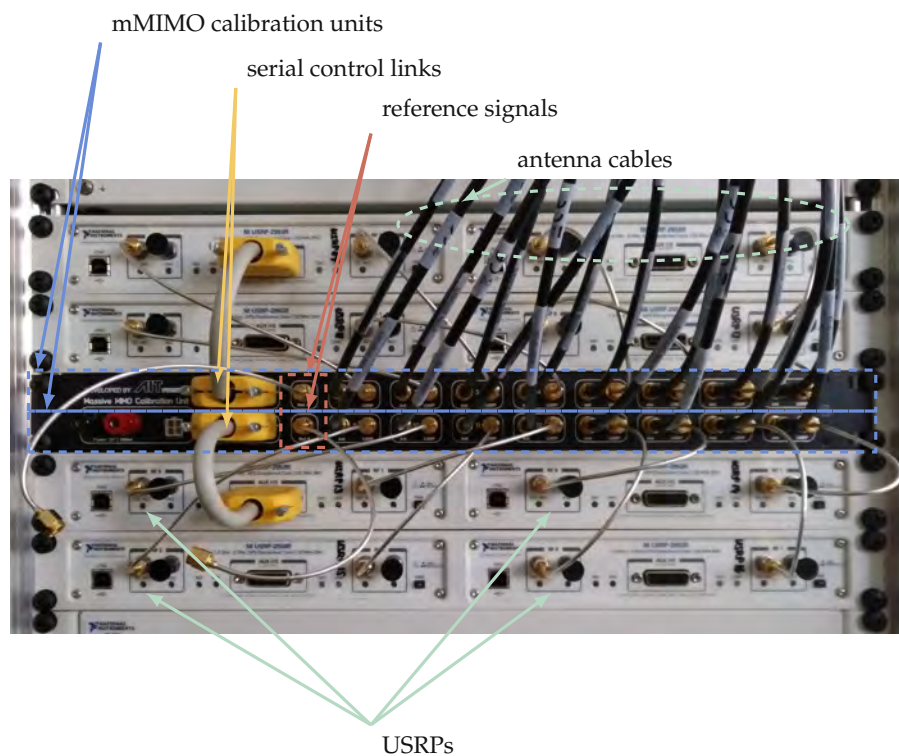
FIGURE 3.7: Channel measurement framework consisting of a central BPU for data aggregation and storage (bottom), two DUs for up- and down conversion, and 32 antennas assembled in one of three RX array configurations (top).

3.2.3 Massive MIMO Calibration Unit

A custom built massive MIMO calibration unit (see Fig. 3.8) is integrated in the measurement framework. It provides one input port for a reference signal, eight antenna input ports and eight RF output ports. A resistive 8-way power splitter divides the reference signal and routes it to eight individually controllable switches. These externally controlled switches allow to choose if either the signals from the eight antennas or the split reference signals are further routed to the RF output ports, see Fig. 3.8a. Figure 3.8b shows two massive MIMO calibration units in one housing, connected to 16 RF ports of eight USRPs and to 16 RX antennas. The control signals are provided via a serial interface of two USRPs.



(a) Massive MIMO calibration unit schematic.



(b) Assembly with two massive MIMO calibration units in one housing, four USRPs on top and four USRPs below.

FIGURE 3.8: Schematic and fully assembled view of the massive MIMO calibration unit. Externally controlled switches route either a reference signal or the antenna signal to the RF output ports which are in turn connected to the receiver USRPs. Two units, as depicted on top, are assembled into one housing and connected to 16 RF chains as seen at the bottom.

In the measurement setup, the calibration unit ensures fast and reliable calibration of all RF chains in the system by routing one reference signal to all RF chains. Thereby, obtaining the frequency response of the involved converters and amplifiers is significantly facilitated. The calibration procedure is the following:

1. Connect transmitter TX 1 (with appropriate attenuation) to the reference input port REF 1.
2. Control the calibration unit such that the reference signal from REF 1 is routed to USRP 01 - USRP 04.
3. Record time samples and store for offline calibration.
4. Perform steps 1) - 3) for all relevant combinations of TX 1, TX 2, REF 1 - REF 4, and USRP 01 - USRP 16.

Provided that the frequency response of the calibration unit is known and does not change, this procedure allows fast and reliable calibration of massive MIMO systems in the field.

3.2.4 Synchronization

In general, RX and TX of any channel sounding hardware need accurate time and frequency synchronization to acquire meaningful measurement data. Synchronization methods are manifold, reaching from dedicated synchronization signals to signal detection and manipulation in post processing. As discussed in the previous chapters, we are primarily concerned with massive MIMO in *time variant* scenarios. Consequently, synchronization during measurements must be achieved with mobility of parts of the hardware in mind. In what follows, the time and frequency synchronization method between the static RX and a mobile TX as well as synchronization from the RX BPU to all USRPs is introduced.

RX-TX Synchronization A Precision Test Systems GPS10eR Rubidium clock is used at the RX to provide a 10 MHz reference signal and a 1 pulse per second (PPS) trigger signal for timing. This Rubidium clock is used as the primary clock and operated in free-run mode. An identical, secondary Rubidium clock is used to provide reference and trigger signals on the TX side. The secondary TX clock is connected via coaxial cables and disciplined to the primary RX clock. This process takes approximately two hours, after which the two Rubidium clocks are sufficiently synchronized, configured to operate in free-run mode, and separated. During the synchronization procedure, calibration measurements are done to acquire the RF transfer functions of all hardware components involved, as discussed in Section 3.2.3. Due to the low frequency drift of the Rubidium oscillator, the separated clocks are used for synchronizing RX and TX for approximately four hours, depending on the outside temperature and other environmental perturbances.

RX-internal Synchronization Two different methods are implemented to synchronize the DUs with the BPU in the RX.

- Coaxial cables: Standard coaxial cables of 30 m length carry the reference and 1 PPS trigger signal from the Rubidium oscillator at the BPU to each DU. This allows for a distance between fully synchronized DUs of up to ≈ 60 m.

- Synchronization over fiber: The open hardware platform White Rabbit (WR) provides precision time protocol synchronization combined with clock phase adjustments over fiber to achieve sub-nanosecond accuracy over large distances. A validation of said system in the massive MIMO context was investigated in [35] and found suitable for our channel sounder architecture. The advantage of synchronization over fiber is its applicability to long distances between receiver nodes and its robustness against environmental stress factors like strong temperature gradients.

For the measurements campaigns presented in this thesis, the first synchronization method is used. However, an implementation of the second method is available and scope of future investigations involving even wider distributed RX antenna configurations.

3.3 Channel Acquisition and Analysis

In this section, we will first introduce the processing steps required to obtain time-variant impulse responses of the wireless communication channel with the channel sounding framework described in Section 3.2. Subsequently, we define the evaluation methodology for assessing the fundamental characteristics of massive MIMO systems with different RX array configurations and apertures in time-variant scenarios. In Chapter 4, the results of the evaluation methodology developed here are presented.

3.3.1 Channel Sounding Signal Model

With the channel sounding framework described in Section 3.2, we obtain bandlimited estimates of the wireless channel transfer function by transmitting a known sounding sequence from $K = 2$ users $k \in \{1, 2\}$, receiving it at the $A = 32$ RX antennas simultaneously and storing the sampled time signal on a hard-drive. In post-processing, this stored time signals are Fourier-transformed and calibrated to correct for the effects of the RF chain. The obtained time-dependent realizations of the channel matrix are then used to derive and analyze the channel characteristics.

We use a complex baseband multitone signal, defined as

$$x[n] = x(nT/Q) = \sum_{q=-(Q-1)/2}^{(Q-1)/2} s[q] e^{i2\pi qn/Q}, \quad (3.2)$$

to capture the channel characteristic over time. The time signal $x[n]$ is formed by a superposition of Q tones with complex weights $s[q]$ and frequency spacing Δf . The amplitudes of the complex weights $|s[q]| = 1$ are chosen to be equal. Their phases are optimized to achieve a low peak-to-average power ratio (PAPR) (square of the *crest factor*) [3, Ch. 8, Eq. (8.3)]

$$\text{PAPR} = \frac{\max_{t \in [0, T]} |x(t)|^2}{\frac{1}{N} \int_0^T |x(t)|^2 dt} \quad (3.3)$$

of the continuous signal $x(t)$ over the period $T = 1/\Delta f$ with the algorithm proposed in [36].

The multitone signal $x[n]$ utilized throughout this thesis features a frequency spacing of $\Delta f = 240$ kHz and $Q = 481$ tones, thus yielding a bandwidth of $B = 115.44$ MHz, with $\text{PAPR} = 1.54$. Like in an OFDM system, we concatenate the

multitone signal with a copy of itself which acts as cyclic prefix (CP). Additionally, a third copy is added to increase the SNR. Thus, the final sounding signal consists of three concatenated copies of the multitone signal $x[n]$ and therefore lasts $3T = 12.5 \mu\text{s}$. Each user k transmits the same sounding sequence with a $(k - 1)3T$ time shift to not interfere with the current measurement.

The sounding signal is sent and received with a repetition rate of $T^{(\text{rep})} = 1 \text{ ms}$, which results in a maximum resolvable Doppler frequency of 500 Hz and a maximum resolvable TX velocity of 150 km/h at a sounding frequency of $f_c = 3.2 \text{ GHz}$.

Each individual antenna $a \in \{1, 2, \dots, A\}$ receives the sounding signal $\tilde{y}_{ka}[m, n]$, which is transmitted by TX k and convolved with the communication channel $h_{ka}[m, q]$. Since the sounding procedure works like a CP OFDM scheme, the received multitone signal weights are obtained by omitting the CP and guard periods in $\tilde{y}_{ka}[m, n]$ to obtain $y_{ka}[m, n]$ and performing a subsequent discrete Fourier transformation, i.e.,

$$\tilde{Y}_{ka}[m, \tilde{q}] = \frac{1}{\sqrt{2Q}} \sum_{n=0}^{2Q-1} y_{ka}[m, n] \exp^{-\frac{j2\pi n\tilde{q}}{2Q}}, \quad (3.4)$$

where n denotes discrete time and q discrete frequency.

The signal part of the sounding sequence contains two repetitions of the multitone signal (3.2). Therefore, every second frequency bin $Y_{ka}[m, q] = \tilde{Y}_{ka}[m, 2\tilde{q}]$ constitutes the uncalibrated transfer function of the communication channel and the radio front-ends. We consider the transmitted symbols $s[q]$ in the frequency domain as pilot symbols which are known at the receiver. Thus, we calculate the calibrated transfer function estimate of the channel by a least squares (LS) estimation [37], [38, Sec. 1.7] as

$$\hat{h}_{ka}[m, q] = \frac{Y_{ka}[m, q]}{s[q] \hat{h}_{ka}^{\text{RF}}[q]}. \quad (3.5)$$

The channel frequency response (CFR) $\hat{h}_{ka}^{\text{RF}}[q]$, representing the transmit and receive RF chain properties, is obtained during a calibration phase prior to the measurement [10].

Figure 3.9 shows the processing steps involved in acquiring the samples to calculate the time-variant transfer function $\hat{h}_{ka}[m, q]$ from user k to RX antenna a .

The finite bandwidth channel impulse response (CIR) is calculated via the inverse Fourier transform over the bandwidth $B = Q\Delta f$

$$\hat{g}_{ka}[m, n] = \frac{1}{Q} \sum_{q=0}^{Q-1} \hat{h}_{ka}[m, q] e^{j2\pi nq/Q}, \quad (3.6)$$

with n being the delay index.

3.3.2 Ray Tracing Implementation

To analyze sounding scenarios in more detail without the need for new measurements, we derive a detailed and spatially consistent ray tracing (RT) model. This allows us to evaluate varying array geometries in different environments and compare them to measurement data. We implement the AIT RT using the NVIDIA Optix RT engine [39]. We follow a hybrid approach, where in a first step possible reflection, diffraction, and diffuse scattering points on surfaces are identified without rigorous validity checks with the 3D geometric model depicted in Fig. 3.10. For this purpose, a reflection tree of given depth is built via the image method. In the second step, we launch rays towards

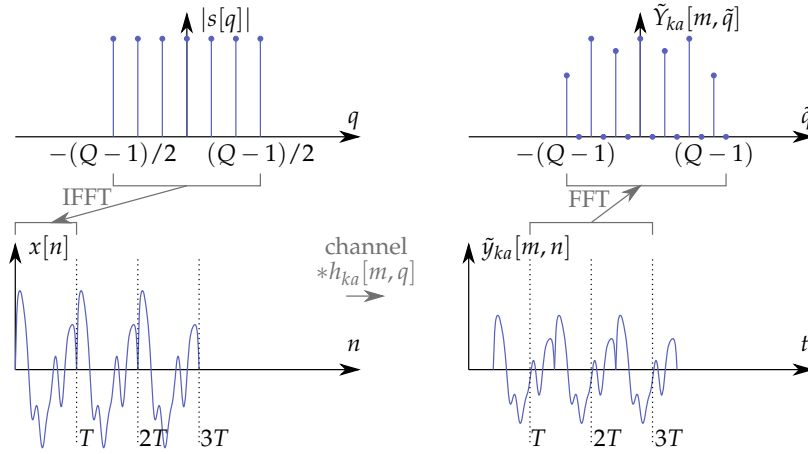


FIGURE 3.9: Signal processing chain of the channel sounder. The complex tone weights $s[q]$ are transformed into time domain via inverse fast Fourier transform (IFFT). The resulting time signal $x[n]$ is concatenated four times and transmitted over the radio channel. At the receiver, the whole sounding sequence is stored. A part of length $2T$ is used to obtain an oversampled estimate of the communication channel via an FFT.

the identified points in space using the NVIDIA Optix framework. The following mechanisms for identifying reflection, diffraction, and diffuse scattering points and computing their respective electromagnetic field are supported and implemented:

- Specular reflections of ℓ -th order by the image method (Snell's law).
- Edge diffraction according to the uniform theory of diffraction (UTD) [40].
- Points on surfaces for diffuse tiling according to [41], [42] and a novel tiling method based on lattices including the Lambertian and directive scattering model [43].

In this thesis, we use the directive scattering model and lattice-based¹ tiling in order to obtain a correlated Doppler spectral density [39]. The basis for the tiling of surfaces is select as

$$\mathbf{b}_i = \frac{\mathbf{u}_i}{\|\mathbf{u}_i\|_2} \frac{c}{2B}, \quad i \in \{1, 2\} \quad (3.7)$$

where \mathbf{u}_i is the i -th spanning vector of a surface, B the system bandwidth (in this thesis 115.44 MHz) and c denotes the speed of light. This leads to the fact that each first order diffuse scattering ray falls into a different delay bin. We implement higher order diffuse scattering by tracing the specular reflection of each diffuse scattering point.

To the best of the authors knowledge, this is the first implementation capable of reproducing measured Doppler spectra over time with diffuse scattering [39].

The CFR obtained with the AIT RT tool is derived by superposition of R_m RT paths r with the respective complex attenuation $\chi_{kar}[m]$ and delay $\tau_{kar}[m]$. The simulated CFR $\hat{h}_{ka}^{\text{RT}}[m, q]$ from user k to RX antenna a is given by

$$\hat{h}_{ka}^{(\text{RT})}[m, q] = h_{ka}^{(\text{RX})}[q] h_{ka}^{\text{TX}}[q] \sum_{r=1}^{R_m} \chi_{kar}[m] e^{-j2\pi(\tau_{kar}[m](f_c - B/2 + q\Delta f))}. \quad (3.8)$$

¹A lattice Λ^n is defined as a subgroup of \mathbb{R}^n as $\Lambda^n(\mathbf{b}_1, \dots, \mathbf{b}_n) := \{\sum_{i=1}^n \alpha_i \mathbf{b}_i : \alpha_i \in \mathbb{Z}\}$, where $\{\mathbf{b}_1, \dots, \mathbf{b}_n\} \subset \mathbb{R}^n$ is a basis.

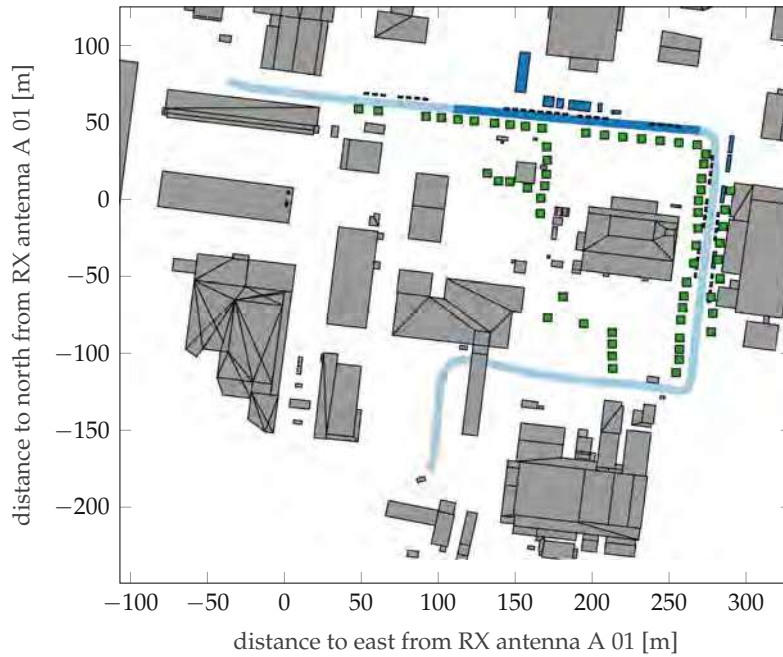


FIGURE 3.10: RT 3D model including buildings (gray), vegetation (green) and metallic structures (blue) derived from openly available building data bases. The TX node trajectory as recorded during measurements is indicated in light blue and the trajectory of interest in this thesis is indicated in dark blue.

The expressions $h_{ka}^{(\text{TX})}[q]$ and $h_{ka}^{(\text{RX})}[q]$ denote the band limiting transmit and receive filters, respectively.

The sampled CIR is calculated via the inverse Fourier transform over the bandwidth $B = Q\Delta f$

$$\hat{g}_{ka}^{(\text{RT})}[m, n] = \frac{1}{Q} \sum_{q=0}^{Q-1} \hat{h}_{ka}^{(\text{RT})}[m, q] e^{j2\pi nq/Q}, \quad (3.9)$$

with n being the delay index.

3.3.3 Stochastic Characterization of the Wireless Propagation Channel

To draw conclusions about wide-sense stationarity or the lack thereof for the RX array configurations under investigation, we revert to analyzing the moments of the wireless channels' time-variant power delay profile (PDP) and Doppler spectral density (DSD). To that end, the LSF is introduced as it provides a means of calculating the considered parameters in highly dynamic scenarios [44], [45]. The LSF characterizes the dispersion in Doppler and delay.

A certain number of consecutive measurements L within a local stationarity region is necessary to calculate the LSF in (3.10). Therefore, discrete time l is introduced to index the calculated LSFs and its moments and marginals. The time index l is often referred to in literature as the stationarity region index, while L is then the stationarity region length [13], [44] and chosen to be even in this work.

Given the time-variant frequency transfer function estimate $\hat{h}_{ka}[m, q]$ from user k to RX antenna a , the estimate of the LSF at stationarity region index l is given as [44],

[46]

$$\hat{C}_{ka}[l; n, p] = \frac{1}{IJ} \sum_{w=0}^{IJ-1} \left| \mathcal{H}_{ka}^{(G_w)}[l; n, p] \right|^2, \quad (3.10)$$

with the Doppler shift index $p \in \{-L/2, \dots, L/2 - 1\}$ and the delay index $n \in \{0, \dots, Q - 1\}$. The delay and Doppler shift resolution are defined by $\tau_s = \frac{1}{Q\Delta f}$ and $\nu_s = \frac{1}{LT^{(\text{rep})}}$, where $T^{(\text{rep})}$ is the repetition rate of the measurement. The operation $m = lL + m'$ maps the measurement time index m to the stationarity region index l . The tapered frequency response is

$$\mathcal{H}_{ka}^{(G_w)}[l; n, p] = \sum_{m=-L/2}^{L/2-1} \sum_{q=-(Q-1)/2}^{(Q-1)/2} \hat{h}_{ka}[m' + Ll, q] G_w[m', q] e^{-j2\pi(pm' - nq)}, \quad (3.11)$$

where the tapers $G_w[m, q]$ are two-dimensional DPS sequences as shown in detail in [13], [21]. The number of tapers in the time and frequency domain is set to $I = 2$ and $J = 1$, respectively [13], [47].

We calculate the PDP and DSD as projections of the LSF onto the Doppler domain and the delay domain, respectively [3], [38]:

$$\hat{\mathcal{P}}_{ka}^{(\tau)}[l; n] = \frac{1}{L} \sum_{p=-L/2}^{L/2-1} \hat{C}_{ka}[l; n, p], \quad (3.12)$$

$$\hat{\mathcal{P}}_{ka}^{(\nu)}[l; p] = \frac{1}{Q} \sum_{n=0}^{Q-1} \hat{C}_{ka}[l; n, p]. \quad (3.13)$$

Moments of the PDP and DSD To allow for a comprehensive and quantitative analysis of the time-variant PDP and DSD, we revert to their normalized moments as characterizing parameters [3, Sec. 6.5], [38, Sec. 1.4.1.5]. The following formulas for the normalized moments of PDP and DSD are taken from [38] and adopted to the used sampling in time and frequency.

The time-variant first moment of the PDP of the estimated channel transfer function $\hat{h}_{ka}[m, q]$, i.e., its time-integrated power, is calculated as

$$\hat{\mathcal{P}}_{ka}^{(\tau)}[l] = \sum_{n=0}^{Q-1} \hat{\mathcal{P}}_{ka}^{(\tau)}[l; n]. \quad (3.14)$$

The second moment is referred to as the mean delay and calculated as

$$\bar{\tau}_{ka}[l] = \frac{\sum_{n=0}^{Q-1} (n\tau_s) \hat{\mathcal{P}}_{ka}^{(\tau)}[l; n]}{\hat{\mathcal{P}}_{ka}^{(\tau)}[l]}. \quad (3.15)$$

We calculate the root mean square (RMS) delay spread by

$$\varsigma_{ka}^{(\tau)}[l] = \sqrt{\frac{\sum_{n=0}^{Q-1} (n\tau_s)^2 \hat{\mathcal{P}}_{ka}^{(\tau)}[l; n]}{\hat{\mathcal{P}}_{ka}^{(\tau)}[l]} - \bar{\tau}_{ka}[l]^2}. \quad (3.16)$$

Similarly, with the Doppler integrated power

$$\hat{\mathcal{P}}_{ka}^{(\nu)}[l] = \sum_{p=-L/2}^{L/2-1} \hat{\mathcal{P}}_{ka}^{(\nu)}[l; p], \quad (3.17)$$

and the mean Doppler

$$\bar{v}_{ka}[l] = \frac{\sum_{p=-L/2}^{L/2-1} (pv_s) \hat{\mathcal{P}}_{ka}^{(v)}[l; p]}{\hat{\mathcal{P}}_{ka}^{(v)}[l]}, \quad (3.18)$$

we obtain the RMS Doppler spread by

$$\zeta_{ka}^{(v)}[l] = \sqrt{\frac{\sum_{p=-L/2}^{L/2-1} (pv_s)^2 \hat{\mathcal{P}}_{ka}^{(v)}[l; p]}{\hat{\mathcal{P}}_{ka}^{(v)}[l]} - \bar{v}_{ka}[l]^2}. \quad (3.19)$$

We define the time-dependent average received power at time instant l as the sum over the LSF in both time and frequency [44], [48]

$$\hat{\mathcal{P}}_{ka}[l] = \frac{1}{LQ} \sum_{p=-L/2}^{L/2-1} \sum_{n=0}^{Q-1} \hat{\mathcal{C}}_{ka}[l; n, p] = \frac{1}{Q} \hat{\mathcal{P}}_{ka}^{(\tau)}[l] = \frac{1}{L} \hat{\mathcal{P}}_{ka}^{(v)}[l]. \quad (3.20)$$

Let $L(j)$ denote the set of time indices l for which the user k moves in a given region R_j , where j is the spatial region index (see also Fig. 4.13 for a visual representation). If user k is in region R_j at time instant l , then $l \in L(j)$. The size of the set $L(j)$, representing the time a user spent in a given region, is denoted by $|L(j)|$. The average received power from user k in region R_j is then defined as

$$\hat{\mathcal{P}}_{ka}[j] = \frac{1}{|L(j)|} \sum_{l \in L(j)} \hat{\mathcal{P}}_{ka}[l]. \quad (3.21)$$

For a more convenient exposition later, we also define the normalized received power from user k in region R_j by dividing with the maximum value of $\frac{1}{A} \sum_{a=1}^A \hat{\mathcal{P}}_{ka}[j]$ over all regions R_j ,

$$\bar{\mathcal{P}}_{ka}[j] = \frac{\hat{\mathcal{P}}_{ka}[j]}{\max_j \frac{1}{A} \sum_{a=1}^A \hat{\mathcal{P}}_{ka}[j]}. \quad (3.22)$$

Collinearity of the LSF We define the collinearity [13], [45] of the LSF at time l as

$$\alpha_{kaa'}[l] = \frac{\sum_{p=-L/2}^{L/2-1} \sum_{n=0}^{Q-1} \hat{\mathcal{C}}_{ka}[l; n, p] \hat{\mathcal{C}}_{ka'}[l; n, p]}{\bar{\mathcal{C}}_{ka}[l] \bar{\mathcal{C}}_{ka'}[l]}, \quad (3.23)$$

with

$$\bar{\mathcal{C}}_{ka}[l] = \sqrt{\sum_{p=-L/2}^{L/2-1} \sum_{n=0}^{Q-1} |\hat{\mathcal{C}}_{ka}[l; n, p]|^2} \quad (3.24)$$

denoting the total power of the LSF, to evaluate the stationarity of the three proposed RX conf. 1 to 3 in space. We thereby analyze, if the wireless communication channel to different RX antennas exhibits different statistical parameters. A value close to one indicates a similar distribution of multipath components in the delay-Doppler domain at a certain time (or equivalently in space). In contrast, a value close to zero indicates no similarity in the multipath component distribution.

The average spatial collinearity between RX antennas over l is defined as

$$\bar{\alpha}_{kaa'} = \frac{1}{\sum_j |L(j)|} \sum_l \alpha_{kaa'}[l] \quad (3.25)$$

and is used to assess the average value of the LSF collinearity over the full TX trajectory.

3.3.4 Stochastic Characterization of the Fading Process

Commonly, Rayleigh fading is assumed in the massive MIMO literature to achieve favorable propagation conditions and harness the full potential of the vast number of antennas. However, this assumption is under many real propagation circumstances not legitimate, and we instead observe Rician fading with a dominant path.

To determine the fading characteristics of the measured scenario, we analyze the stochastic distribution of the signal envelope over time/space. This is done by considering the first strong delay bin of the CIR in (3.6), i.e., the distribution of the set $\mathcal{G} = \{\max_n |\hat{g}_{ka}[m, n]|\}$, for a, k , and m in a given parameter set defined in (3.26). The first strong delay component critically determines the performance of communication systems based on correlation synchronization such as OFDM [49]. Large-scale fading effects on the envelope's distribution are avoided by normalizing the signal with its mean power over a sliding time window of a given length [49]. This guarantees that only small-scale fading determines power variations within the elements of \mathcal{G} . To obtain enough small-scale fading realizations, we assume stationarity over a time interval $T^{(\text{stat})}$ and use all obtained samples within this time frame. Further, since closely spaced antennas also receive different realizations of the same random fading process, we allow for more than one RX and TX antenna index.

Therefore, the set \mathcal{G} is constituted of elements chosen from discrete intervals

$$\mathcal{G} = \left\{ \max_n |\hat{g}_{ka}[m, n]| : a \in \bar{A}, k \in \bar{K}, m \in \bar{M} \right\} \quad (3.26)$$

with $\bar{A} \subseteq [1, A]$, $\bar{K} \subseteq [1, K]$ and $\bar{M} \subseteq [m_0, m_0 + T^{(\text{stat})}]$.

Fitting of the empirical and simulated envelope distribution \mathcal{G} to several well-known probability distributions is performed with the proprietary *Statistics and Machine Learning Toolbox* of Matlab. The Kolmogorov-Smirnov (KS) criterion [50]

$$\text{GoF} = \sup_z |F_Z(z) - F_G(z)| \quad (3.27)$$

is used to assess the goodness of fit (GoF) of an empirical cumulative distribution function (CDF) $F_G(z)$ to its analytical counterpart $F_Z(z)$ [49]. A good fit is indicated by a small value of GoF.

3.3.5 Massive MIMO Signal Model

To emphasize the link of the proposed channel sounding framework architecture to a widely distributed massive MIMO system, we elaborate in terms of BS and UE, as opposed to RX and TX, in what follows.

We consider an uplink massive MIMO system where $K = 2$ users $k \in \{1, 2\}$ are transmitting to a BS deploying A antennas. The channel vector for user k at symbol index m is constructed by assembling the coherently measured and sampled channel transfer function $\hat{h}_{ka}[m]$ from (3.5) into vector form,

$$\mathbf{h}_{km} = \left[\hat{h}_{1k}[m] \hat{h}_{2k}[m] \dots \hat{h}_{Ak}[m] \right]^T \in \mathbb{C}^{A \times 1}. \quad (3.28)$$

The channel vector collects the channel coefficients from user k to all A BS antennas. As all following analysis only considers one subcarrier at a time, we ease notation

by omitting the frequency index q (interpreted as a subcarrier index in this context). However, all quantities in this section are frequency dependent.

The channel vectors of all users are grouped into the channel matrix (refer to [6] for more details)

$$\mathbf{H}_m = [\mathbf{h}_{1m} \ \mathbf{h}_{2m} \ \dots \ \mathbf{h}_{Km}], \quad (3.29)$$

where, in our case, K will equal the number of UEs utilized in the channel sounding campaign.

By applying a beam-forming matrix

$$\mathbf{W}_m = [\mathbf{w}_{1m} \ \mathbf{w}_{2m} \ \dots \ \mathbf{w}_{Km}] \in \mathbb{C}^{A \times K} \quad (3.30)$$

in the uplink, the vector collecting the received symbols from all K users at time index m is

$$\hat{\mathbf{s}}_m = \mathbf{W}_m^H \mathbf{y}_m = \mathbf{W}_m^H \mathbf{H}_m \mathbf{s}_m + \mathbf{W}_m^H \mathbf{n}_m, \quad (3.31)$$

with $\mathbf{s}_m \in \mathbb{C}^{K \times 1}$ the vector collecting the transmitted information symbols of all users, $\mathbf{W}_m^H \mathbf{n}_m \sim \mathcal{CN}(\mathbf{0}, \frac{\sigma_n^2}{P} \mathbf{I}_K)$ denoting filtered complex Gaussian noise, and P the average transmit power of each user.

The received symbol estimate from one single user k at the BS is

$$\begin{aligned} \hat{s}_{km} &= \mathbf{w}_{km}^H \mathbf{y}_m = \mathbf{w}_{km}^H \mathbf{H}_m \mathbf{s}_m + \mathbf{w}_{km}^H \mathbf{n}_m \\ &= \mathbf{w}_{km}^H \mathbf{h}_{km} s_{km} + \mathbf{w}_{km}^H \mathbf{n}_m + \sum_{k' \neq k} \mathbf{w}_{km}^H \mathbf{h}_{k'm} s_{k'm} \end{aligned} \quad (3.32)$$

where the first term in the second line is the scaled signal, the second term is filtered and scaled Gaussian noise $\mathbf{w}_{km}^H \mathbf{n}_m \sim \mathcal{CN}(0, \frac{\sigma_n^2}{P})$, and the third term is interference from other users $k' \neq k$.

Note that the measurement framework shown in Section 3.2 in itself does not introduce any inter-user interference as the users transmit their respective sounding sequence separated in time. However, interpreting the measured channel transfer function as entries in the channel matrix (3.29) provides a signal model that assumes simultaneous transmission of all users, thus yielding the interference term in (3.32).

The performance of a massive MIMO systems in terms of SINR (or equivalently spectral efficiency) is largely determined by the properties of the current channel matrix realization \mathbf{H}_m and its statistics. We therefore establish in the following the methods to assess the characteristics of the channel matrix and, ultimately, the quality of a wireless communication system based on it.

SINR and Channel Aging Rate and reliability for user k are mainly determined by the instantaneous SINR [6]

$$\eta_k = \frac{|\mathbf{w}_{km}^H \tilde{\mathbf{h}}_{km}|^2}{\frac{\sigma_n^2}{\sqrt{P}} \mathbf{w}_{km}^H \tilde{\mathbf{h}}_{km} + |\mathbf{w}_{km}^H (\mathbf{h}_{km} - \tilde{\mathbf{h}}_{km})|^2 + \sum_{k' \neq k} |\mathbf{w}_{km}^H \mathbf{h}_{k'm}|^2}, \quad (3.33)$$

defined as the ratio of the signal component to the interference and noise component, see also (2.33). We consider in what follows the beam-forming vectors \mathbf{w}_{km} to being

calculated via the RZF approach [12], [51] by solving

$$\mathbf{W}_m = [\mathbf{w}_{1m} \ \mathbf{w}_{2m} \ \dots \ \mathbf{w}_{Km}] \quad (3.34)$$

$$= \tilde{\mathbf{H}}_m \left(\tilde{\mathbf{H}}_m^H \tilde{\mathbf{H}}_m + \frac{\sigma_n^2}{P} \mathbf{I}_K \right)^{-1}, \quad (3.35)$$

which is approximated well by the zero-forcing (ZF) solution

$$\mathbf{W}_m \approx \tilde{\mathbf{H}}_m \left(\tilde{\mathbf{H}}_m^H \tilde{\mathbf{H}}_m \right)^{-1}, \quad (3.36)$$

if $P \gg \sigma_n^2$, i.e., if the pilot power during CSI acquisition is far greater than the noise power. If the measurement SNR for obtaining the channel vector realizations in (3.28) is large, $\tilde{\mathbf{H}}_m^H \tilde{\mathbf{H}}_m + \frac{\sigma_n^2}{P} \mathbf{I}_K \approx \tilde{\mathbf{H}}_m^H \tilde{\mathbf{H}}_m$ holds and the regularization term is negligible. This is the case for all measurement campaigns described in the Chapter 4.

To quantify the effect of channel aging, we deliberately introduce outdated channel matrices to calculate the beam-forming matrices in (3.36). The outdated channel matrix $\tilde{\mathbf{H}}_m$ is defined similar to (3.29) as the outdated channel vectors $\tilde{\mathbf{h}}_{km}$ grouped into a matrix, i.e.,

$$\tilde{\mathbf{H}}_m = [\tilde{\mathbf{h}}_{1m} \ \tilde{\mathbf{h}}_{2m} \ \dots \ \tilde{\mathbf{h}}_{Km}], \quad (3.37)$$

$$\tilde{\mathbf{h}}_{km} = [\hat{h}_{1k}(mT_R + \Delta t) \ \hat{h}_{2k}(mT_R + \Delta t) \ \dots \ \hat{h}_{Ak}(mT_R + \Delta t)]^T. \quad (3.38)$$

The beam-forming matrix \mathbf{W}_m determines the ability of a massive MIMO system to maximize the signal component and minimize interference from other users. Acquisition of timely CSI (i.e., with small delay Δt) $\tilde{\mathbf{H}}_m \approx \mathbf{H}_m$ that is necessary to calculate the beam-forming matrix is, however, non-trivial if high mobility is involved. By the time the beam-forming matrix is applied, it might already be out-dated (i.e., $\tilde{\mathbf{H}}_m \not\approx \mathbf{H}_m$) and the instantaneous SINR in (3.33) decreases. This effect is called *channel aging* and prevents massive MIMO systems to operate in high mobility scenarios without special measures such as channel prediction [8].

Channel Hardening The large number of BS antennas $A \gg K$ leads to linear beam-forming (e.g., ZF as outlined above) being close to optimal. Additionally, the law of large numbers guarantees that random fluctuations of the signal component become less probable and the effective channel

$$\gamma_{km} = \mathbf{w}_{km}^H \tilde{\mathbf{h}}_{km} \quad (3.39)$$

becomes quasi-deterministic – a process called *channel hardening* [17].

To assess if channel hardening is occurring, we investigate the ratio of the effective gain variance to its squared mean

$$\beta_k = \frac{\text{Var}\{\gamma_{km}\}}{\mathbb{E}\{\gamma_{km}\}^2}, \quad (3.40)$$

similar to [15]–[17]. Low values of β_k indicate a low probability of the channel gain γ_{km} deviating significantly from its mean.

The variance in (3.40) is estimated as

$$\text{Var}\{\gamma_{km}\} = \frac{1}{L-1} \sum_{m=-L/2+1L}^{L/2-1+1L} \left(\left| \mathbf{w}_{km}^H \tilde{\mathbf{h}}_{km} \right|^2 - \mathbb{E}\{\gamma_{km}\} \right)^2 \quad (3.41)$$

from the measurement data, and the mean is estimated as

$$\mathbb{E}\{\gamma_{km}\} = \frac{1}{L} \sum_{m=-L/2+1L}^{L/2-1+1L} \left| \mathbf{w}_{km}^H \tilde{\mathbf{h}}_{km} \right|^2. \quad (3.42)$$

Singular Value Spread To quantify if users can be addressed in orthogonal subspaces of the channel matrix via beam-forming, we utilize the singular value spread (SVS) defined as the ratio

$$\zeta(\mathbf{H}_m) = \frac{\zeta_{km}^{(\max)}}{\zeta_{km}^{(\min)}} \quad (3.43)$$

of the largest to the smallest singular value ζ_{km} of the channel matrix \mathbf{H}_m .

The singular values are defined by decomposing the channel matrix

$$\mathbf{H}_m = \mathbf{U}_m \Sigma_m \mathbf{V}_m^H \quad (3.44)$$

into unitary matrices $\mathbf{U}_m \in \mathbb{C}^{A \times A}$, $\mathbf{V}_m \in \mathbb{C}^{K \times K}$, and the rectangular matrix $\Sigma_m \in \mathbb{C}^{A \times K}$ with K singular values ζ_{km} on its main diagonal.

A small SVS indicates that the channel vectors $\tilde{\mathbf{h}}_{ka}[m]$ reside in orthogonal eigenspaces whereas a large value of the SVS indicates their linear dependency. With orthogonal channel vectors and through the law of large numbers, small scale fading is eliminated, and channel hardening is achieved [17].

3.4 Related Literature

The research work on cell-free massive MIMO has increased tremendously over the last five years, see, e.g., [33], [34], [52], [53] and the references therein, as it is considered an enabling technology for beyond 5G systems. While anticipated key characteristics are already known through extensive analysis and simulation, empirical validation is missing in most instances.

In [34], the authors put forward a cost-efficient architecture called *radio stripes* for cell-free systems. The architecture includes antennas and associated processing units, synchronization, data transfer, and power supply within a single cable, thus facilitating deployment considerably. However, no empirical data obtained with this approach is publicly available. With the proposed measurement framework presented in this thesis, linear deployment strategies like the radio stripes technology can be analyzed based on real-world data for the first time.

Wireless propagation channel measurements at 2.6 GHz with a virtual wide-aperture array measuring 7.3 m were first reported in [54]. The proposed measurement approach involves one antenna that is moved to form a virtual array, and is only suitable for static scenarios without mobility.

In [55] the authors describe a comparative study of MIMO antenna geometries, with aperture sizes ranging from 0.3 m to 6 m. Eight fully parallel receive units and fast switching was used to characterize the system with 64 BS antenna elements.

A first cell-free channel measurement using a drone with a single transmit antenna that flies from one radio unit (RU) position to the next was reported in [56]. This

method does not provide coherent impulse responses from the RU positions but allows a quantitative assessment of properties such as the uplink energy efficiency [57]. Furthermore, UE mobility and scatterer mobility cannot be captured by the distributed virtual array measurement principle of [56].

Chapter 4

Measurement Campaigns and Results

4.1 Contents of this Chapter

The promising features of massive MIMO systems, that were investigated analytically and numerically in Chapter 2, are highly dependent on the characteristics of the wireless channel. Verifying the underlying assumptions about its key features and statistics is therefore crucial to draw relevant and realistic conclusions. To achieve this, we utilize the massive MIMO sounding framework and data processing tools from Chapter 3 and design two measurement campaigns accordingly. The obtained data is analyzed to substantiate the results from Chapter 2, in accordance with **O3**.

In this chapter, the conceptualization and realization of those measurement campaigns is described (**M3**). For each measurement campaign, the analysis results of the empirical data and their relevance to the theoretic results are presented (**M4**).

A distributed measurement campaign *DIST*, presented in Section 4.2, was carried out in 2018 and demonstrated the intended functionality of the massive MIMO channel sounder. Both collocated and distributed BS antenna configurations were deployed. The *DIST* measurement campaign description and results are published in

[10] D. Löschenbrand, M. Hofer, L. Bernadó, G. Humer, B. Schrenk, S. Zelenbaba, and T. Zemen, "Distributed massive MIMO channel measurements in urban vehicular scenario", in *13th European Conference on Antennas and Propagation (EuCAP)*, Krakow, Poland, 2019.

[11] D. Löschenbrand, M. Hofer, B. Rainer, and T. Zemen, "Empirical and simulated performance evaluation of distributed massive MIMO", in *Asilomar Conference on Signals, Systems, and Computers (ASILOMAR)*, 2019.

A widely distributed measurement campaign *WIDE*, presented in Section 4.3, was carried out in 2022. It included, in addition to a collocated and a distributed RX array configuration, also the world's first fully parallel massive MIMO wide aperture RX array configuration. The *WIDE* measurement campaign description and results are published in

[9] D. Löschenbrand, M. Hofer, L. Bernadó; S. Zelenbaba, and T. Zemen, "Towards cell-free massive MIMO: A measurement-based analysis", *IEEE Access*, 2022. DOI: 10.1109/ACCESS.2022.3200365.

4.2 DIST Measurement Campaign

We conducted a distributed massive MIMO vehicle to infrastructure (V2I) measurement campaign in an urban environment around the AIT office premises in Vienna

(48.269 080°N, 16.427 637°E) in 2018. In this measurement campaign, referred to as DIST in the following, two different array geometries with apertures ranging from 2 m to 8 m were installed and tested. It allows for an analysis of the merits and drawbacks of distributed massive MIMO systems in comparison to collocated massive MIMO systems currently being deployed and operational worldwide.

4.2.1 Measurement Scenario

The RX of the massive MIMO channel sounder is positioned on top of an office building at approximately 15 m height. It features 32 parallel RX ports grouped into two antenna arrays with 16 dual polarized patch antenna elements each. With these two RX antenna arrays, a *collocated* (antenna arrays next to each other with 0.5 m distance, see Fig. 4.1a) and a *distributed* (antenna arrays with 7.5 m distance, see Fig. 4.1b) setup is realized. For both setups, the antenna arrays are facing east, see Fig. 4.3. Figure 4.1 shows pictures of the measurement hardware on the roof of the office building for both the collocated and distributed RX antenna array configuration.

Two transmitters, TX 1 and TX 2, are mounted into one van with their respective omnidirectional monopole antennas being placed on the van's roof with a distance of 1 m, see Fig. 4.2b. Additionally, two GNSS antennas are mounted on the roof of the van and connected to the Rubidium clock to enable precise and redundant localization while moving. Inside the van, the controller, Rubidium clock, SDR and the PAs are fixed in a 19-inch rack and powered by a UPS, see Fig. 4.2a. The transmit power is 25 dBm for TX 1 and 20 dBm for TX 2, which is below the 1 dB compression point of the respective PAs.

The TX follows a fixed trajectory on a two-way street with light traffic through an urban scenario with vegetation, parking cars, metallic construction site objects and factory halls. One measurement on this route takes 90 s. We repeatedly run the TX on the defined route with a reproducible velocity profile and perform measurements. This way we generate multiple realizations of the same scenario to gain statistical significance. The maximum speed of the TX is approximately 50 km/h (13.9 m/s). The position of the car is recorded via GNSS and mapped to the obtained channel measurements. For each RX antenna array setup, ten measurement runs are conducted to gain statistical significance.

In what follows, we will focus on the 20 s - 40 s segment of one measurement run. The corresponding traveled distance is 115 m - 270 m as indicated in Fig. 4.3. The scenario under consideration is the approaching of a crossing. The distance from the RX to the crossing is 285 m. The TX start close to the RX and moves away, approaching the crossing with approximately 10 m/s. It then slows down to make a right turn.

Figure 4.3 shows the measurement scenario with the TX van trajectory (carrying TX 1 and TX 2), the RX antenna array position on top of the office building and facing east. Table 4.1 lists parameters used in the measurement.

Additionally, we utilize the obtained data to verify the correct operation of the RT tool introduced in Section 3.3.2. Given the computational complexity of simulating CIRs in a complex urban environment with the RT, we did not, however, replicate the full empirical massive MIMO data set.

4.2.2 Single Antenna Results

To analyze the time-variant characteristics of the channel impulse response \hat{g}_{ka} (3.6) for both measurements and RT, we revert to the time-variant PDP (3.12) and the



(a) DIST measurement campaign, collocated RX setup.



(b) DIST measurement campaign, distributed RX setup.

FIGURE 4.1: DIST measurement campaign, collocated (top) and distributed (bottom) RX setup.



(a) DIST measurement campaign, TX setup of hardware in the van.



(b) DIST measurement campaign, TX and GNSS antennas on vans roof.

FIGURE 4.2: DIST measurement campaign, TX antenna setup on the van roof.

TABLE 4.1: Measurement parameters and their respective values for DIST measurement campaign.

Parameter	Value
carrier frequency f_c	3.52 GHz
number of tones Q	481
tone spacing Δf	240 kHz
bandwidth B	115.44 MHz
repetition rate	1 ms
max. Doppler frequency	500 Hz
max. velocity	42 m/s
TX 1 power	25 dBm
TX 2 power	20 dBm
measurement time per run	90 s
runs per scenario	10
RX array aperture	8 m (dist.), 1.5 m (coll.),

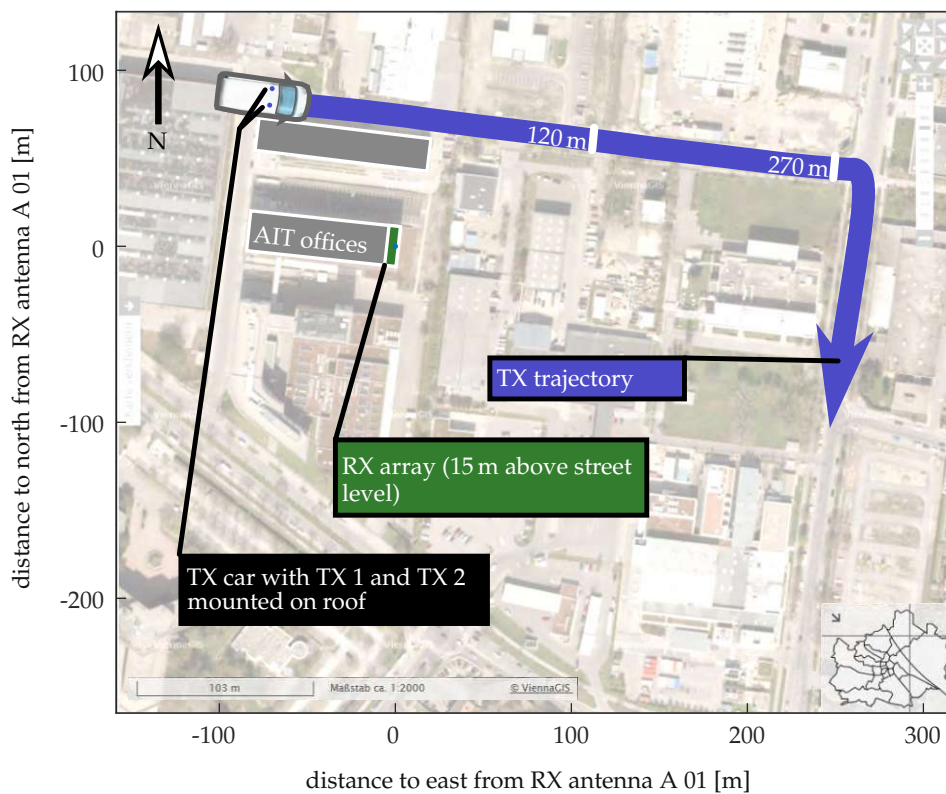


FIGURE 4.3: Top view of the urban scenario of the DIST measurement campaign in Vienna. The full trajectory of the van carrying TX 1 and TX 2 is indicated in blue and the trajectory part of interest is marked with white lines. The position of the RX array on top of the office building (both for collocated and distributed setup) is indicated in green, and the individual antenna element pattern main lobe is facing to the east.

time-variant DSD (3.13). They are obtained as marginals of the LSF (3.10) (see [44], [48] for more details). The time index m is chosen as a multiple of the channel sounder repetition rate, i.e., absolute time $t = mT^{(\text{rep})}$. Since the time variability in our setup mainly arises through the movement of the TX and there is detailed geometrical knowledge of the scenario available (position and velocity through GNSS tracking for the measurements and the geometrical model for RT), we assume a one-to-one mapping of time to spatial position of the TX antennas. Therefore, m can both be interpreted as a temporal and spatial index.

Figure 4.4 (top) shows an exemplary PDP for one TX and one RX antenna. Due to the large bandwidth, the single delay components from various scattering sources are clearly visible in the PDP. The LOS is interrupted by trees next to the street. This causes large-scale power variations of the main component of more than 10 dB. Qualitatively, we observe a good match between measurements (top) and RT results (bottom) in Fig. 4.4. The LOS shows the same temporal characteristics, although the power level fluctuation due to vegetation next to the street is less pronounced with RT. The delay distribution of diffuse scattering over time is well captured in the simulation. Note that the chosen RT approach is spatially consistent and allows for continuous contributions of diffuse scatterers.

Figure 4.5 (top) shows an exemplary DSD evaluated using (3.10). The strongest component in the DSD is caused by the TX driving away from the RX and approaching the crossing with ≈ 10 m/s, causing a Doppler shift of ≈ 120 Hz. Multiple scattering objects are passed by the TX, causing traces from positive to negative Doppler. Deceleration of the TX before turning right on the crossing causes smaller Doppler shifts of the main component and all the scattering components at the end of the shown segment. Again, we observe a good match between measurements (top) and RT results (bottom) in Fig. 4.5. The simulated RT DSD shows the same strong LOS path as the measurement, but without much large-scale fading due to vegetation. The changing Doppler frequencies of the diffuse scattering over time reproduce the measurement data very well and are spatially consistent.

4.2.3 Stochastic Evaluation

As described in Section 3.3.4, we aim to determine the fading characteristics of the measured scenario to validate or falsify the common assumption of Rayleigh fading statistics in massive MIMO systems. We analyze the stochastic distribution of the signal envelope over time/space. This is done by considering the first strong delay bin of the CIR in (3.6), i.e., the distribution of the set $\mathcal{G} = \{\max_n |\hat{g}_{ka}[m, n]|\}$, for a , k , and m in a given parameter set defined in (3.26). The channel sounder measurements are performed with a bandwidth of 115.44 MHz. For the analysis in what follows, however, we restrict the CIR to a bandwidth of $B = 20$ MHz to observe realistic fading behavior of the delay bin under consideration.

The sliding window length to normalize the signal with its mean power is 600 ms [49]. To obtain enough small-scale fading realizations, stationarity over a time interval $T^{(\text{stat})} = 500$ ms is assumed (equivalent to at most 7 m $\approx 82\lambda$ with a maximum speed in our scenario of 13.9 m/s). We use all obtained samples within this time frame.

To analyze which probability distribution fits the measurement data best, we choose the realization set \mathcal{G}

$$\mathcal{G} = \left\{ \max_n |\hat{g}_{ka}[m, n]| : a \in \bar{A}, k \in \bar{K}, m \in \bar{M} \right\} \quad (4.1)$$

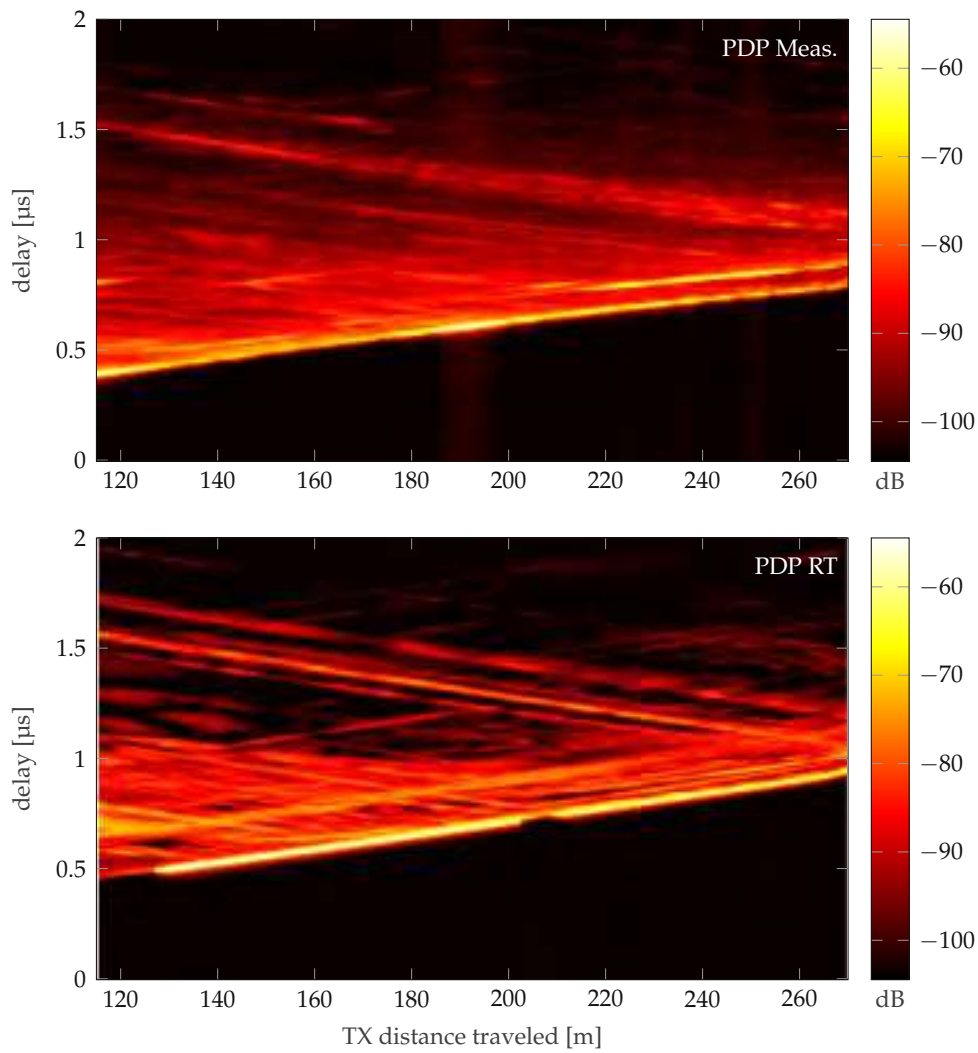


FIGURE 4.4: Comparison of measured and simulated PDP over distance traveled by the TX. The PDP shows a rich scattering environment with a strong LOS path, a second strong path with a delay of 120 ns from 210 m – 270 m and various additional multipath components.

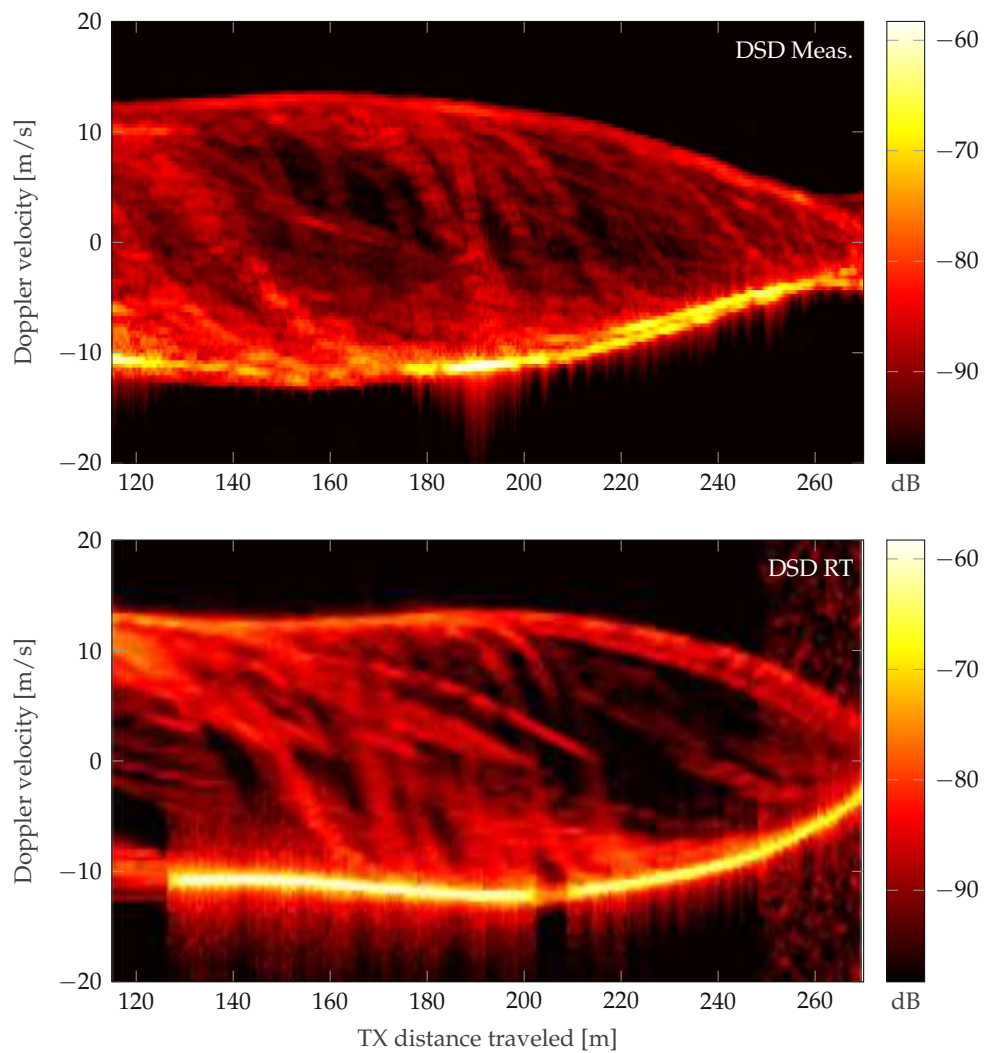


FIGURE 4.5: Comparison of measured and simulated DSD over distance traveled by the TX. The DSD shows a strong component with increasing negative Doppler shift. The TX is moving away from the RX, approaching a crossing with ≈ 40 km/h and decelerating before turning right.

from (3.26) with $\bar{A} = [1, 16]$, $\bar{K} = 1$ and $\bar{M} = [m_0, m_0 + T^{(\text{stat})}]$ and fit the well known Rayleigh and Rice distribution as well as other common probability distributions. The time index m_0 is varied to obtain several fits along the trajectory of interest.

To assess the GoF of an empirical CDF $F_G(z)$ to its analytical counterpart $F_Z(z)$, we utilize the KS criterion

$$\text{GoF} = \sup_z |F_Z(z) - F_G(z)| \quad (4.2)$$

as introduced in (3.27). A good fit is indicated by a small value of GoF.

The probability density function (PDF) and CDF of Rayleigh distributed random variable z with the scale parameter w are defined as

$$f(z; w) = \frac{z}{w^2} e^{-z^2/(2w^2)}, \quad (4.3)$$

$$F(z; w) = 1 - e^{-z^2/(2w^2)}, \quad (4.4)$$

respectively. The PDF and CDF of a Rice distributed random variable z with the shape parameters w and ν are given by

$$f(z; \nu, w) = \frac{z}{w^2} e^{-(z^2+\nu^2)/(2w^2)} I_0\left(\frac{z\nu}{w^2}\right), \quad (4.5)$$

$$F(z; \nu, w) = 1 - Q_1\left(\frac{\nu}{w}, \frac{z}{w}\right), \quad (4.6)$$

respectively. $Q_1(\cdot, \cdot)$ denotes the Marcum-Q-function of first order. A Rayleigh distribution arises for the special case $\nu = 0$.

Given the shape parameters w and ν of a Rician distributions for the realization set \mathcal{G} , the Rician K -factor describing the power ratio of the LOS path to all other multipath contributions is defined as

$$\kappa(\mathcal{G}) = \nu^2/2w^2. \quad (4.7)$$

Figure 4.6 shows the box plot of the GoF (3.27) for all fitted distributions to the measurement data along the TX trajectory. Clearly, the assumption of Rayleigh fading is not valid in our scenario. Assuming Rician fading, we observe a good fit (low GoF) with low median (horizontal line in the box) and few outliers. Other probability distributions do not provide a significantly better GoF and are therefore not considered further.

4.2.4 Key Findings

Summarizing the single antenna results of the DIST measurement campaign, we note the following.

- Given the large bandwidth and high repetition time of the massive MIMO channel sounding framework introduced in Chapter 3, detailed analysis of the wireless channel in terms of PDP and DSD is possible. Individual paths, and their respective delay and Doppler values, can be identified. Moreover, we show by investigation of the GoF that for the V2I scenario under investigation, a Rician distribution is a better fit than a Rayleigh distribution for the fading statistics.
- The RT tool introduced in Chapter 3 is able to consistently reproduce the the DSD and PDP of the measured CIRs. Initial results also show that the

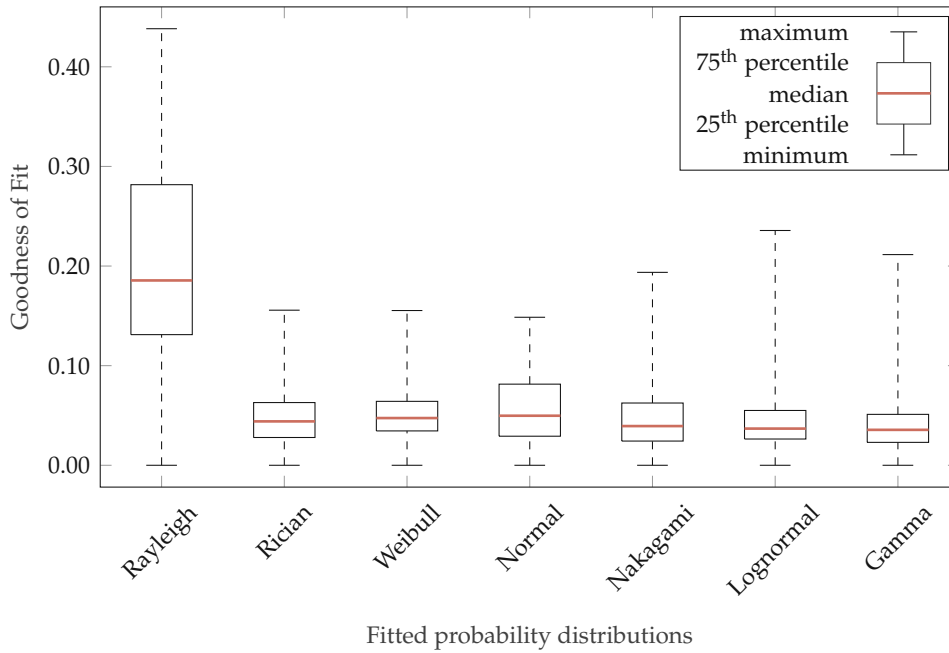


FIGURE 4.6: Box plot of the GoF for several probability distributions. The boxes span the 25 – 75 percentile and the horizontal line in the box shows the median GoF. The whiskers extend from the minimum to the maximum value.

fading statistics are accurately reproduced by RT simulations. However, we don't include a detailed analysis here because the computational complexity of calculating enough CIRs to reach statistical significance is prohibitively high.

4.2.5 Massive MIMO Results

With the channel sounding framework introduced in Chapter 3, all 64 channels from $K = 2$ TX antennas to $A = 32$ RX antennas are captured in parallel. We therefore can construct the measured channel vectors $\mathbf{h}_{km} \in \mathbb{C}^{A \times 1}$ and channel matrices $\mathbf{H}_m \in \mathbb{C}^{A \times K}$ according to (3.28) and (3.29), respectively. In this context, we assume that the RX antenna array mimics a massive MIMO BS and the TX represent UEs, and use this nomenclature instead.

SVS The SVS is often referred to as a measure of *favorable propagation* in massive MIMO systems [58]. Under favorable propagation scenarios, the inner product of the instantaneous channel matrix \mathbf{H}_m with itself approaches a diagonal matrix $\mathbf{H}_m^H \mathbf{H}_m \approx \mathbf{h}_m \mathbf{I}_K$, and thus linear precoding becomes close to optimal. SVSs close to one indicate uncorrelated channel vectors which do not lie in the same eigenspace and thus facilitate interference cancellation through ZF or RZF. We evaluate the SVS $\zeta(\mathbf{H}_m)$ (or in other words, the condition number) of the measured channel matrix \mathbf{H}_m according to (3.43).

Figure 4.7 shows the SVS for the measured channel matrix both in the distributed (7.5 m BS array distance, bottom) and the collocated (0.5 m BS array distance, top) case. The distributed BS configuration exhibits three distinct spikes at the exact times when there is LOS (also refer to Figs. 4.4 and 4.5). Surprisingly, the collocated case in Fig. 4.7 (top) does not exhibit the same spikes and shows a lower SVS in general.

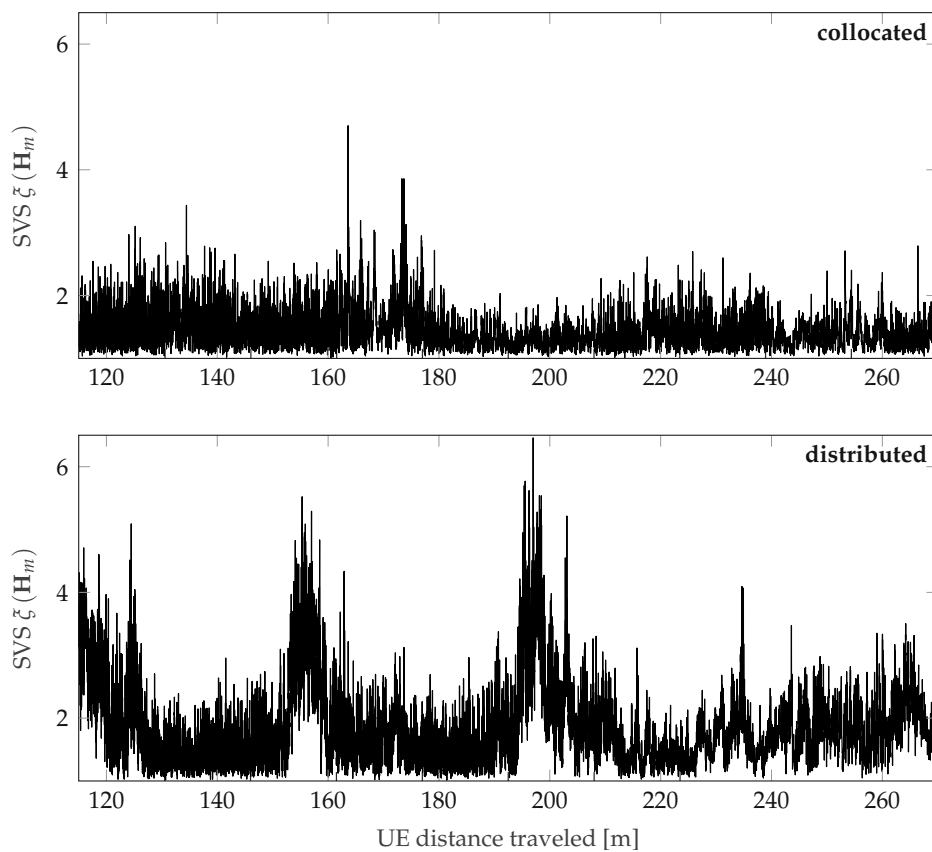


FIGURE 4.7: SVS for one run with the BS antennas collocated (top) and distributed (bottom). The three spikes in the distributed case coincide with the three LOS regions in Figs. 4.4 and 4.5. The collocated BS setup does not show this behavior.

Considering subsets of the measured channel matrices and performing a statistical evaluation over multiple measurement runs offers the possibility to evaluate the empirical probability distribution of the SVS for a varying number of BS antennas A , see Fig. 4.8. For increasing A , the SVS and therefore the probability of highly correlated channel vectors decreases in general. Interestingly, the collocated BS configuration again seems to outperform the distributed case. For the case of $A = 16$, they are chosen to be arranged horizontally, i.e., using only the lower row of antenna array elements on both BS arrays (see Fig. 3.3). Adding another 16 antennas on top (i.e., the upper row of BS antenna array elements) to a total of $A = 32$ does not decrease the average SVS significantly. This hints at low angular diversity in the elevation domain.

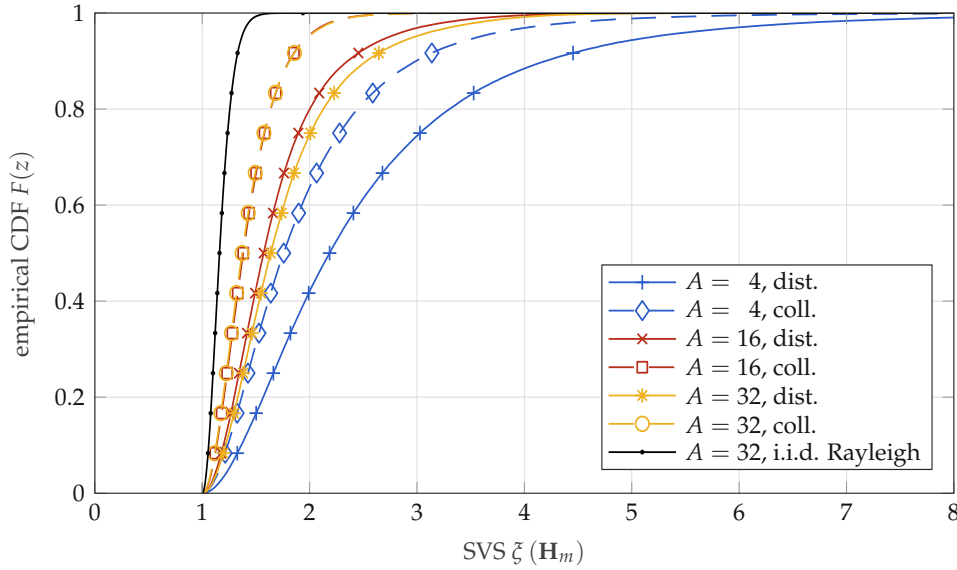


FIGURE 4.8: Empirical CDF of the SVS over 10 runs with the distributed setup and 10 runs with the collocated setup. A subset with of the measured 32×2 channel matrix with size 4×2 and 16×2 is used to simulate less BS antennas.

SVS and Rician K -factor For every Rician distribution fit along the UE trajectory, we evaluate the Rician K -factor $\kappa(\mathcal{G})$ to analyze its spatial dependencies and characteristics. Further, we perform two separate fits for each of the BS antenna arrays, i.e., for $a \in [1, 16]$ and $a \in [17, 32]$. The top plot in Fig. 4.9 shows $\kappa(\mathcal{G})$ for the first (blue) and second (red) BS array for the distributed BS setup. We observe three regions (i)-(iii) with increased LOS contributions. In region (ii) only the first BS array exhibits LOS propagation conditions whereas the K -factor for the second array stays low.

The top plot in Fig. 4.10 shows $\kappa(\mathcal{G})$ for the first (blue) and second (red) BS array for the collocated BS setup. Again, we observe three regions (i)-(iii) with increased LOS contributions. In region (ii), given the proximity of the BS arrays, both exhibit high K -factors.

The SVS is calculated for the full measured channel matrix $\mathbf{H}_m \in \mathbb{C}^{A \times K}$ at every position along the UE trajectory of interest according to (3.43). The mean of 50 consecutive SVS values $1/50 \sum_{m=m_0}^{m_0+49} \zeta(\mathbf{H}_m)$ is then plotted over the position associated with $m_0 + 25$.

The bottom plot of Fig. 4.9 shows the SVS $\zeta(\mathbf{H}_m)$ over the position for the distributed BS antenna configuration. We observe three regions (i)-(iii) with increased

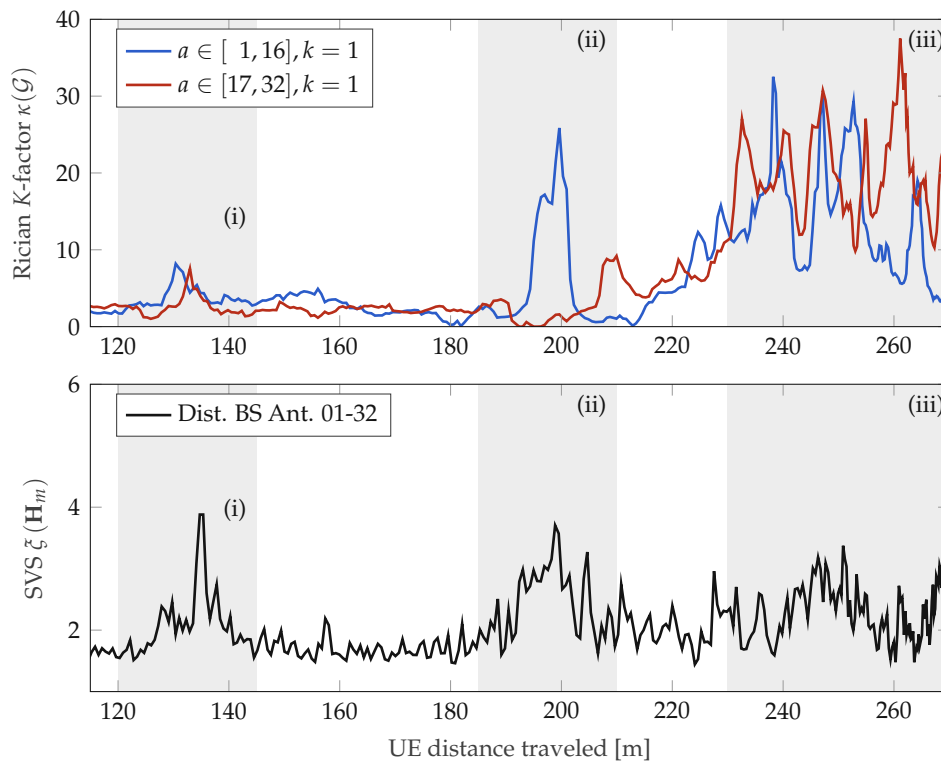


FIGURE 4.9: Rician K-factor $\kappa(\mathcal{G})$ (top) and SVS $\zeta(\mathbf{H}_m)$ (bottom) over UE position from measured data for the distributed BS setup.

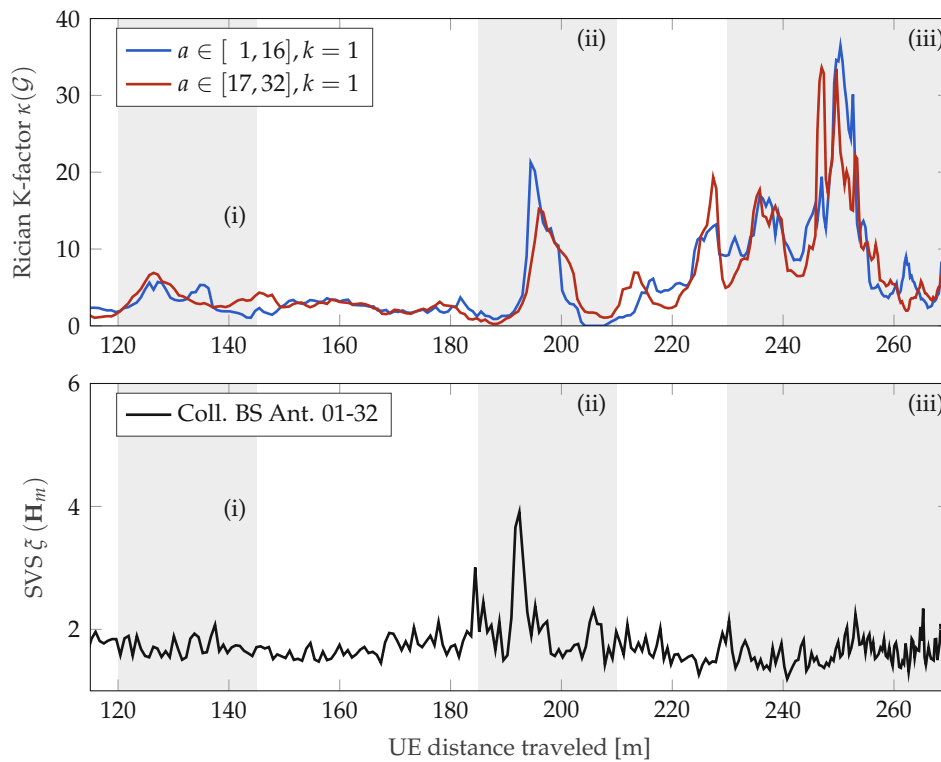


FIGURE 4.10: Rician K-factor $\kappa(\mathcal{G})$ (top) and SVS $\zeta(\mathbf{H}_m)$ (bottom) over UE position from measured data for the collocated BS setup.

SVS and a corresponding decrease in orthogonality between the channel vectors \mathbf{h}_{1a} and \mathbf{h}_{2a} . The three regions coincide with the strong LOS occurrences identified with the Rician K -factor.

The bottom plot of Fig. 4.10 shows the SVS $\zeta(\mathbf{H}_m)$ over the position for the collocated BS antenna setup. We observe only one region (ii) with increased SVS whereas regions (i) and (iii) show low SVS values despite high K -factors. Therefore, in terms of the SVS, the collocated BS setup is the preferred one in this particular scenario.

SE The orthogonality of the channel vectors directly impacts the SINR and therefore the achievable uplink SE, see (2.37). In Fig. 4.11 we show a comparison of the sum SE $= \sum_{k=1}^K SE_k$ for the distributed and collocated BS configuration. For this, the instantaneous SE is calculated according to (2.37) for every position along the UE trajectory and afterwards the mean over 50 consecutive positions is obtained. The mean SNR over all positions under consideration is normalized to be 6 dB. In the plot, we clearly observe high SE in the LOS regions (i)-(iii) for the collocated BS setup, meaning that this setup can harvest the high received power of the LOS while keeping the SINR low. For the distributed setup, the aforementioned effects cancel each other out, resulting in a more or less constant sum SE below the level of the collocated setup.

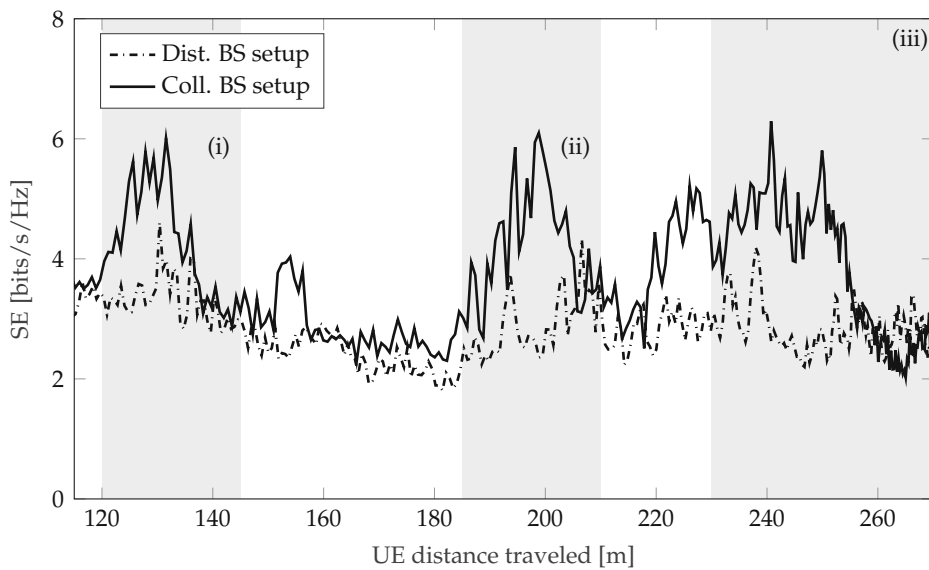


FIGURE 4.11: Ergodic achievable uplink sum SE over UE position for a mean SNR of 6 dB. In LOS propagation conditions, the collocated BS setup achieves a higher sum SE.

To avoid coincidental results, we performed the sum SE analysis over 6 UE trajectory runs for both the distributed and collocated BS setup. Fig. 4.12 shows the empirical CDF of the ergodic achievable uplink sum SE for this analysis. Again, the collocated BS setup shows clear performance benefits with a higher achievable sum SE on average.

4.2.6 Key Findings

Summarizing the massive MIMO results of the DIST measurement campaign, we note the following.

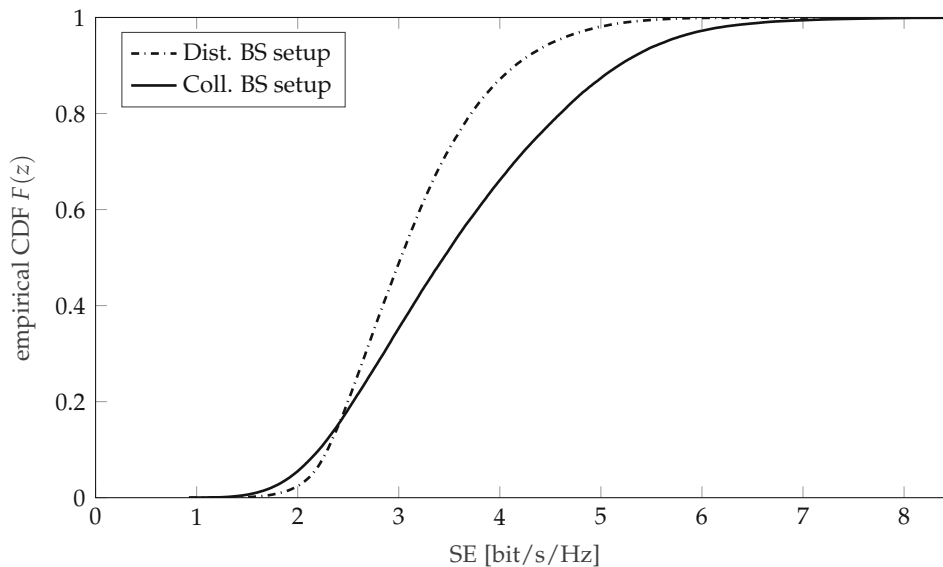


FIGURE 4.12: Empirical CDF of the ergodic achievable uplink sum SE for realizations over the UE trajectory from 6 measurement runs.

- Analysis of the SVS, both for a single run of the UE along its trajectory as well as over several runs, shows significantly lower values for the collocated BS antenna array setup, as compared to the distributed configuration. We conclude that the collocated BS configuration is better suited to apply beam-forming for two closely spaced UEs. This effect cannot be traced back to different LOS conditions for the two BS antenna arrays. It is suspected to be caused by the increased beam-forming capabilities of the collocated configuration, as it features 0.6λ -spaced antennas over almost the whole aperture. The distributed configuration, on the contrary, acts as two separate arrays with decreased aperture.
- The insights from the SVS analysis also reflect in the SE results. Both for a single UE run and on average over several runs, the collocated BS configuration yields significantly higher SE compared to the distributed configuration. The latter provides no benefit in any part of the trajectory under investigation and is lower by 0.4 bit/s/Hz (12 %) on average.

This result negates the argumentation of Chapter 2 to some extent, as it is commonly considered beneficial to decrease spatial correlation of BS antennas (i.e., by distributing the BS antennas). In order to investigate further, a second measurement campaign is devised that replicates the collocated and distributed BS configuration, but also includes a third, widely distributed, BS configuration. It is presented in the following.

4.3 WIDE Measurement Campaign

We conducted a widely distributed massive MIMO V2I channel sounding campaign in March 2022 at the premises of AIT in Vienna, Austria ($48.269\ 080^\circ\text{N}$, $16.427\ 637^\circ\text{E}$). In this campaign, referred to as WIDE in the following, three different array geometries with apertures ranging from 2 m to 46.5 m were installed and tested. It allows for an analysis of the merits and drawbacks of widely distributed and cell-free systems in comparison to conventional massive MIMO systems currently being deployed and operational worldwide.

Cell-free massive MIMO systems are a revolutionary new architecture for future mobile communications systems [33]. BS antennas are distributed in space over a large geographical area and processed coherently at a central BPU. This architecture enables similar properties as known from massive MIMO systems, such as high spectral efficiency using linear processing, and exploiting channel reciprocity between uplink and downlink. However, crucial improvements are achieved by distributing the BS antennas in space, such as (i) a strong transmit energy reduction due to reduced distance to the UE, (ii) a consistent throughput over the coverage area avoiding the strong throughput drop at cell edges, and (iii) mitigation of large-scale fading [53].

So far, widely distributed and cell-free massive MIMO systems have been explored from a theoretical point of view (see [33] and the references therein). Empirical evidence on propagation conditions in those systems is missing, although being of fundamental importance. Cell-free systems can be seen as a widely distributed antenna array with a large aperture, causing common far-field assumptions (e.g., plane wave propagation) to not hold and propagation conditions to differ substantially from BS antenna to BS antenna. In other words, the propagation conditions for mobile users are non-stationary in space and time.

The WIDE measurement campaign described in the following is, to the best of our knowledge, the world's first empiric attempt to verify the anticipated propagation conditions and consequential benefits of widely distributed massive MIMO systems.

4.3.1 Measurement Scenario

Widely distributed and cell-free massive MIMO systems are envisioned to be deployed in urban environments, as they potentially mitigate the burden of large-scale fading, i.e., blocking by buildings, vegetation, cars etc. The widely distributed massive MIMO channel sounding campaign WIDE is designed to capture these urban channel characteristics, including mobility, multipath propagation, blocking and transition from LOS to non-line of sight (NLOS).

The channel sounding framework as described in Chapter 3 is used to conduct the widely distributed channel measurements. Two vertically polarized monopole transmit antennas are mounted on the rooftop of a van right above the driving seat and the passenger seat, respectively. They are acting as TX and are referenced in the following as TX 1 and TX 2, respectively. Both TX are following a fixed trajectory for all measurements, with velocities ranging from 15 km/h to 60 km/h. The trajectory is divided into eight regions R_s , $s \in \{1, \dots, 8\}$, with a length of approximately 40 m each, for easy referencing and location-specific data evaluation. Figure 4.13 shows a top view of the scenario under consideration, with the TX trajectory and the regions R_1 to R_8 indicated in blue. The starting position of the TX is marked with a white van icon.

On the RX side, 32 array elements consisting of single patch antennas are positioned on the roof top of an office building at a height of 15 m as a horizontal linear array, with vertical polarization and their individual main lobe facing north. The RX antennas are receiving the signal transmitted by the TX. The green area in Fig. 4.13 shows the position of the RX array. Since there is an office building of similar height to the north of the linear RX antenna array (in the directions the individual patch antenna array elements are facing), regions R_3 to R_5 of the TX trajectory are exhibiting NLOS conditions. Regions R_1 and R_2 are characterized as LOS with the main direction of TX movement perpendicular to the RX antenna array, while regions R_6 , R_7 , and R_8 show LOS characteristics with the main direction of TX movement

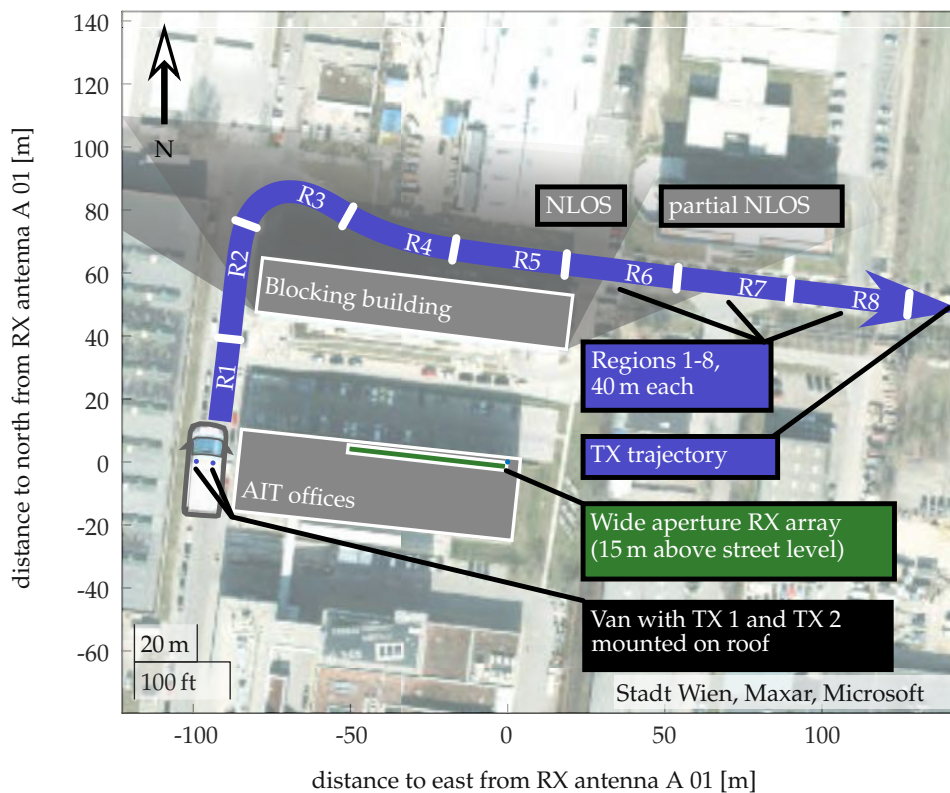


FIGURE 4.13: Top view of the urban scenario of the WIDE measurement campaign. The TX trajectory is divided into regions R_1 to R_8 and indicated in blue. The RX antenna array is located on the roof of an office building and indicated in green. The individual RX antennas are facing a large office building to the north, dividing the TX trajectory into LOS and NLOS regions.

parallel to the RX antenna array. The region where the blocking building causes NLOS conditions and the transition to LOS is indicated as a gray shade in Fig. 4.13.

Three different linear horizontal RX array configurations are implemented, with significant variation in the array aperture and antenna element spacing. Figure 4.14 shows in green the position where all three array configurations are located. As a reference point, the easternmost antenna (A 01) stayed on the same position throughout all measurements. The white elements in the green bars at the top of Fig. 4.14 indicate the individual position and spacing of antenna elements for the three array configurations (not to scale) and will serve as reference and visualization aid throughout the remainder of this thesis. The exact positioning and spacing of the patch antenna elements for each RX array configuration is detailed in Fig. 3.7. Photos of the three different RX antenna array setups on top of the AIT office building are shown in Fig. 4.15.

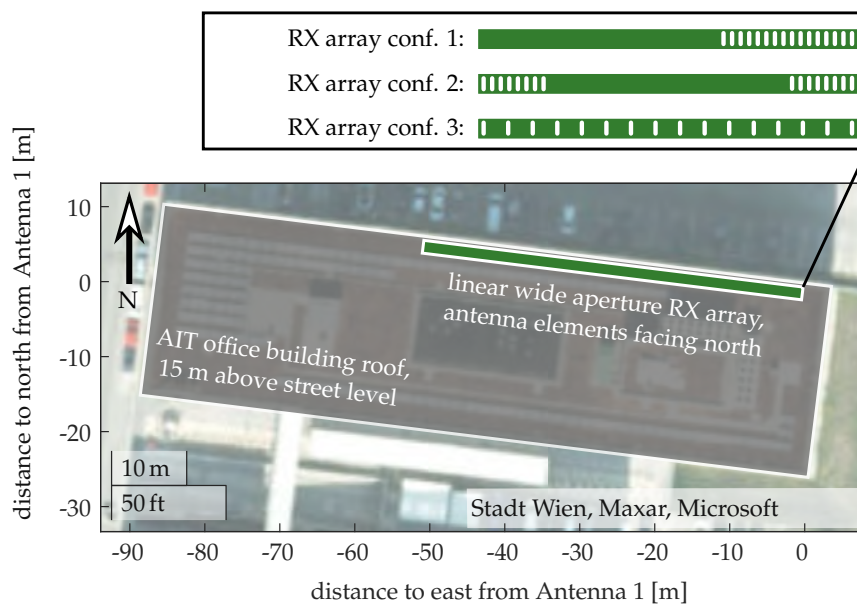


FIGURE 4.14: Top view of the roof where three different RX array configurations are realized. The white elements in the green bars at the top indicate the individual position and spacing of antenna elements for the three array configurations.

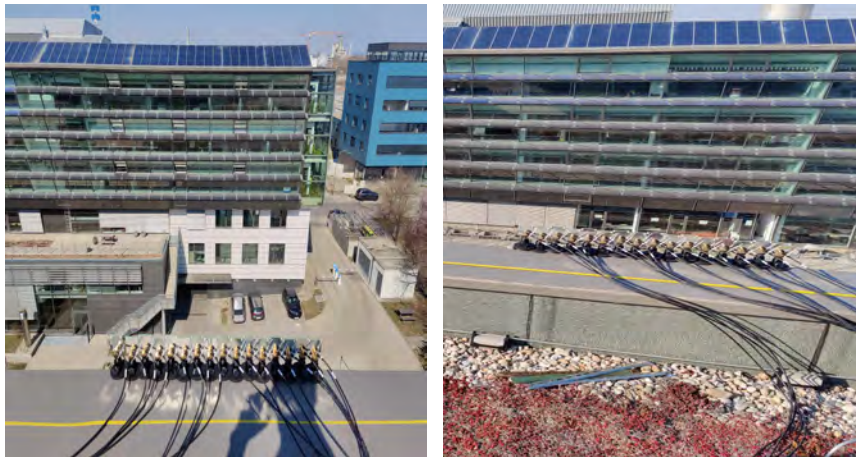
The parameters of the channel sounding framework utilized for the WIDE measurement campaign are listed in Table 4.2. For each RX array configuration, 10 runs on the same TX trajectory with similar velocities are performed. One measurement run lasts 30 s, in which a distance of around 300 m (divided in eight regions) is covered.

4.3.2 Single Antenna Results

In this section, we analyze the data gathered as described above with the methods outlined in Section 3.3.3. We seek knowledge of the characteristics of each channel from TX 1 to RX antenna a , and their relation and correlation to each other. Although ten measurement runs were obtained for each RX array configuration, the results of only one run per configuration are presented for the ease of exposition. Including more measurement runs has been analyzed and did not show significant differences in the presented results.



(a) WIDE measurement campaign, RX conf. 1.



(b) WIDE measurement campaign, RX conf. 2.



(c) WIDE measurement campaign, RX conf. 3.

FIGURE 4.15: WIDE measurement campaign, RX configurations.

TABLE 4.2: Measurement parameters and their respective values for the WIDE measurement campaign.

Parameter	Value
carrier frequency f_c	3.2 GHz
number of tones Q	481
tone spacing Δf	240 kHz
bandwidth B	115.44 MHz
repetition rate $T^{(\text{rep})}$	1 ms
max. resolvable Doppler frequency	500 Hz
max. resolvable velocity	150 km/h
TX power	38 dBm
measurement time per run	30 s
runs per RX conf.	10
TX distance traveled	300 m
RX array aperture	2 m (RX conf. 1), 46 m (RX conf. 2 and 3)

4.3.3 Average Received Power

We evaluate the average received power on each individual RX antenna from transmitter TX 1 for the three considered RX array configurations along the TX trajectory. Results are normalized to the maximum average received power as defined in (3.22), which occurred in region R_6 with RX conf. 1. The height of the 32 bars per region indicates $10 \log_{10} \bar{\mathcal{P}}_{1a}[s]$ and the color indicates the distance to RX antenna 01 for each antenna in the RX array. The average normalized received power over all RX antennas within a region $10 \log_{10} \frac{1}{A} \sum_{a=1}^A \bar{\mathcal{P}}_{1a}[s]$ is provided at the base of the bar plots for each region.

Figure 4.16 shows the average normalized received power $\bar{\mathcal{P}}_{1a}[s]$ for regions R_1 to R_8 and RX conf. 1. Since this configuration only has a small overall aperture size of approximately 2 m (see Fig. 3.7), all 32 RX antennas experience the same large-scale fading and $\bar{\mathcal{P}}_{1a}[s]$ is similar within each region. In the NLOS regions R_3 to R_5 , the average received power drops 15 - 20 dB compared to the strong LOS case in region R_6 .

In contrast to the previous result, Fig. 4.17 with RX conf. 2 shows significant differences in large-scale fading along the aperture of 46.5 m. It is obvious that in this case, the common assumption of wide-sense stationarity among RX antennas is no longer satisfied. The difference in average received power between the RX antenna groups (see also Fig. 3.7) is typically 7 - 8 dB (essentially the free space path-loss between RX antenna groups), but occasionally grows as large as 20 dB like in region R_6 . In this case, RX antennas 01-16 have direct LOS, whereas antennas 17-32 are still blocked by the large office building to the north of the RX array. Only in region R_4 with NLOS propagation conditions and approximately the same distance from the TX to all RX antennas the average received power stays on a similar level over the RX aperture.

Like before, RX conf. 3 shows strong non-stationarity over its aperture of 46.5 m as shown in Fig. 4.18. Again, the differences in average received power of 7 - 8 dB in regions R_1 to R_3 and R_5 is mostly explained with the different distance from the TX

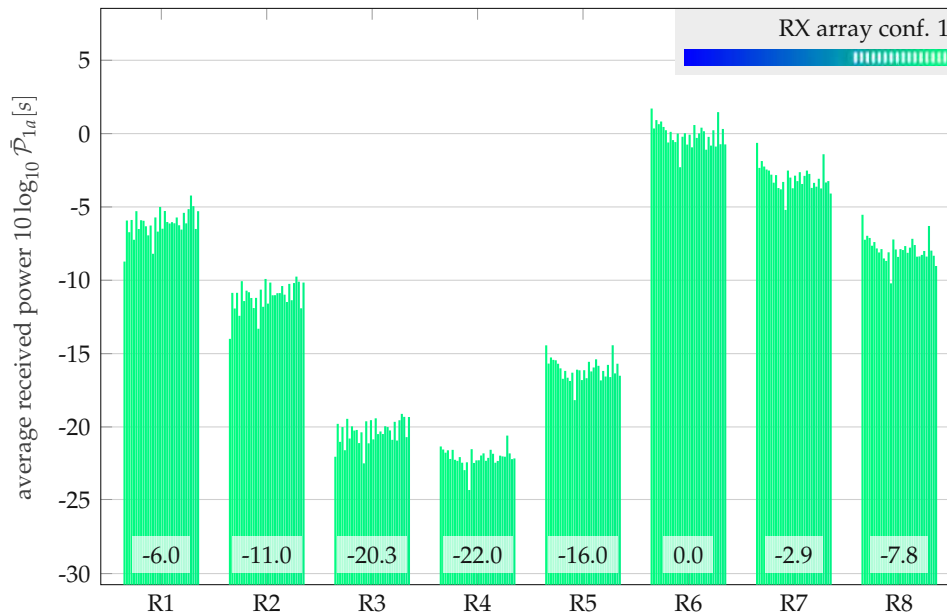


FIGURE 4.16: Average received power $\bar{P}_{1a} [s]$ for RX conf. 1 and regions R₁ to R₈. Each regions contains 32 bars for all RX antennas. The color coding shows the respective distance to RX antenna 01 as indicated in the top right corner.

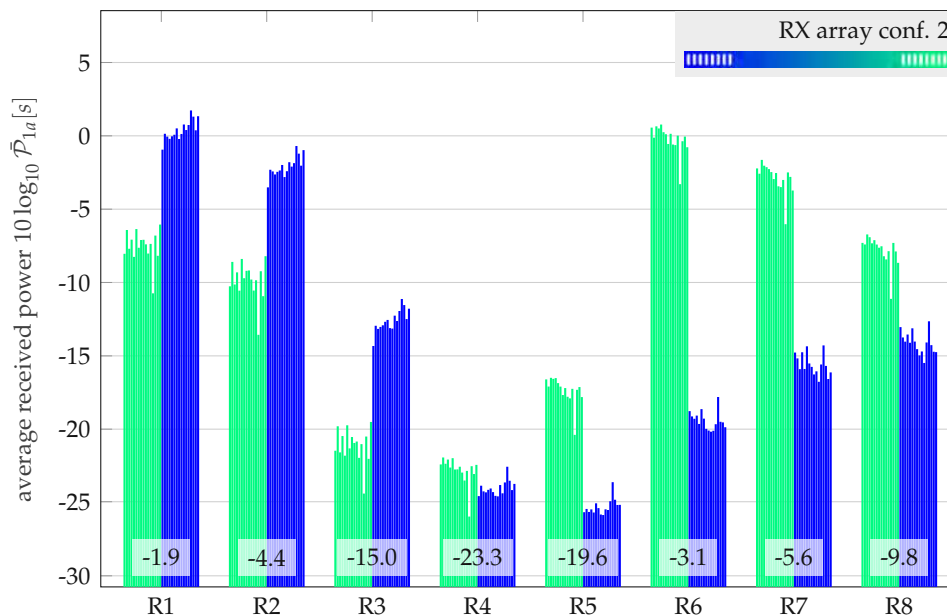


FIGURE 4.17: Average received power $\bar{P}_{1a} [s]$ for RX conf. 2 and regions R₁ to R₈. Each regions contains 32 bars for all RX antennas. The color coding shows the respective distance to RX antenna 01 as indicated in the top right corner.

to the individual RX antenna and the corresponding path-loss. Region R_6 shows the average received power with a variation of 20 dB among RX antennas due to a large building blocking parts of the array aperture.

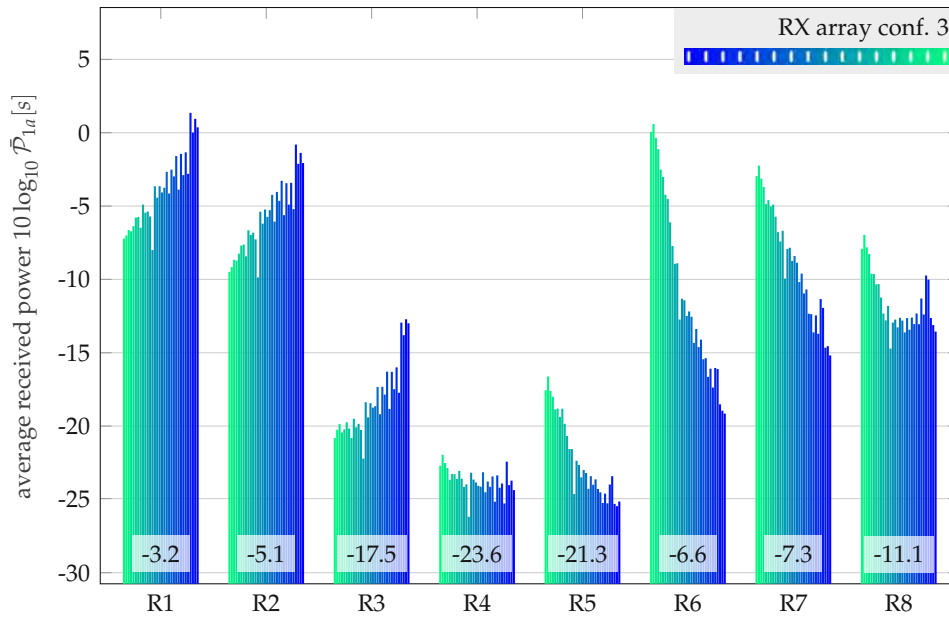


FIGURE 4.18: Average received power \bar{P}_{1a} [s] for RX conf. 3 and regions R_1 to R_8 . Each regions contains 32 bars for all RX antennas. The color coding shows the respective distance to RX antenna 01 as indicated in the top right corner.

4.3.4 Delay- and Doppler spreads

The large array apertures of RX conf. 2 and 3 (in relation to configuration 1) not only cause great variation in the average received power as seen in the previous section. Due to the TX operating in the near-field, the relative distances and velocities between TX and RX antennas vary greatly. To quantify this effect, we revert to the delay spread and Doppler spread as defined in (3.16) and (3.19), respectively.

A stationarity time of 256 ms for the LSF was assumed for the necessary calculations, i.e., $M = 256$. Comparative studies with a smaller stationarity time (i.e., 128 ms or 64 ms) did not show significant differences in the presented results but offer less resolution in the Doppler domain (see (3.10)).

Additionally, thresholds are applied to the delay and Doppler components of the LSF to reduce influence of measurement noise and limited dynamic range on the calculation of the spreads. The noise threshold is set to 3 dB and the sensitivity threshold is set to 45 dB [13].

Delay Spread - RX Array Configuration 1 Figure 4.19 shows the delay spreads $\zeta_{1a}^{(\tau)}$ [s] as defined in (3.16) of the $A = 32$ time-dependent channel transfer functions from TX 1 to the RX antennas in configuration 1. The time dependency is translated into space by plotting against the cumulative distance TX 1 traveled at each respective time instance. The color of each line indicates the distance of the respective antenna element to RX antenna 01 as indicated in the top right corner of the plot. The gray area between regions R_2 and R_6 indicates NLOS propagation conditions.

We notice that especially in the LOS regions R_1 , R_2 , and $R_6 - R_8$, the delay spread is very similar among RX antennas, which is not surprising given the proximity of the individual array elements. In the NLOS regions R_3 to R_5 it naturally rises in general due to the lack of a strong multipath component.

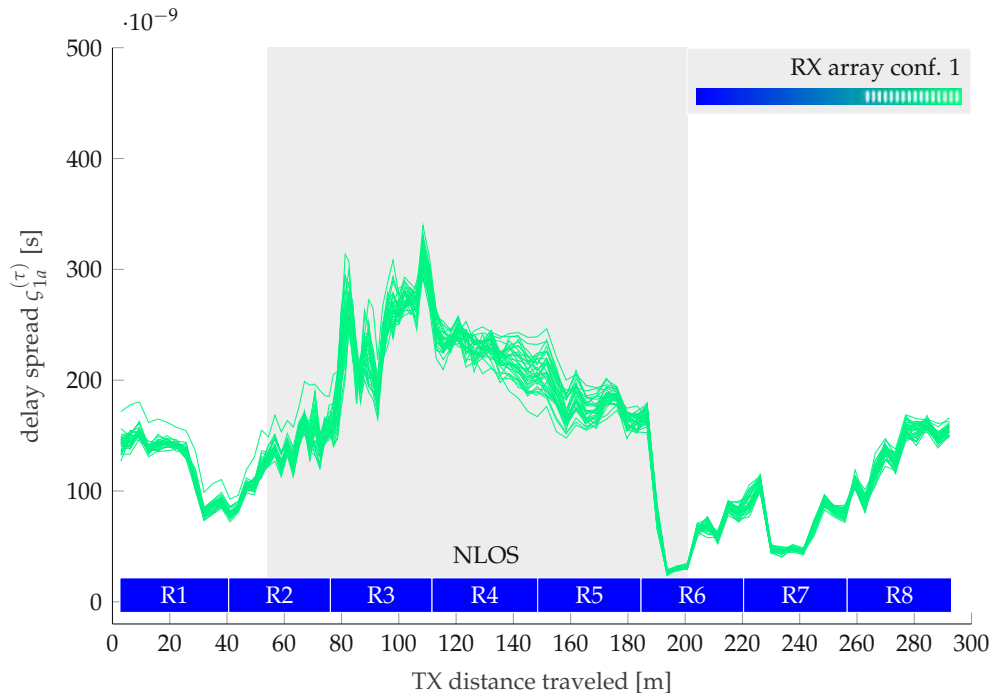


FIGURE 4.19: Delay spread $\varsigma_{1a}^{(\tau)}$ [s] of the $A = 32$ time-dependent channel transfer functions from TX 1 to the RX in configuration 1.

Delay Spread - RX Array Configuration 2 Figure 4.20 shows the delay spreads of the time-dependent channel transfer functions from TX 1 to the RX antennas in configuration 2. The edges of the NLOS region are indicated in light gray as only half of the RX antennas are blocked by the large office building. What is immediately obvious is the clustering of the delay spreads for RX antennas in the distributed arrays to the east and west, respectively. In regions R_1 to R_3 RX antennas 01-16 in the east are further from TX 1 than antennas 17-32, resulting in an increased delay spread. Regions R_6 to R_8 show this effect even more pronounced as the LOS to RX antennas 17-32 is still blocked, resulting in increased delay spreads, whereas antennas 1-16 are close to the TX trajectory and have LOS.

Delay Spread - RX Array Configuration 3 Figure 4.21 shows the delay spreads of the time-dependent channel transfer functions from TX 1 to the RX antennas in configuration 3. The edges of the NLOS region are fading out as the LOS to NLOS transition happens gradually over RX antennas. Like RX conf. 2, the range of occurring delay spreads for a given TX position varies widely compared to RX conf. 1. But given the uniform distribution of antenna elements, no clustering of delay spreads as in Fig. 4.20 is observed. Special emphasis is put on region R_6 , where we observe a sudden drop of the delay spread of 150 ns consecutively for the RX antennas. This effect is caused by TX 1 emerging from the blocking building and LOS propagation conditions occurring for one RX antenna after the other.

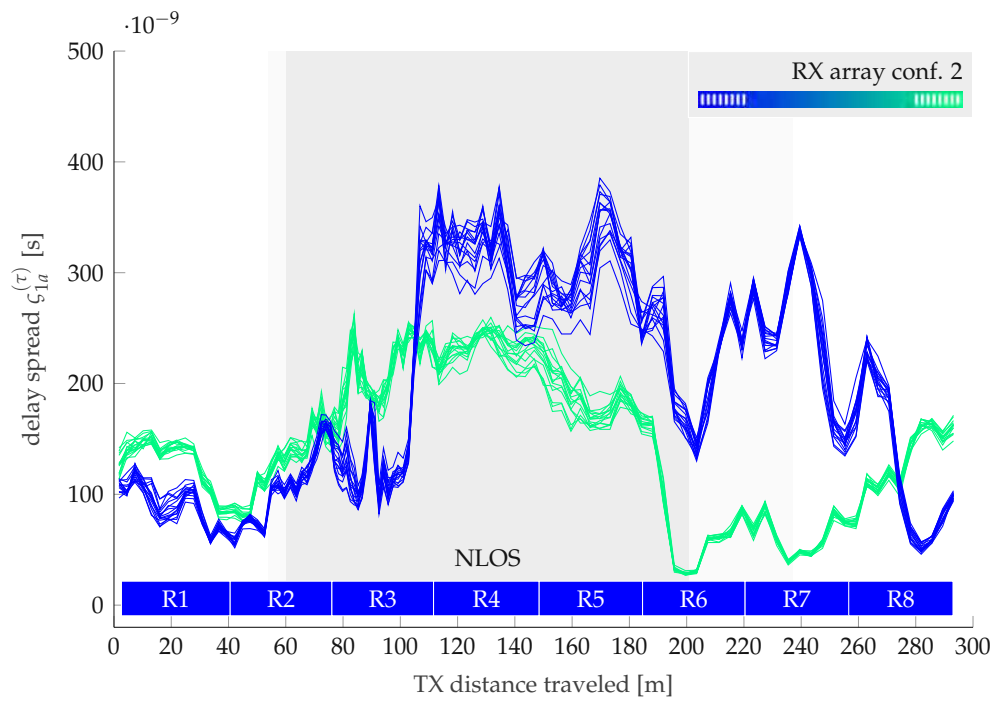


FIGURE 4.20: Delay spread $\zeta_{1a}^{(\tau)}$ [s] of the $A = 32$ time-dependent channel transfer functions from TX 1 to the RX in configuration 2.

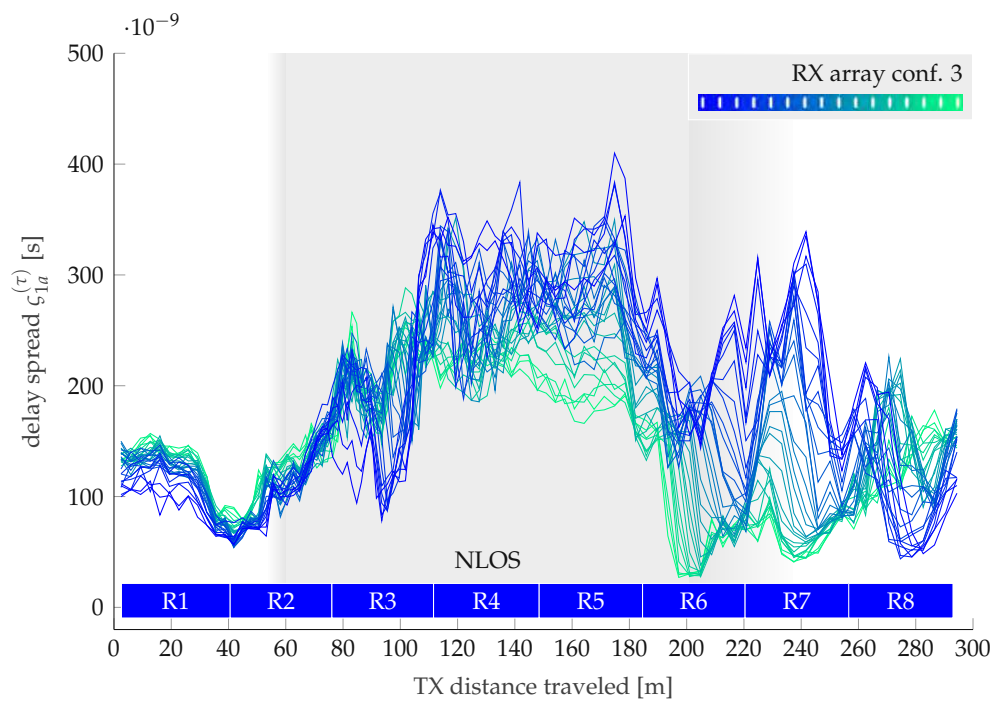


FIGURE 4.21: Delay spread $\zeta_{1a}^{(\tau)}$ [s] of the $A = 32$ time-dependent channel transfer functions from TX 1 to the RX in configuration 3.

TABLE 4.3: Maximum, minimum, and mean value of the RMS delay spread as well as its standard deviation around the mean within regions R_1 to R_8 for RX conf. 1 to 3.

Delay spread $\zeta_{1a}^{(\tau)}$ [s]	regions							
	R_1	R_2	R_3	R_4	R_5	R_6	R_7	R_8
RX array conf. 1								
Max. [ns]	181.8	213.4	344.9	317.2	251.4	179.5	133.9	193.4
Min. [ns]	72.2	72.2	120.2	164.6	93.8	22.8	37.2	78.8
Mean [ns]	119.0	133.1	230.2	229.6	178.2	72.6	73.5	138.7
Std. [ns]	5.1	9.1	14.0	11.3	11.0	5.3	3.6	6.1
RX array conf. 2								
Max. [ns]	161.9	194.3	380.3	381.6	388.1	318.5	342.2	245.3
Min. [ns]	51.7	51.7	77.9	174.8	147.6	25.8	35.4	45.1
Mean [ns]	106.4	119.7	183.9	271.9	239.7	148.3	153.2	129.5
Std. [ns]	21.3	14.0	43.1	45.7	60.9	79.8	96.0	42.2
RX array conf. 3								
Max. [ns]	159.1	199.9	383.6	390.8	410.8	315.7	342.1	231.0
Min. [ns]	54.0	53.4	76.8	177.3	132.4	25.8	37.5	38.0
Mean [ns]	113.4	114.9	199.3	264.2	253.9	141.0	134.3	130.8
Std. [ns]	11.7	11.7	33.7	39.2	44.8	57.2	67.5	36.2

Delay Spread - Summary Table 4.3 shows the quantitative analysis of the qualitative plots presented in Figs. 4.19 to 4.21. For each region R_1 to R_8 and each RX conf. 1 to 3, the maximum, minimum, mean, and standard deviation value of the delay spread over the 32 RX antenna realizations is provided.

We observe that the maximum, minimum, and mean delay spread values differ at most 20 ns for RX conf. 2 and 3, as their array aperture and position are identical (Fig. 4.14). The standard deviation, however, is consistently higher for the distributed massive MIMO setup in RX conf. 2. The standard deviation and therefore fluctuations in delay spread values among RX antennas for RX conf. 1 lies between 3 ns (LOS) and 14 ns (NLOS) and is in general significantly lower than the respective values for the RX conf. 2 and 3, given their significantly larger antenna apertures.

Doppler Spread - RX Array Configuration 1 Figure 4.21 shows the Doppler spread of the time-dependent channel transfer functions from TX 1 to the RX antennas in configuration 1. Like in the delay spread analysis, the time dependency is translated into space by plotting against the cumulative distance TX 1 traveled at each respective time instance. The color of each line indicates the distance of the respective antenna element to RX antenna 01 as indicated in the top right corner of the plot.

As with the delay spread, also the Doppler spread variation among RX antennas is small at maximally 10 Hz in the LOS regions R_1 , R_2 , and R_6 to R_8 . The Doppler spread generally increases in the NLOS regions R_3 to R_5 due to the lack of a strong LOS component. The relative velocity from TX 1 to the RX was low since the TX trajectory hardly showed radial components in these regions, see Fig. 4.13. However, Doppler spreads increase significantly in regions R_7 and R_8 since here the radial velocity component of the TX in relation to the RX increases.

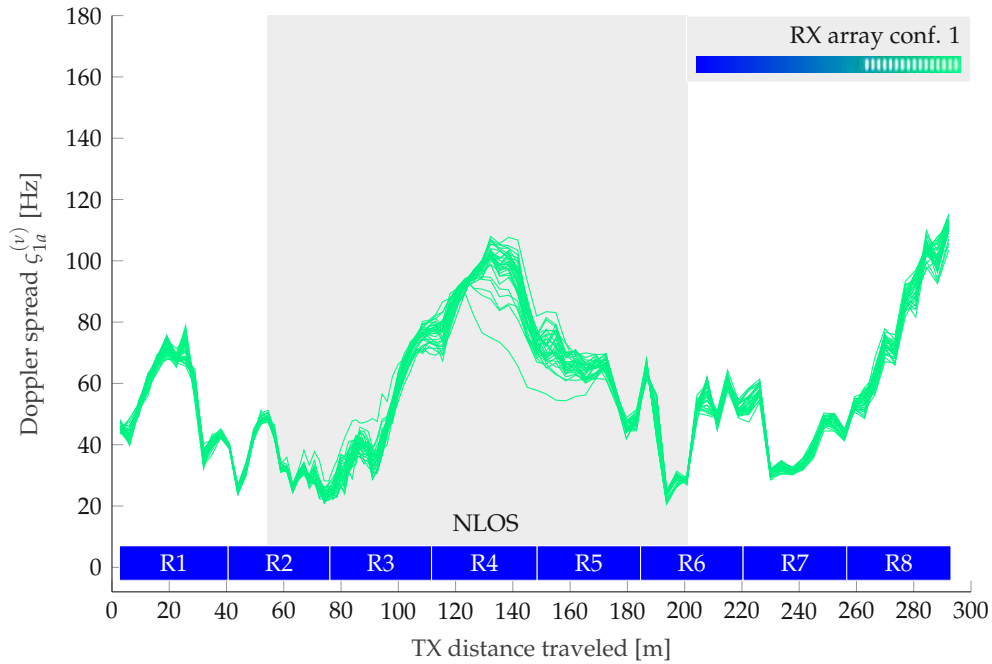


FIGURE 4.22: Doppler spread $\zeta_{1a}^{(v)}$ [s] of the $A = 32$ time-dependent channel transfer functions from TX 1 to the RX in configuration 1.

Doppler Spread - RX Array Configuration 2 Figure 4.21 shows the Doppler spread of the time-dependent channel transfer functions from TX 1 to the RX antennas in configuration 2. Clear clustering can be observed as RX antennas 01-16 experience propagation and large-scale fading conditions that are different from RX antennas 17-32. Within each distributed group, the Doppler spread is similar among RX antennas. Its value is largely determined by the absence of a LOS component for the respective antenna group (regions R_3 to R_5) and the relative velocity of the TX in respect to the antenna group (regions R_6 to R_8).

Doppler Spread - RX Array Configuration 3 Figure 4.21 shows the Doppler spread of the time-dependent channel transfer functions from TX 1 to the RX antennas in configuration 3. The minimum and maximum Doppler spread values along the trajectory of the user are, except for some outliers in region R_8 , similar. However, no clustering is observed. At each position in space along the TX trajectory, the Doppler spread values of the 32 RX antennas are distributed uniformly between their minimum and maximum values. Again, sudden drops (or increases) in the Doppler spread are observed consecutively over RX antennas (regions R_6 , R_7) as strong signal components appear (or disappear) for the respective antenna.

Doppler Spread - Summary Table 4.4 shows the quantitative analysis of the qualitative plots presented in Figs. 4.22 to 4.24. For each region R_1 to R_8 and each RX conf. 1 to 3, the maximum, minimum, mean, and standard deviation value of the Doppler spread over the 32 RX antenna realizations is provided.

Many findings from analyzing the delay spreads can readily be applied to the Doppler spreads. Maximum, minimum, and mean Doppler spread values are similar (within 8 Hz in regions R_1 to R_7) for RX conf. 2 and 3, as the array aperture and position are identical. Region R_8 , however, shows an increased maximum Doppler

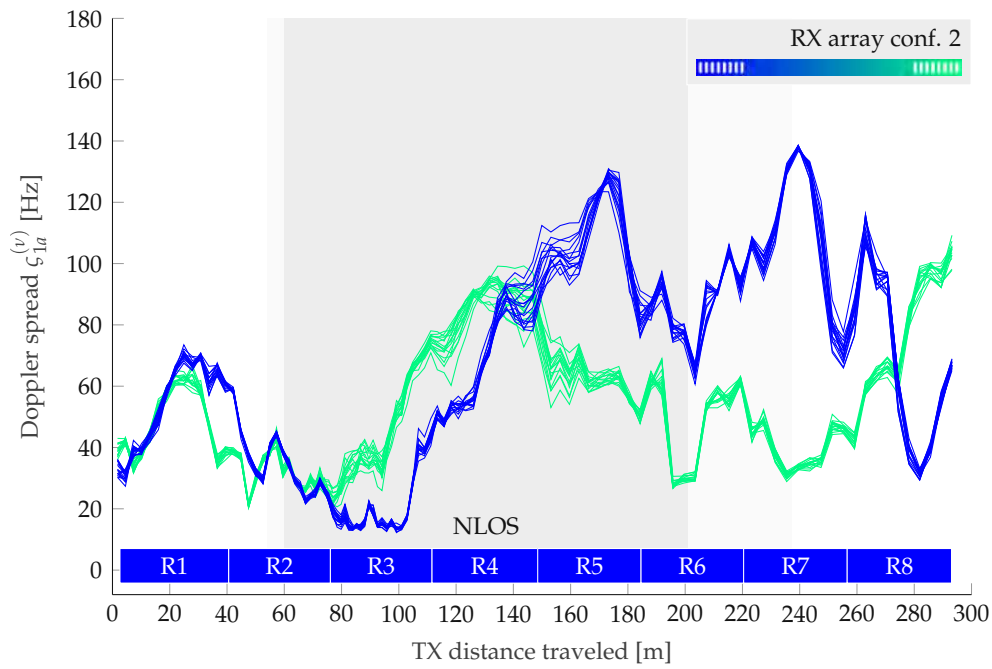


FIGURE 4.23: Doppler spread $\zeta_{1a}^{(v)}$ [s] of the $A = 32$ time-dependent channel transfer functions from TX 1 to the RX in configuration 2.

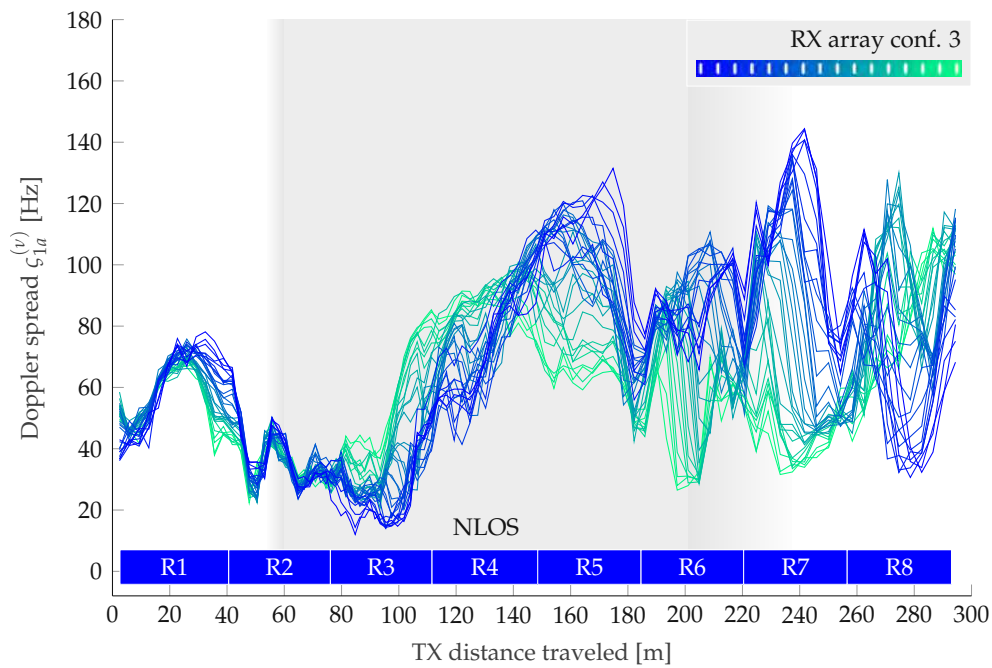


FIGURE 4.24: Doppler spread $\zeta_{1a}^{(v)}$ [s] of the $A = 32$ time-dependent channel transfer functions from TX 1 to the RX in configuration 3.

TABLE 4.4: Maximum, minimum and mean value of the RMS Doppler spread as well as its standard deviation around the mean within regions R_1 to R_8 for RX conf. 1 to 3.

Doppler spread $\zeta_{1a}^{(v)}$ [s]	regions							
	R_1	R_2	R_3	R_4	R_5	R_6	R_7	R_8
RX array conf. 1								
Max. [Hz]	79.6	54.0	85.5	109.8	84.6	74.1	69.2	125.4
Min. [Hz]	23.6	20.7	20.7	53.9	40.6	20.6	26.1	43.9
Mean [Hz]	53.0	32.9	44.9	87.2	62.7	47.6	42.6	84.2
Std. [Hz]	2.0	1.3	2.9	4.9	3.4	2.4	1.6	3.1
RX array conf. 2								
Max. [Hz]	74.5	63.3	78.7	113.5	133.1	117.3	138.8	116.8
Min. [Hz]	27.4	18.5	11.8	41.8	45.6	25.3	27.3	28.8
Mean [Hz]	52.0	32.6	32.5	76.9	84.2	69.2	73.6	75.0
Std. [Hz]	6.6	4.0	12.2	11.5	22.5	21.0	35.7	20.9
RX array conf. 3								
Max. [Hz]	78.8	68.7	85.3	116.1	132.8	120.4	145.6	131.2
Min. [Hz]	35.7	22.1	12.0	38.7	40.8	23.7	28.1	29.2
Mean [Hz]	58.9	36.2	36.0	80.6	86.7	75.5	74.8	82.6
Std. [Hz]	5.1	3.7	10.5	10.9	15.9	19.0	26.8	20.3

spread that is caused most probably by a blocking of some RX antennas by a large structure when the TX moves through.

The standard deviation is again and not surprisingly lowest for RX conf. 1. It is also consistently lower for the cell-free RX conf. 3 compared to the distributed configuration 2, a fact that has consequences on channel aging as detailed in Section 4.3.7.

4.3.5 Collinearity of the LSF in space

We evaluate the collinearity of the LSF in (3.23) to assess the stationarity of the three proposed RX conf. 1 to 3 in space, i.e., we analyze if the statistical parameters of the wireless propagation channel vary over RX antennas. A collinearity value close to one indicates a similar distribution of multipath components in the delay-Doppler domain, while a value close to zero indicates no similarity.

Collinearity Over Distance Traveled Figure 4.25 displays the collinearity $\alpha_{1aa'}[l]$ from RX antenna $a = 1$ to all other RX antennas $a' \in \{1, \dots, 32\}$ over the distance traveled by TX 1. Figure 4.25 (a) for RX conf. 1 shows high collinearity values $\alpha_{1aa'}[l]$ in general (0.8 – 1), but also exhibits regions of lower collinearity, e.g., in the NLOS regions between 100 m and 180 m traveled. Surprisingly, we do not see a monotonic decrease of collinearity with increasing RX antenna index a' (i.e., increasing distance between RX antennas a' and a). Especially after 200 m distance traveled, a repetitive pattern emerges with collinearity values of 0.9 and 0.6 alternating every two antennas. The reason for this is not yet clear and subject of further investigation.

Figure 4.25 (b) displays the collinearity $\alpha_{1aa'}[l]$ for RX conf. 2. The top half of the plot, representing the first RX antenna group, largely resembles the RX conf. 1 case.

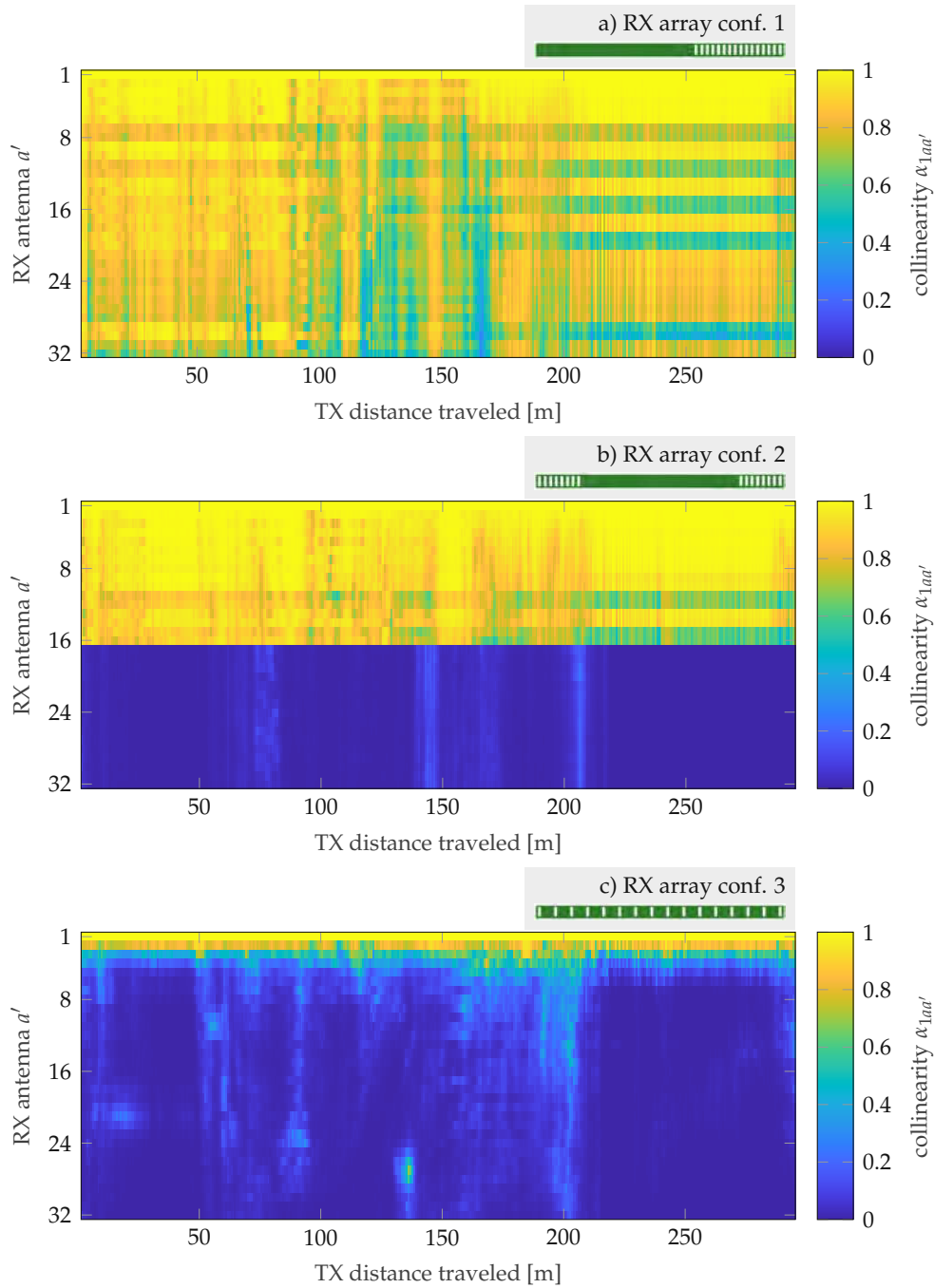


FIGURE 4.25: Spatial collinearity to RX antenna $a = 1$ over distance traveled on the users trajectory for (a) RX conf. 1, (b) RX conf. 2, and (c) RX conf. 3.

The bottom half of the plot, representing the RX antennas a' with a distance of at least 45 m to antenna $a = 1$, does not show any significant collinearity, as expected.

Figure 4.25 (c) displays the collinearity $\alpha_{1aa'}[l]$ for RX conf. 3. Already for the second RX antenna $a' = 2$, collinearity drops to 0.8 as the distance of 1.5 m = 16λ causes significant changes in the propagation environment. This effect is also confirmed in RX conf. 1 for RX antennas with similar distance. For RX antenna $a' = 3$ the collinearity drops further to 0.5. We conclude that for distances larger than 3 m = 32λ , non-stationarity in space must be assumed. Additionally, a distance significantly smaller than that (i.e., 0.3 m = 3.2λ) is no guarantee for stationarity in a rich scattering environment, as seen in Fig. 4.25 (a).

Average Collinearity Over All Regions We revert to the average collinearity over all regions R_1 to R_8 as defined in (3.25) to analyze collinearity between all RX antenna pairs (a, a') . This allows us to assess stationarity of antenna groups within the RX array in space.

Figure 4.26 (a) displays the average collinearity $\bar{\alpha}_{1aa'}[l]$ for RX conf. 1. Overall, collinearity of the involved LSFs is high at values between 0.9 and 1. However, RX antennas with indices $a \in \{7, 8, 11, 12, 15, 16, 19, 20, 29, 30\}$ apparently exhibit differing propagation characteristics as the complimentary RX antenna set and therefore low collinearity at 0.6 – 0.7, thus yielding the observed checkerboard pattern.

Figure 4.26 (b) displays the average collinearity $\bar{\alpha}_{1aa'}[l]$ for RX conf. 2. The observations from above are immediately applicable to each 16×16 block on the main diagonal, i.e., the distributed RX antenna array groups exhibit high collinearity within themselves, but not among them. Collinearity between any RX antenna in the east ($a \in \{1, \dots, 16\}$) and in the west ($a \in \{17, \dots, 32\}$) is negligible.

Figure 4.26 (c) displays the average collinearity $\bar{\alpha}_{1aa'}[l]$ for RX conf. 3. In this configuration, the distance between consecutive RX antennas is 1.5 m and therefore the collinearity decreases rapidly, i.e., to 0.8 for $|a' - a| = 1$ and to 0.5 for $|a' - a| = 2$. We conclude that there is no antenna pair (a, a') for which stationarity holds if their distance is larger than 3 m = 32λ .

4.3.6 Key Findings

Summarizing the single antenna results of the WIDE measurement campaign, we note the following.

- Large-scale fading and shadowing cause path-loss differences of up to 20 dB over horizontal linear RX array apertures that are 46.5 m in size for the scenario under investigation.
- The delay and Doppler spread vary greatly, up to 300 ns and 100 Hz respectively, over the aperture size for RX conf. 2 and 3.
- The standard deviation of the delay spread and the Doppler spread over RX antenna realizations is larger for RX conf. 2 than for configuration 3.
- Stationarity in space among RX antennas is likely for aperture sizes below 2 m = 21λ , but not guaranteed.
- Non-stationarity in space among RX antennas can be assumed for RX antenna distances greater than 3 m = 32λ .

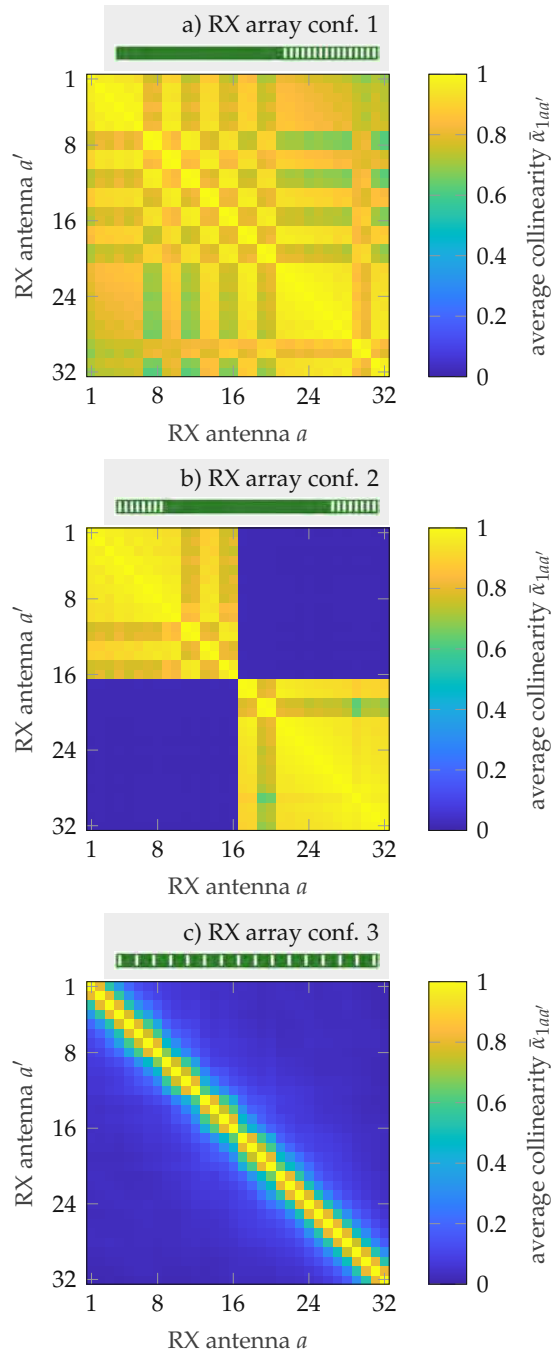


FIGURE 4.26: Average spatial collinearity over all regions for all RX antenna combinations (a, a') and for (a) RX conf. 1, (b) RX conf. 2, and (c) RX conf. 3.

4.3.7 Massive MIMO Processing and Results

The unmatched spectral efficiency of massive MIMO systems [4] arises due to K users (UEs) being served by a large number of BS antennas $A \gg K$ in favorable propagation conditions within a rich scattering environment.

A common step to simplify analysis in literature is to assume the matrix describing the wireless channel to be composed of independent and identically distributed (i.i.d.) channel realizations for the BS antennas a . With the growing array aperture size of distributed massive MIMO and cell-free systems, and the resulting variation in large-scale fading, shadowing, and relative velocities over BS antennas as shown in the previous section, this assumption no longer holds. It is therefore not sufficiently known in the community if the linear processing algorithms commonly utilized in massive MIMO maintain their close-to-optimal performance in widely distributed and cell-free systems.

In the following, we utilize the wireless channel measurements described above and the processing steps detailed in Section 3.3.5 to derive a massive MIMO signal model with channel matrix realizations deduced from real-world propagation scenarios. These channel matrices obtain their characteristics solely from the geometric relation between TX and RX and all the scattering and blocking objects in their surroundings as shown in Fig. 4.13. No statistical or other modeling assumptions for the channel matrix are made. The measurement SNR is greater than 25 dB at all times, i.e., $\tilde{\mathbf{H}}_m^H \tilde{\mathbf{H}}_m + \frac{\sigma_n^2}{P} \mathbf{I}_K \approx \tilde{\mathbf{H}}_m^H \tilde{\mathbf{H}}_m$ holds in (3.35) and the regularization term is therefore omitted when evaluating the results in what follows. Simulation results (not shown) confirm this approach, as the maximum difference in median SINR utilizing either RZF beam-forming in (3.35) or ZF beam-forming in (3.36) is found to be below 0.3 dB throughout all scenarios.

In this context, we again use the terms UE and BS instead of TX and RX, respectively, to highlight the usage of the obtained wireless propagation channel measurements in a widely distributed massive MIMO context. The measured channel transfer function realizations are directly interpreted as channel vector realizations as defined in (3.28). Since the number of supported RX antennas is limited to 32 by the measurement framework, no analysis with an increased number of antennas is presented.

SINR and Channel Aging Results The instantaneous SINR (3.33) determines achievable rates for the respective user k at a given time instant m . The signal component in the numerator and the interference component in the denominator heavily depend on the beam-forming applied at the BS, which in turn relies on timely CSI. We analyze the influence of aged CSI on the instantaneous SINR by calculating the beam-forming matrix (3.36) with outdated channel vectors $\tilde{\mathbf{h}}_{km}$ that are delayed by $\Delta t \in \{10 \mu\text{s}, 100 \mu\text{s}, 500 \mu\text{s}\}$.

The channel coefficients $\hat{h}_{ka}(mT_R + \Delta t)$ that were not measured directly are obtained by interpolating the preceding and subsequent measured channel transfer functions $\hat{h}_{ka}[m'] = \hat{h}_{ka}(m'T_R)$, $m' \in \{m-2, m-1, m, m+1\}$ using a cubic spline interpolation [59], [60]. This approach works sufficiently well since the repetition rate of the channel sounding measurements $T_R = 1 \text{ ms}$ is high enough to periodically capture channel transfer function realizations while the users move maximally $1.7 \text{ cm} = 0.18\lambda$ at their maximum velocity of 60 km/h [37].

The average noise power to transmit power ratio $\frac{\sigma_n^2}{P}$ in (3.33) is chosen to be -112 dB in all simulations. With an average path-loss of -92 dB in BS conf. 1 over

all regions R_1 to R_8 , the average over the time-varying SNR in all regions without interference is 20 dB.

Figure 4.27 plots the empirical CDF of the SINR (3.33) for outdated channel matrices (vertically aligned) and different regions (horizontally aligned). To calculate the empirical CDF, all channel matrices obtained in a given region (in which the UEs move along their trajectory) are used to calculate (3.36) and in turn the SINR. Each subplot in Fig. 4.27 shows the three BS conf. 1 to 3 under consideration in this thesis. Regions R_1 and R_6 exhibit LOS propagation characteristics while region R_4 is purely NLOS, see Fig. 4.13.

In region R_1 and with low channel aging of $\Delta t = 10 \mu\text{s}$, BS conf. 3 shows the highest SINR values on average, and BS conf. 2 performs slightly worse. BS conf. 1, however, has a significant drawback since the average distance between BS antennas and UEs is highest in this configuration (the larger aperture of configuration 2 and 3 lead to BS antennas being closer to the UE trajectory). The SINR is on average 3 dB lower in this configuration.

When the delay between CSI acquisition and beam-forming increases to $\Delta t = 100 \mu\text{s}$, the BS array configuration most affected is BS conf. 2 which now only shows slightly higher average SINR values than configuration 1. BS conf. 1 and 3 largely maintain the distribution of the empirical CDF. For all three configurations, the effect of channel aging is already noticeable

For a delay between CSI acquisition and beam-forming of $\Delta t = 500 \mu\text{s}$, as depicted in Fig. 4.27 at the bottom left, the SINR drops significantly for all BS conf. 1 to 3. Specifically, the median SINR value over the region R_1 drops by 4 dB in configuration 1, 8 dB in configuration 2, and 6 dB in configuration 3, compared to hardly any channel aging (at a CSI delay of $10 \mu\text{s}$).

The comparatively small effects of channel aging in region R_1 on BS conf. 1 is explained by the small relative velocity of the UEs in relation to the BS. Both configuration 2 and 3 feature BS antennas which are closer to the UE trajectory, but therefore also exhibit larger Doppler spreads, see also Fig. 4.23.

In region R_4 with NLOS propagation conditions, depicted in the center column of Fig. 4.27, channel aging has only very limited effect on the empirical CDF of the SINR. The median drops by at most 1 dB for all BS array configurations, comparing $\tilde{\mathbf{h}}_{km}$ aged $10 \mu\text{s}$ and $500 \mu\text{s}$, respectively. Again, BS conf. 3 shows the least sensitivity to channel aging.

In region R_6 , the right-most column in Fig. 4.27, BS conf. 1 shows the clear advantage of having all BS antennas close to the current position of the UEs and in direct LOS, whereas for both configuration 2 and 3 a considerable amount of antennas are still blocked by a large office building. Therefore, both large aperture configurations 2 and 3 give a similar SINR distribution that is in general shifted to lower values when compared to BS conf. 1. However, also in region R_6 BS conf. 3 is less influenced by channel aging of $\Delta t = 500 \mu\text{s}$, with its median SINR value dropping only 5 dB as compared to 8 dB and 6 dB of configuration 1 and 2, respectively.

Channel Hardening Results An evaluation of the channel hardening coefficient (3.40) distribution in regions R_1 (LOS), R_4 (NLOS), and R_6 (LOS) is shown in Fig. 4.28. It is immediately evident that channel hardening, i.e., the random fluctuations of the signal component $|\gamma_{km}|^2$ in (3.39), is lowest for the BS conf. 3 in all regions. This leads to the conclusion that if deterministic signal levels are desired, widely distributed configurations improve on the channel hardening capabilities of conventional massive MIMO systems.

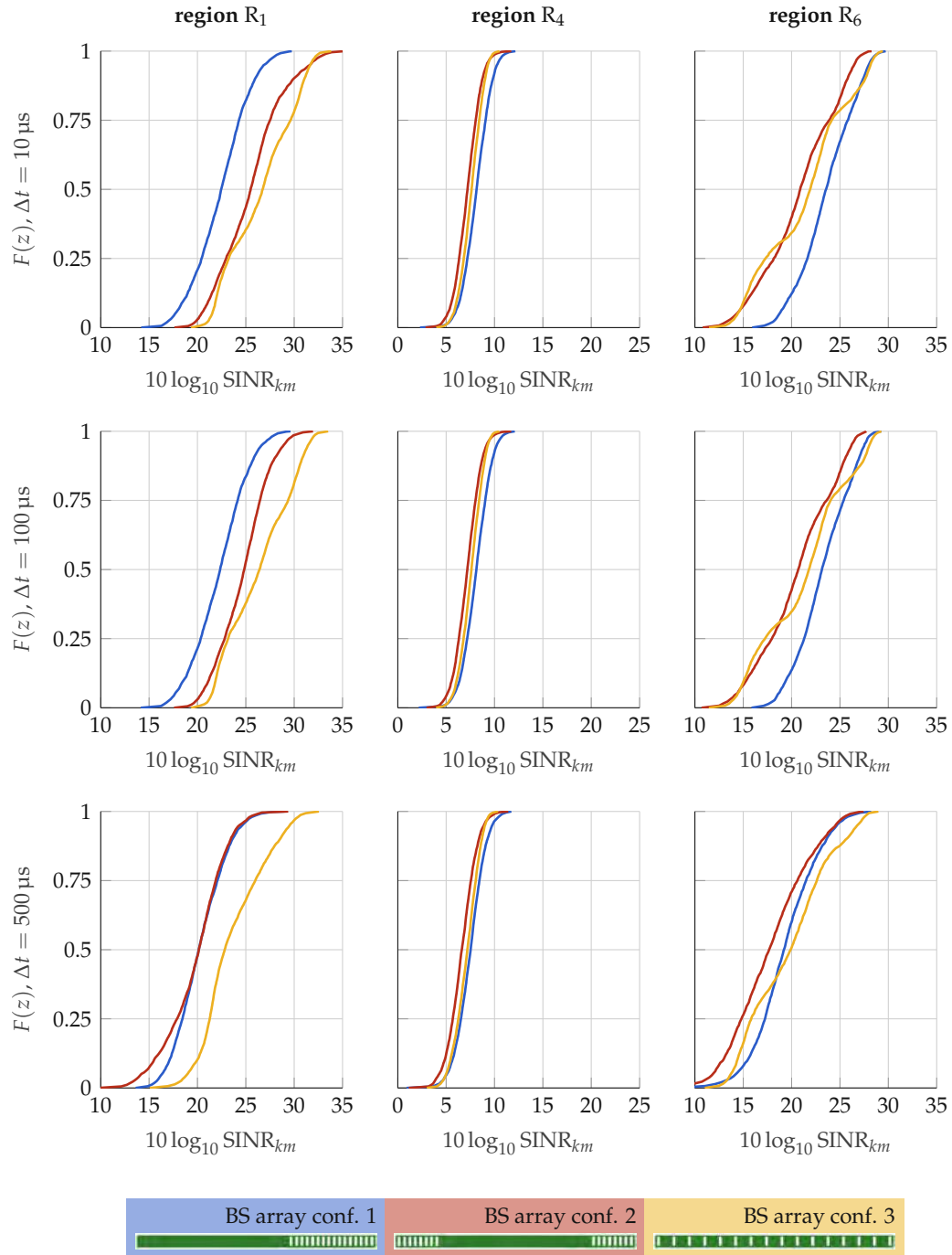


FIGURE 4.27: Empirical CDF of the SINR for regions R_1 (left), R_4 (middle) and R_6 (right), BS conf. 1 to 3, and channel matrices $\tilde{\mathbf{H}}_m$ aged $\Delta t = 10 \mu\text{s}$ (top), $\Delta t = 100 \mu\text{s}$ (middle), and $\Delta t = 500 \mu\text{s}$ (bottom).

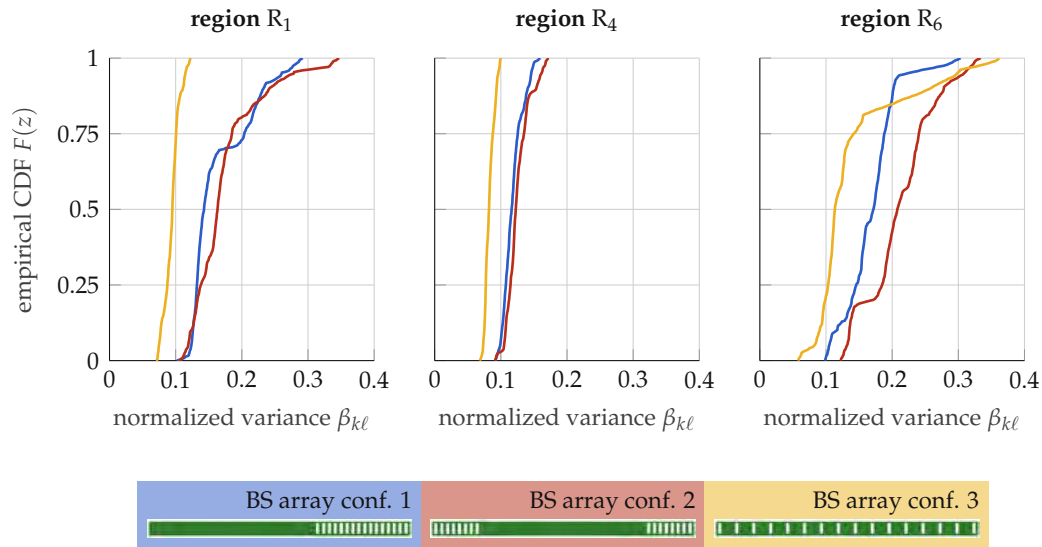


FIGURE 4.28: Empirical CDF of the channel hardening coefficient β_{kl} (normalized variance of the effective channel gain γ_{km}) for regions R_1 , R_4 and R_6 , and BS conf. 1 to 3.

4.3.8 Key Findings

Summarizing the massive MIMO processing result section, we note the following.

- Widely distributed systems are less susceptible to channel aging than distributed or conventional massive MIMO systems as presented in Fig. 4.27. The exact reason behind this phenomenon is still under investigation, but we suspect that the wide range of relative velocities of the UE in relation to the BS antennas (see the Doppler spreads in Fig. 4.21) mitigates channel aging to some extent.
- Widely distributed systems offer better channel hardening capabilities in the considered scenario than distributed or conventional massive MIMO systems as presented in Fig. 4.28 due to the great variation in multipath distribution over BS antennas (see also Fig. 4.26).

Chapter 5

Concluding Remarks

5.1 Conclusion and Discussion

We conclude this thesis with a discussion on the research objectives as introduced in Chapter 1, and if and to what extent they were met.

O1 was to assess the impact of CSI prediction on the reliability of widely distributed massive MIMO communications systems in high mobility scenarios. To accomplish this, we did the following:

- We analyzed the achievable SE in an uplink massive MIMO system with a general temporal covariance matrix for various values of the prediction horizon $\ell \geq 1$, the number of pilot symbols N , the SNR P/σ_n^2 , and BS antennas A .
- We found that CSI prediction considerably improved the achievable SE in all considered cases and parameter sets. Utilizing four instead of one pilot symbol was shown to double the SE, both for MRC and RZF. Utilizing more than four pilots showed no clear advantages. Moreover, we showed that utilizing a large number of pilot symbols leads to a reduction of the achievable block SE due to the large pilot overhead, which cannot be compensated by the improved CSI prediction.
- We showed that channel hardening, i.e., the capability of a massive MIMO system to eliminate small-scale fading and create quasi-deterministic effective channel gains, is (largely) independent of channel aging.
- Link-level simulations showed polynomial and Wiener CSI prediction significantly improved (> 5 dB) BER performance of our system in time-varying scenarios compared to constant or linear prediction.

O2 was to utilize time-frequency diversity through OP and spatial diversity through widely distributed BS antennas to increase the reliability of massive MIMO systems. This objective was met in the following manner:

- Utilization of OP in combination with CSI prediction decreased the BER and enabled approaching the performance of the system with perfect channel knowledge to within 2 dB (1 dB) for polynomial (Wiener) prediction for a velocity of 160 km/h. We showed that there is a trade-off between increased time-frequency diversity utilization and decreased predicted CSI quality for an increasing block length.
- We showed with empirical data that widely distributed systems are less susceptible to channel aging than distributed or conventional massive MIMO systems.

We suspect that the wide range of relative velocities of the UE in relation to the BS antennas mitigate channel aging to some extent, but further investigations are necessary.

- We showed with empirical data that widely distributed systems offer better channel hardening capabilities in the considered measurement scenario than distributed or conventional massive MIMO systems due to the great variation in multipath distribution over BS antennas.

O3 was to devise suitable measurement campaigns and gather empirical data to analyze the statistical properties of widely distributed massive MIMO systems and confirm the assumptions and results in **O1** and **O2**. We achieved the following:

- We devised and implemented the hardware, software, and processing stack to enable fully parallel and coherent channel sounding of two users and 32 BS antennas in high mobility scenarios with widely distributed BS antennas. The maximum supported speed of the users at a carrier frequency $f_c = 3.5$ GHz is 42 m/s. The maximum aperture of the BS antenna array is 90 m. To the best of our knowledge, this is currently a globally unique capability.
- We analyzed the statistical characteristics of the obtained CIRs in terms of envelope distribution, received power, delay spread, Doppler spread, and LSF collinearity. We showed that the assumption of i.i.d. Rayleigh distributed entries of the channel matrix common in massive MIMO literature does not hold for distributed or widely distributed systems. Further, we assume that the wide range of observed Doppler values along the widely distributed BS array helps mitigating the effects of channel aging.

Summarizing the points above, we conclude that we identified and verified, both empirically and analytically, several approaches to increase reliability of massive MIMO systems in high mobility environments. All the approaches under investigation in this thesis act on different aspects of a communication system and can therefore be combined as seen fit for the application at hand.

CSI prediction aims at improving the beam-forming quality of the system by intrinsically accounting for and anticipating the mobility of the users. OP does not compensate for channel aging, but rather mitigates its effect by spreading information bits over time and frequency. Widely distributed BS antenna arrays, on the contrary, suffer from less channel aging as there is a high probability that a subset of BS antennas experiences only low Doppler shifts due to the small relative velocity of the user to it.

5.2 Outlook

Similar to massive MIMO in current 5G deployment roll-outs, widely distributed massive MIMO is anticipated to serve as enabling technology for mobile communication systems of the sixth generation (6G) and cell-free systems [33]. A significant amount of research is still necessary to bring this technology to market [61], some of which closely related to the contents of this thesis. The following will provide a non-exhaustive overview of promising next steps in research which could benefit from results of this work.

Channel Modeling In the process of designing, simulating, and testing novel wireless communication systems, accurate and realistic channel models are of paramount importance. As widely distributed massive MIMO heavily relies on spatial diversity in the physical propagation environment, this characteristic must be captured and reproduced correctly by the utilized channel model. Their development and parametrization hinges on measurements and data acquisition frameworks to empirically validate the required accuracy. Many more widely distributed massive MIMO channel sounding campaigns in a large variety of settings (industrial, automotive, railway etc.), carrier frequencies, and BS antenna array configurations are necessary to obtain channel models for all scenarios targeted by 6G and its applications. Moreover, with the current push for *digital twins* in many industrial processes and the growing importance of wireless communications therein, realistic reproductions of wireless propagation as part of the complete simulation workflow becomes increasingly indispensable.

Implementations and Testbeds 6G is still in the early stages of development and standardization. There is not yet a clear picture on which candidate technologies will provide its anticipated capabilities, nor to which degree theoretical and simulated approaches prove themselves in a deployed system. Testbeds accomplish this task by implementing promising approaches in hardware and by verifying technology in the field. However, a significant amount of research and engineering work is still required, e.g., for implementing CSI prediction capabilities on field-programmable gate array (FPGA) hardware in computationally efficient ways; or for increasing the number of supported RF chains. Moreover, widely distributed massive MIMO testbeds should provide enough flexibility to allow for rapid prototyping development cycles of both hardware and software modules, e.g., by utilization of SDRs.

Tighter Integration of Photonic Components into Mobile Radio Systems Given the possibly large distances between BS antennas in widely distributed massive MIMO systems, the exclusive utilization of coaxial cables in BS antennas arrays becomes unfeasible both from an energy efficiency and deployment complexity perspective. It has already been shown that photonic components with integrated beam-forming capabilities are promising candidates for fronthauling in mobile networks [62], [63]. This approach can be extended by replacing the coaxial cable based distribution network from BPU to BS antenna with a fully optical network, potentially combined with the ability to perform integrated beam-forming, and a simple fiber-to-RF interface at each BS antenna. This method offers a rich field of research with potentially huge benefits for widely distributed massive MIMO systems.

List of Figures

2.1	Receive combining matrix signal model for the massive MIMO uplink.	7
2.2	Exemplary temporal correlation coefficient $r_{h,\ell}$ and coherence time $T^{(\text{coh})}$.	8
2.3	Equivalent receive combining matrix signal model for two users. . . .	8
2.4	Ergodic and asymptotic achievable $SE_{k\ell}$ over prediction horizon ℓ for a normalized Doppler $f_D T_s = 0.04$, an SNR $\frac{P}{\sigma_n^2} = 12$ dB, and MRC beam-forming.	15
2.5	$SE_{k\ell}$ over prediction horizon ℓ for a normalized Doppler $f_D T_s = 0.04$ and RZF beam-forming.	15
2.6	Boxplot of the channel hardening coefficient $\beta_{k\ell}$ (normalized variance of effective channel gain) distribution over prediction horizon $\ell \in \{0, \dots, 30\}$ for different number of BS antennas, $A \in [8, 128]$	16
2.7	$SE_{k\ell}$ over prediction horizon ℓ for a normalized Doppler $f_D T_s = 0.04$ and RZF beam-forming.	16
2.8	$SE_{k\ell}$ over prediction horizon ℓ for a normalized Doppler $f_D T_s = 0.04$ and RZF beam-forming.	17
2.9	SE_{kMN} for block length M , a normalized Doppler $f_D T_s = 0.04$, and RZF beam-forming.	18
2.10	Assumed slot structure with the uplink (UL) SRS symbol indices $m \in \{-4, -3, -2, -1\}$	20
2.11	Relative MSE for block length M , a velocity of 70 km/h, and a carrier frequency of 3.5 GHz in a simulated Rayleigh channel.	24
2.12	Relative MSE over the block length M in time for a velocity of 60 km/h at 3.5 GHz for empirical channel data from vehicular measurements.	24
2.13	Bar plot of the simulated BER for a massive MIMO system employing CSI prediction without precoding, given various velocity and SNR combinations. The number of BS antennas is $A = 64$	26
2.14	Simulated BER for a massive MIMO system employing the considered prediction methods without precoding and with DSFT precoding.	27
2.15	Simulated BER over block length M in time for $A = 64$ BS antennas, a velocity of 160 km/h and $E_b/N_0 = 6$ dB.	27
2.16	Simulated BER over block length M and number of BS antennas A for a velocity of 160 km/h.	28
3.1	Block diagram of the massive MIMO channel sounder TX. The transmitter consists of one USRP connected to two antennas (TX 1, TX 2) and supplemented with external PAs.	32
3.2	Block diagram of the massive MIMO channel sounder RX.	34
3.3	Side view and front view of the rectangular RX air-gaped patch antenna array.	35
3.4	S11 parameter for both an RX antenna element in the center of the array as well as on the edge.	35

3.5	Modular patch antenna array element on ball head tripod with magnetic mount and dimensions.	36
3.6	S11 parameter for an individual RX antenna array element, both with and without adjacent antennas.	37
3.7	Channel measurement framework consisting of a central BPU for data aggregation and storage (bottom), two DUs for up- and down conversion, and 32 antennas assembled in one of three RX array configurations (top).	38
3.8	Schematic and fully assembled view of the massive MIMO calibration unit.	39
3.9	Signal processing chain of the channel sounder.	43
3.10	RT 3D model including buildings (gray), vegetation (green) and metallic structures (blue) derived from openly available building data bases.	44
4.1	DIST measurement campaign, collocated (top) and distributed (bottom) RX setup.	55
4.2	DIST measurement campaign, TX antenna setup on the van roof.	56
4.3	Top view of the urban scenario of the DIST measurement campaign in Vienna.	57
4.4	Comparison of measured and simulated PDP over distance traveled by the TX.	59
4.5	Comparison of measured and simulated DSD over distance traveled by the TX.	60
4.6	Box plot of the GoF for several probability distributions.	62
4.7	SVS for one run with the BS antennas collocated (top) and distributed (bottom).	63
4.8	Empirical CDF of the SVS over 10 runs with the distributed setup and 10 runs with the collocated setup.	64
4.9	Rician K-factor $\kappa(\mathcal{G})$ (top) and SVS $\xi(\mathbf{H}_m)$ (bottom) over UE position from measured data for the distributed BS setup.	65
4.10	Rician K-factor $\kappa(\mathcal{G})$ (top) and SVS $\xi(\mathbf{H}_m)$ (bottom) over UE position from measured data for the collocated BS setup.	65
4.11	Ergodic achievable uplink sum SE over UE position for a mean SNR of 6 dB.	66
4.12	Empirical CDF of the ergodic achievable uplink sum SE for realizations over the UE trajectory from 6 measurement runs.	67
4.13	Top view of the urban scenario of the WIDE measurement campaign.	69
4.14	Top view of the roof where three different RX array configurations are realized.	70
4.15	WIDE measurement campaign, RX configurations.	71
4.16	Average received power $\bar{\mathcal{P}}_{1a}[s]$ for RX conf. 1 and regions R_1 to R_8	73
4.17	Average received power $\bar{\mathcal{P}}_{1a}[s]$ for RX conf. 2 and regions R_1 to R_8	73
4.18	Average received power $\bar{\mathcal{P}}_{1a}[s]$ for RX conf. 3 and regions R_1 to R_8	74
4.19	Delay spread $\zeta_{1a}^{(\tau)}[s]$ of the $A = 32$ time-dependent channel transfer functions from TX 1 to the RX in configuration 1.	75
4.20	Delay spread $\zeta_{1a}^{(\tau)}[s]$ of the $A = 32$ time-dependent channel transfer functions from TX 1 to the RX in configuration 2.	76
4.21	Delay spread $\zeta_{1a}^{(\tau)}[s]$ of the $A = 32$ time-dependent channel transfer functions from TX 1 to the RX in configuration 3.	76

4.22	Doppler spread $\zeta_{1a}^{(v)}$ [s] of the $A = 32$ time-dependent channel transfer functions from TX 1 to the RX in configuration 1.	78
4.23	Doppler spread $\zeta_{1a}^{(v)}$ [s] of the $A = 32$ time-dependent channel transfer functions from TX 1 to the RX in configuration 2.	79
4.24	Doppler spread $\zeta_{1a}^{(v)}$ [s] of the $A = 32$ time-dependent channel transfer functions from TX 1 to the RX in configuration 3.	79
4.25	Spatial collinearity to RX antenna $a = 1$ over distance traveled on the users trajectory for (a) RX conf. 1, (b) RX conf. 2, and (c) RX conf. 3. . .	81
4.26	Average spatial collinearity over all regions for all RX antenna combinations (a, a') and for (a) RX conf. 1, (b) RX conf. 2, and (c) RX conf. 3.	83
4.27	Empirical CDF of the SINR for regions R_1 (left), R_4 (middle) and R_6 (right), BS conf. 1 to 3, and channel matrices $\hat{\mathbf{H}}_m$ aged $\Delta t = 10 \mu\text{s}$ (top), $\Delta t = 100 \mu\text{s}$ (middle), and $\Delta t = 500 \mu\text{s}$ (bottom).	86
4.28	Empirical CDF of the channel hardening coefficient β_{kl} (normalized variance of the effective channel gain γ_{km}) for regions R_1 , R_4 and R_6 , and BS conf. 1 to 3.	87

List of Tables

4.1	Measurement parameters and their respective values for DIST measurement campaign.	56
4.2	Measurement parameters and their respective values for the WIDE measurement campaign.	72
4.3	Maximum, minimum, and mean value of the RMS delay spread as well as its standard deviation around the mean within regions R_1 to R_8 for RX conf. 1 to 3.	77
4.4	Maximum, minimum and mean value of the RMS Doppler spread as well as its standard deviation around the mean within regions R_1 to R_8 for RX conf. 1 to 3.	80

List of Abbreviations

A/D	analog to digital
BER	bit error rate
BPU	baseband processing unit
BS	base station
CDF	cumulative distribution function
CFR	channel frequency response
CIR	channel impulse response
CP	cyclic prefix
CSI	channel state information
DPS	discrete prolate spheroidal
DSD	Doppler spectral density
DSFT	discrete symplectic Fourier transform
DU	distributed unit
FFT	fast Fourier transform
FPGA	field-programmable gate array
GNSS	global navigation satellite system
GoF	goodness of fit
GSM	global system for mobile communications
i.i.d.	independent and identically distributed
IFFT	inverse fast Fourier transform
KS	Kolmogorov-Smirnov
LOS	line of sight
LS	least squares
LSF	local scattering function
LTE	long term evolution
MIMO	multiple input multiple output
ML	machine learning
MMSE	minimum mean square error
MRC	maximum ratio combining
MSE	mean squared error
NLOS	non-line of sight
NR	new radio

OFDM	orthogonal frequency-division multiplexing
OP	orthogonal precoding
PA	power amplifier
PAPR	peak-to-average power ratio
PDF	probability density function
PDP	power delay profile
PPS	pulse per second
PXI	PCI extensions for instrumentation
RF	radio frequency
RMS	root mean square
RT	ray tracing
RU	radio unit
RX	receiver
RZF	regularized zero-forcing
SDR	software-defined radio
SE	spectral efficiency
SINR	signal to interference and noise ratio
SNR	signal to noise ratio
SRS	sounding reference signal
SVS	singular value spread
TDD	time division duplex
TX	transmitter
UE	user equipment
UPS	uninterruptible power supply
USRP	universal software radio peripheral
UTD	uniform theory of diffraction
V2I	vehicle to infrastructure
WR	White Rabbit
ZF	zero-forcing
5G	fifth generation
6G	sixth generation

Notation and List of Symbols

Notation

A, a	scalar variable
$a \in \{1, \dots, A\}$	a is in the set of natural numbers from 1 to A
\mathbf{a}	\mathbf{a} is a vector
\mathbf{A}	\mathbf{A} is a matrix
$\mathbf{a} = \text{vec}(\mathbf{A})$	vectorization of matrix \mathbf{A} by stacking its columns into vector \mathbf{a}
$a = (\mathbf{A})_{ij}$	element of matrix \mathbf{A} in i -th row and j -th column
\mathbf{A}^T	transpose of matrix \mathbf{A}
\mathbf{A}^H	conjugate (Hermitian) transpose of matrix \mathbf{A}
\mathbf{A}^{-1}	inverse of matrix \mathbf{A}
$\mathbf{A} \in \mathbb{C}^{a \times b}$	complex matrix \mathbf{A} of dimension a times b
$\mathbf{a} \sim \mathcal{CN}(\mathbf{b}, \mathbf{B})$	random vector \mathbf{a} with complex Gaussian distribution, mean \mathbf{b} and covariance matrix \mathbf{B}
$\mathbb{E}\{\mathbf{A}\}$	elementwise expectation
$\text{Var}\{a\}$	variance of random variable a
$\text{tr}\{\mathbf{A}\}$	trace of matrix \mathbf{A}
$\mathbf{A} \otimes \mathbf{B}$	Kronecker product of matrices \mathbf{A} and \mathbf{B}
$\ \mathbf{A}\ _F$	Frobenius norm of matrix \mathbf{A}
\mathbf{I}_A	identity matrix of dimension A times A
$\mathbf{0}$	zero matrix/vector, $(\mathbf{0})_{ij} = 0, \forall i, j$

Symbols

a	RX or BS antenna index
A	number of RX or BS antennas
\mathbf{b}	information symbols
B	bandwidth
c	speed of light
C	capacity
\mathbf{C}	spreading matrix
\hat{C}_{ka}	estimate of LSF
d_k	distance between user and RX array
D	size of the linear RX array
f_c	carrier frequency
f_D	Doppler frequency
\hat{g}_{ka}	CIR
G_w	taper functions
\mathcal{G}	set for fitting CIR distributions
GoF	goodness of fit
h_{kam}	channel coefficient
\mathbf{h}_{km}	channel vector
\mathbf{H}_m	channel matrix

$\mathcal{H}_{ka}^{(G_w)}$	tapered frequency response
$I_{k\ell}$	instantaneous interference and noise power
k	TX antenna or users index
K	number of TX antennas or users
ℓ	prediction horizon
l	stationarity region index
L	length of stationarity region
m	time index
M	number of time samples
n	delay sample index
N	number of pilot symbols
\mathbf{n}_m	noise vector
p	Doppler shift index
P	signal power
$\hat{\mathcal{P}}_{ka}^{(\tau)}$	PDP
$\hat{\mathcal{P}}_{ka}^{(v)}$	DSD
q	subcarrier index
Q	number of subcarriers
r	propagation path index
R	number of propagation paths
$\mathbf{r}_{h,\ell}$	temporal correlation of the channel coefficient
\mathbf{R}_k	correlation matrix
s_{km}	transmitted (spreaded) information symbol
\mathbf{s}_m	transmitted (spreaded) information symbol vector
$S_{k\ell}$	instantaneous signal power
$\text{SE}_{k\ell}$	ergodic achievable SE
$T^{(\text{slot})}$	slot duration
$T^{(\text{symb})}$	symbol duration
$T^{(\text{rep})}$	repetition time
$T^{(\text{stat})}$	stationarity time
v	speed
$\mathbf{V}_{k\ell}$	Wiener predictor
w	second Rice distribution shape parameter, Rayleigh distribution shape parameter
\mathbf{w}_{km}	beam-forming vector
\mathbf{W}_m	beam-forming matrix
$x[n]$	transmit signal
$y_{ka}[m, n]$	received signal
\mathbf{y}_m	received signal vector
z	random variable
$\alpha_{kaa'}$	collinearity of LSF
$\beta_{k\ell}$	normalized variance of effective gain (channel hardening metric)
γ_{km}	effective gain
$\epsilon_{kN\ell}(\cdot, \cdot)$	MSE
ζ_{km}	singular value
$\eta_{k\ell}$	instantaneous SINR
$\Theta_{kN\ell}$	covariance matrix of the channel vector estimate
$\kappa(\mathcal{G})$	Rician K -factor
λ	wavelength
$\Lambda_k(m)$	Lagrange basis functions

ν	propagation path Doppler frequency
$\bar{\nu}_{ka}$	mean Doppler
ν	first Rice distribution shape parameter
$\xi(\cdot)$	singular value spread
σ^2	noise power
$\zeta_{ka}^{(\tau)}$	RMS delay spread
$\zeta_{ka}^{(\nu)}$	RMS Doppler spread
τ	propagation path delay
$\bar{\tau}_{ka}$	mean delay
χ	propagation path attenuation

Bibliography

- [1] C. Shannon, "Communication in the presence of noise", *Proceedings of the IRE*, vol. 37, no. 1, pp. 10–21, 1949. DOI: 10.1109/JRPROC.1949.232969.
- [2] E. Telatar, "Capacity of multi-antenna Gaussian channels", *European Transactions on Telecommunications*, vol. 10, no. 6, pp. 585–595, 1999.
- [3] A. F. Molisch, *Wireless Communications*, 2nd ed. John Wiley & Sons, 2011, ISBN: 9780470741870.
- [4] T. L. Marzetta, "Noncooperative cellular wireless with unlimited numbers of base station antennas", *IEEE Transactions on Wireless Communications*, vol. 9, no. 11, pp. 3590–3600, 2010, ISSN: 15361276. DOI: 10.1109/TWC.2010.092810.091092. arXiv: 1201.3210.
- [5] E. Björnson, J. Hoydis, and L. Sanguinetti, "Massive MIMO has unlimited capacity", *IEEE Transactions on Wireless Communications*, vol. 17, no. 1, pp. 574–590, 2017.
- [6] K. T. Truong and R. W. Heath, "Effects of channel aging in massive MIMO systems", *Journal of Communications and Networks*, vol. 15, no. 4, pp. 338–351, 2013, ISSN: 12292370. DOI: 10.1109/JCN.2013.000065. arXiv: 1305.6151.
- [7] D. Löschenbrand, M. Hofer, and T. Zemen, "Spectral efficiency of time-variant massive MIMO using Wiener prediction", *IEEE Communications Letters*, 2023. DOI: 10.1109/LCOMM.2023.3242457.
- [8] —, "Orthogonal precoding with channel prediction for high mobility massive MIMO", in *2020 IEEE 31st Annual International Symposium on Personal, Indoor and Mobile Radio Communications (PIMRC)*, 2020. DOI: 10.1109/PIMRC48278.2020.9217208.
- [9] D. Löschenbrand, M. Hofer, L. Bernadó; S. Zelenbaba, and T. Zemen, "Towards cell-free massive MIMO: A measurement-based analysis", *IEEE Access*, 2022. DOI: 10.1109/ACCESS.2022.3200365.
- [10] D. Löschenbrand, M. Hofer, L. Bernadó, G. Humer, B. Schrenk, S. Zelenbaba, and T. Zemen, "Distributed massive MIMO channel measurements in urban vehicular scenario", in *13th European Conference on Antennas and Propagation (EuCAP)*, Krakow, Poland, 2019.
- [11] D. Löschenbrand, M. Hofer, B. Rainer, and T. Zemen, "Empirical and simulated performance evaluation of distributed massive MIMO", in *Asilomar Conference on Signals, Systems, and Computers (ASILOMAR)*, 2019.
- [12] E. Björnson, J. Hoydis, and L. Sanguinetti, "Massive MIMO networks: Spectral, energy, and hardware efficiency", *Foundations and Trends® in Signal Processing*, vol. 11, no. 3-4, pp. 154–655, 2017, ISSN: 1932-8346. DOI: 10.1561/20000000093. [Online]. Available: <http://www.nowpublishers.com/article/Details/SIG-093>.

- [13] L. Bernadó, T. Zemen, F. Tufvesson, A. F. Molisch, and C. F. Mecklenbräuker, "Delay and Doppler spreads of nonstationary vehicular channels for safety-relevant scenarios", *IEEE Transactions on Vehicular Technology*, vol. 63, no. 1, pp. 82–93, Jan. 2014, ISSN: 0018-9545. DOI: 10.1109/TVT.2013.2271956. arXiv: arXiv:1305.3376v1.
- [14] C. Kong, C. Zhong, A. K. Papazafeiropoulos, M. Matthaiou, and Z. Zhang, "Sum-rate and power scaling of massive MIMO systems with channel aging", *IEEE Transactions on Communications*, vol. 63, no. 12, pp. 4879–4893, 2015, ISSN: 00906778. DOI: 10.1109/TCOMM.2015.2493998. arXiv: 1510.06827.
- [15] H. Q. Ngo and E. G. Larsson, "No downlink pilots are needed in TDD massive MIMO", *IEEE Transactions on Wireless Communications*, vol. 16, no. 5, pp. 2921–2935, 2017, ISSN: 15361276. DOI: 10.1109/TWC.2017.2672540. arXiv: 1606.02348.
- [16] S. Gunnarsson, J. Flordelis, L. Van der Perre, and F. Tufvesson, "Channel hardening in massive MIMO - a measurement based analysis", in *2018 IEEE 19th International Workshop on Signal Processing Advances in Wireless Communications (SPAWC)*, IEEE, 2018.
- [17] T. Zemen, D. Löschenbrand, M. Hofer, C. Pacher, and B. Rainer, "Orthogonally precoded massive MIMO for high mobility scenarios", *IEEE Access*, vol. 7, pp. 132 979–132 990, 2019. DOI: 10.1109/access.2019.2941316.
- [18] Y. R. Zheng and C. Xiao, "Simulation models with correct statistical properties for Rayleigh fading channels", *IEEE Transactions on Communications*, vol. 51, no. 6, pp. 920–928, 2003, ISSN: 00906778. DOI: 10.1109/TCOMM.2003.813259.
- [19] T. Zemen and C. F. Mecklenbräuker, "Time-variant channel estimation using discrete prolate spheroidal sequences", *IEEE Transactions on Signal Processing*, vol. 53, no. 9, pp. 3597–3607, 2005, ISSN: 1053587X. DOI: 10.1109/TSP.2005.853104.
- [20] R. Hadani, S. Rakib, M. Tsatsanis, A. Monk, A. J. Goldsmith, A. F. Molisch, and R. Calderbank, "Orthogonal time frequency space modulation", in *IEEE Wireless Communications and Networking Conference, WCNC*, IEEE, 2017, ISBN: 9781509041831. DOI: 10.1109/WCNC.2017.7925924. arXiv: 1808.00519.
- [21] D. Slepian, "Prolate spheroidal wave functions, Fourier analysis, and uncertainty-V: The discrete case", *Bell Systems Technical Journal*, vol. 57, no. 5, pp. 1371–1430, 1978, ISSN: 00058580. DOI: 10.1002/j.1538-7305.1978.tb02104.x.
- [22] 3GPP, "NR; Physical channels and modulation", 3rd Generation Partnership Project (3GPP), Technical Specification (TS) 38.211, Jun. 2021, Version 16.6.0. [Online]. Available: <https://portal.3gpp.org/desktopmodules/Specifications/SpecificationDetails.aspx?specificationId=3213>.
- [23] "5G TDD synchronisation guidelines and recommendations for the coexistence of TDD networks in the 3.5 GHz range", GSMA, Tech. Rep., 2020. [Online]. Available: <https://www.gsma.com/spectrum/wp-content/uploads/2020/04/3.5-GHz-5G-TDD-Synchronisation.pdf>.
- [24] S. Kashyap, C. Mollén, E. Björnson, and E. G. Larsson, "Performance analysis of (TDD) massive MIMO with Kalman channel prediction", in *2017 IEEE Int. Conf. Acoustics, Speech and Signal Process. (ICASSP)*, 2017, pp. 3554–3558. DOI: 10.1109/ICASSP.2017.7952818.

- [25] H. Kim, S. Kim, H. Lee, C. Jang, Y. Choi, and J. Choi, "Massive MIMO channel prediction: Kalman filtering vs. machine learning", *IEEE Transactions on Communications*, vol. 69, no. 1, pp. 518–528, 2021. DOI: 10.1109/TCOMM.2020.3027882.
- [26] C. Wu, X. Yi, Y. Zhu, W. Wang, L. You, and X. Gao, "Channel prediction in high-mobility massive MIMO: From spatio-temporal autoregression to deep learning", *IEEE Journal on Selected Areas in Communications*, vol. 39, no. 7, pp. 1915–1930, 2021. DOI: 10.1109/JSAC.2021.3078503.
- [27] T. Zemen, C. F. Mecklenbräuker, and B. H. Fleury, "Minimum-energy bandlimited time-variant channel prediction with dynamic subspace selection", *IEEE Transactions on Signal Processing*, vol. 55, no. 9, pp. 4534–4548, 2007, ISSN: 22195491.
- [28] K. Huber and S. Haykin, "Improved Bayesian MIMO channel tracking for wireless communications: Incorporating a dynamical model", *IEEE Transactions on Wireless Communications*, vol. 5, no. 9, pp. 2468–2476, 2006, ISSN: 15361276. DOI: 10.1109/TWC.2006.04313.
- [29] A. J. Tenenbaum, R. S. Adve, and Y.-S. Yuk, "Channel prediction and feedback in multiuser broadcast channels", in *2009 11th Canadian Workshop on Information Theory (CWIT)*, 2009, pp. 67–70, ISBN: 9781424434015. DOI: 10.1109/CWIT.2009.5069523.
- [30] C. Potter, G. K. Venayagamoorthy, and K. Kosbar, "RNN based MIMO channel prediction", *Signal Processing*, vol. 90, no. 2, pp. 440–450, 2010, ISSN: 01651684. DOI: 10.1016/j.sigpro.2009.07.013. [Online]. Available: <http://dx.doi.org/10.1016/j.sigpro.2009.07.013>.
- [31] Y. Yang, F. Gao, G. Y. Li, and M. Jian, "Deep learning-based downlink channel prediction for FDD massive MIMO system", *IEEE Communications Letters*, vol. 23, no. 11, pp. 1994–1998, 2019, ISSN: 15582558. DOI: 10.1109/LCOMM.2019.2934851. arXiv: 1912.12265.
- [32] A. K. Papazafeiropoulos, "Impact of general channel aging conditions on the downlink performance of massive MIMO", *IEEE Transactions on Vehicular Technology*, vol. 66, no. 2, pp. 1428–1442, 2016.
- [33] Ö. T. Demir, E. Björnson, L. Sanguinetti, *et al.*, "Foundations of user-centric cell-free massive MIMO", *Foundations and Trends in Signal Processing*, vol. 14, no. 3-4, pp. 162–472, 2021.
- [34] G. Interdonato, E. Björnson, H. Quoc Ngo, P. Frenger, and E. G. Larsson, "Ubiquitous cell-free massive MIMO communications", *EURASIP Journal on Wireless Communications and Networking*, vol. 2019, no. 1, 2019.
- [35] T. Bigler, A. Treytl, D. Löschenbrand, and T. Zemen, "High accuracy synchronization for distributed massive MIMO using White Rabbit", in *2018 IEEE International Symposium on Precision Clock Synchronization for Measurement, Control, and Communication (ISPCS)*, IEEE, 2018, pp. 1–6.
- [36] M. Friese, "Multitone signals with low crest factor", *IEEE Transactions on Communications*, vol. 45, no. 10, pp. 1338–1344, 1997, ISSN: 00906778. DOI: 10.1109/26.634697.
- [37] S. Coleri, M. Ergen, A. Puri, and A. Bahai, "Channel estimation techniques based on pilot arrangement in OFDM systems", *IEEE Transactions on Broadcasting*, vol. 48, no. 3, pp. 223–229, 2002, ISSN: 00189316. DOI: 10.1109/TBC.2002.804034.

- [38] F. Hlawatsch and G. Matz, Eds., *Wireless Communications over Rapidly Time-Varying Channels*. Academic Press, 2011.
- [39] B. Rainer, D. Löschenbrand, S. Zelenbaba, M. Hofer, and T. Zemen, "Towards a non-stationary correlated fading process for diffuse scattering in ray tracing", in *2020 IEEE 31st Annual International Symposium on Personal, Indoor and Mobile Radio Communications*, 2020. DOI: 10.1109/PIMRC48278.2020.9217182.
- [40] R. G. Kouyoumjian and P. H. Pathak, "A uniform geometrical theory of diffraction for an edge in a perfectly conducting surface", *Proceedings of the IEEE*, vol. 62, no. 11, pp. 1448–1461, 1974, ISSN: 0018-9219. DOI: 10.1109/PROC.1974.9651.
- [41] F. Mani, F. Quitin, and C. Oestges, "Accuracy of depolarization and delay spread predictions using advanced ray-based modeling in indoor scenarios", *EURASIP Journal on Wireless Communications and Networking*, vol. 2011, no. 1, p. 11, 2011, ISSN: 1687-1499. DOI: 10.1186/1687-1499-2011-11. [Online]. Available: <https://doi.org/10.1186/1687-1499-2011-11>.
- [42] M. Gan, X. Li, F. Tufvesson, and T. Zemen, "An effective subdivision algorithm for diffuse scattering of ray tracing", in *2014 XXXIth URSI General Assembly and Scientific Symposium (URSI GASS)*, 2014. DOI: 10.1109/URSIGASS.2014.6929365.
- [43] V. Degli-Esposti, F. Fuschini, E. M. Vitucci, and G. Falciasecca, "Measurement and modelling of scattering from buildings", *IEEE Transactions on Antennas and Propagation*, vol. 55, no. 1, pp. 143–153, 2007, ISSN: 0018-926X. DOI: 10.1109/TAP.2006.888422.
- [44] G. Matz, "On non-WSSUS wireless fading channels", *IEEE Transactions on Wireless Communications*, vol. 4, no. 5, pp. 2465–2478, 2005, ISSN: 15361276. DOI: 10.1109/TWC.2005.853905.
- [45] A. Paier, T. Zemen, L. Bernado, G. Matz, J. Karedal, N. Czink, C. Dumard, F. Tufvesson, *et al.*, "Non-WSSUS vehicular channel characterization in highway and urban scenarios at 5.2 GHz using the local scattering function", in *2008 International ITG Workshop on Smart Antennas*, 2008, pp. 9–15. DOI: 10.1109/WSA.2008.4475530.
- [46] D. B. Percival and A. T. Walden, *Spectral Analysis for Physical Applications*. Cambridge University Press, 1963.
- [47] E. Zöchmann, M. Hofer, M. Lerch, S. Pratschner, L. Bernadó, J. Blumenstein, S. Caban, S. Sangodoyin, *et al.*, "Position-specific statistics of 60 GHz vehicular channels during overtaking", *IEEE Access*, vol. 7, pp. 14 216–14 232, 2019. DOI: 10.1109/ACCESS.2019.2893136.
- [48] L. Bernadó, T. Zemen, F. Tufvesson, A. F. Molisch, and C. F. Mecklenbräuker, "Delay and Doppler spreads of non-stationary vehicular channels for safety relevant scenarios", *IEEE Transactions on Vehicular Technology*, no. 1, pp. 82–93, ISSN: 0018-9545. DOI: 10.1109/TVT.2013.2271956. arXiv: 1305.3376.
- [49] L. Bernadó, T. Zemen, F. Tufvesson, A. F. Molisch, and C. F. Mecklenbräuker, "Time- and frequency-varying K-factor of non-stationary vehicular channels for safety relevant scenarios", *IEEE Transactions on Intelligent Transportation Systems*, vol. 16, no. 2, pp. 1007–1017, 2015.
- [50] F. J. Massey Jr., "The Kolmogorov-Smirnov test for goodness of fit", *Journal of the American Statistical Association*, vol. 46, no. 253, pp. 68–78, 1951. DOI: 10.1080/01621459.1951.10500769.

- [51] H. Q. Ngo, "Massive MIMO : Fundamentals and System Designs", PhD thesis, Linköping University, 2015, p. 67, ISBN: 9789175191478. DOI: 10.3384/lic.diva-112780.
- [52] H. I. Obakhena, A. L. Imoize, F. I. Anyasi, and K. Kavitha, "Application of cell-free massive MIMO in 5G and beyond 5G wireless networks: A survey", *Journal of Engineering and Applied Science*, vol. 68, no. 1, 2021.
- [53] J. Zhang, S. Chen, Y. Lin, J. Zheng, B. Ai, and L. Hanzo, "Cell-free massive MIMO: A new next-generation paradigm", *IEEE Access*, vol. 7, pp. 99 878–99 888, 2019.
- [54] S. Payami and F. Tufvesson, "Channel measurements and analysis for very large array systems at 2.6 GHz", in *6th European Conference on Antennas and Propagation (EUCAP)*, 2012, pp. 433–437.
- [55] À. O. Martínez, E. D. Carvalho, and J. Ø. Nielsen, "Towards very large aperture massive MIMO: A measurement based study", in *IEEE Globecom Workshops (GC Wkshps)*, 2014, pp. 281–286. arXiv: arXiv:1507.06203v1.
- [56] T. Choi, M. Ito, I. Kanno, T. Oseki, K. Yamazaki, and A. F. Molisch, "Uplink energy efficiency of cell-free massive MIMO with transmit power control in measured propagation channels", in *2021 IEEE Workshop on Signal Processing Systems (SiPS)*, 2021, pp. 164–169.
- [57] T. Choi, J. Gomez-Ponce, C. Bullard, I. Kanno, M. Ito, T. Ohseki, K. Yamazaki, and A. F. Molisch, "Using a drone sounder to measure channels for cell-free massive MIMO systems", in *2022 IEEE Wireless Communications and Networking Conference (WCNC)*, IEEE, 2022, pp. 2506–2511.
- [58] H. Q. Ngo, E. G. Larsson, and T. L. Marzetta, "Aspects of favorable propagation in massive MIMO", *European Signal Processing Conference*, no. 1, pp. 76–80, 2014, ISSN: 22195491. arXiv: arXiv:1403.3461v1.
- [59] S. McKinley and M. Levine, "Cubic spline interpolation", *College of the Redwoods*, vol. 45, no. 1, pp. 1049–1060, 1998.
- [60] C. De Boor, *A Practical Guide To Splines*. Springer New York, 1978, vol. 27.
- [61] W. Jiang, B. Han, M. A. Habibi, and H. D. Schotten, "The road towards 6G: A comprehensive survey", *IEEE Open Journal of the Communications Society*, vol. 2, pp. 334–366, 2021. DOI: 10.1109/OJCOMS.2021.3057679.
- [62] D. Milovančev, N. Vokić, D. Löschenbrand, T. Zemen, and B. Schrenk, "Analog coherent-optical mobile fronthaul with integrated photonic beamforming", *IEEE Journal on Selected Areas in Communications*, vol. 39, no. 9, pp. 2827–2837, 2021. DOI: 10.1109/JSAC.2021.3064640.
- [63] A. V. Martí, D. Löschenbrand, M. Hofer, T. Zemen, and B. Schrenk, "Photonic delay processing with centralized etalon cascade for radio beamsteering in simplified 2×5 phased-array radio heads", *Journal of Lightwave Technology*, vol. 40, no. 20, pp. 6929–6938, 2022. DOI: 10.1109/JLT.2022.3188355.